Refractory high entropy alloys for hydrogen storage

Jorge Montero Banuelos

Thesis to obtain the degree of **Doctor of Philosophy**
from the University of Paris-Est

Degree in **Chemistry**
Institut de Chimie et des Matériaux de Paris-Est, CNRS

Refractory High-Entropy Alloys for Hydrogen Storage

Submitted by **Jorge MONTERO BAÑUELOS**

Thesis defended 15 - Dec - 2020

Jury :

Dr. Patricia de RANGO	Institut Néel, CNRS, Grenoble	Reviewer
Dr. Luc AYMARD	Université de Picardie, CNRS, Amiens	Reviewer
Dr. Thierry GROSDIDIER	Université de Lorraine, CNRS, Nancy	President
Dr. Ivan GUILLOT	Université de Paris-Est, CNRS, Créteil	Examiner
Dr. Claudia ZLOTEA	Université de Paris-Est, CNRS, Créteil	Supervisor

Summary

For many years now, hydrogen has been considered one of the most promising energy carriers to substitute fossil fuels due to its numerous applications and advantages over hydrocarbons and other sources of energy. However, the bottleneck for hydrogen-based technologies lies within two major issues: the production of hydrogen at competitive market prices, and the safe storage of hydrogen for transportation and supply. This project aims for the solid-state hydrogen storage in metals and alloys, also known as metal hydrides, which are considered safe stores with high-energy densities. In this project, we study the structural and hydrogen sorption properties of different multi-principal element alloys (MPEA) based on refractory elements, in the form of Ti-V-Zr-Nb-*M* (*M*=Ta, Al, Mg), also known as high-entropy alloys. These alloys were prepared using two different techniques, arc melting and high-energy ball milling. All MPEAs have adopted a single *bcc* structure and can rapidly absorb hydrogen at 25 °C, with a maximum hydrogen capacity between 1.6-2.0 H/*M* (2.4-2.8 wt.%). *In-situ* neutron diffraction experiments were performed to study the structural transformation of the MPEAs during hydrogen desorption. Synchrotron X-ray diffraction characterization was also employed to determine the crystalline structure of the produced hydrides. All MPEAs studied in this project underwent a single-phase transformation from a pristine *bcc* alloy to an *fcc* hydride phase upon hydrogen absorption, except for the Al-containing alloy that adopted a *bct* structure in its hydride form. The hydrogen absorption-desorption cycling properties were evaluated in terms of hydrogen capacity and the structural and chemical properties were characterized before and after cycling. All alloys were able to reversibly store up to 82-89% of their initial capacity up to 10-20 hydrogenation cycles, while retaining their single crystalline structure.

Even though the development of high-entropy alloys as a safe hydrogen stores is still in its infancy, these materials (MPEAs) are interesting candidates for hydrogen storage due to their chemical diversity and promising hydrogenation properties.

Table of content

CHAPTER I

~ Introduction ~

CHAPTER 1. Introduction

For many decades, the scientific community has shown great concern regarding the implications of hydrocarbons and the combustion of fossil fuels as the base of our energy economy, currently generating more than the 80% of the global energy and releasing dangerous amounts of CO_2 and other greenhouse gases into the atmosphere. Many countries all around the world have encouraged initiatives to switch to a zero-emission energy-based economy by implementing new technologies and using alternative sources that are cleaner and more sustainable than fossil fuels. Hydrogen as an energy carrier has a promising future in the energy landscape as it can overcome most of the drawbacks of fossil fuels, however, the bottleneck of these technologies lies principally on the development of safe and efficient methods for hydrogen storage. Extensive research has been carried out to find proper methods for mobile and stationary applications, either for combustion engines or fuel cells. Among the many methods to store hydrogen, the solid-state storage of hydrogen inside metals stands out due to its high-energy density, long life-cycle, low costs of operation and maintenance, and principally, is one of the safest methods.

1.1 Hydrogen: energy carrier

Hydrogen as an energy carrier has numerous advantages over other forms of energy sources due to its flexibility for diverse energy-based applications, mobile and stationary. Hydrogen-based technologies can overcome certain limitations of its competitors, like lithium-batteries or solar energy, as the amount of energy harvested from hydrogen can be scaled to power from small devices to even industrial level applications. The energy stored in hydrogen comes from the chemical bond of the molecular hydrogen (H_2) and this can be harvested mainly in two pathways: combustion to generate heat or mechanical work, and fuel cells to produce electrical energy. One of the main attractiveness of hydrogen is the clean use of energy from its combustion, releasing water as the product of the reaction, and has a more superior (mass)energy density, ~140 KJ/Kg, than any other commercially available hydrocarbon, ~30-42 KJ/Kg[1]. This makes hydrogen the ultimate candidate to substitute fossil fuels that will eventually lead to a zero CO_2 emission economy.

1.2 Hydrogen storage

Despite the numerous benefits of hydrogen as an energy carrier, the implementation of these technologies is held back mainly by the lack of safe methods to store hydrogen with high energy densities (gravimetric and volumetric) and the ability to work efficiently at mild operating conditions. Over the years, different methods have been studied to store hydrogen and these may be classified into two main families: *physical storage* and *chemical storage*, each owning advantages and limitations for energy-based applications mainly due to their operating conditions, as depicted in Figure 1.1.

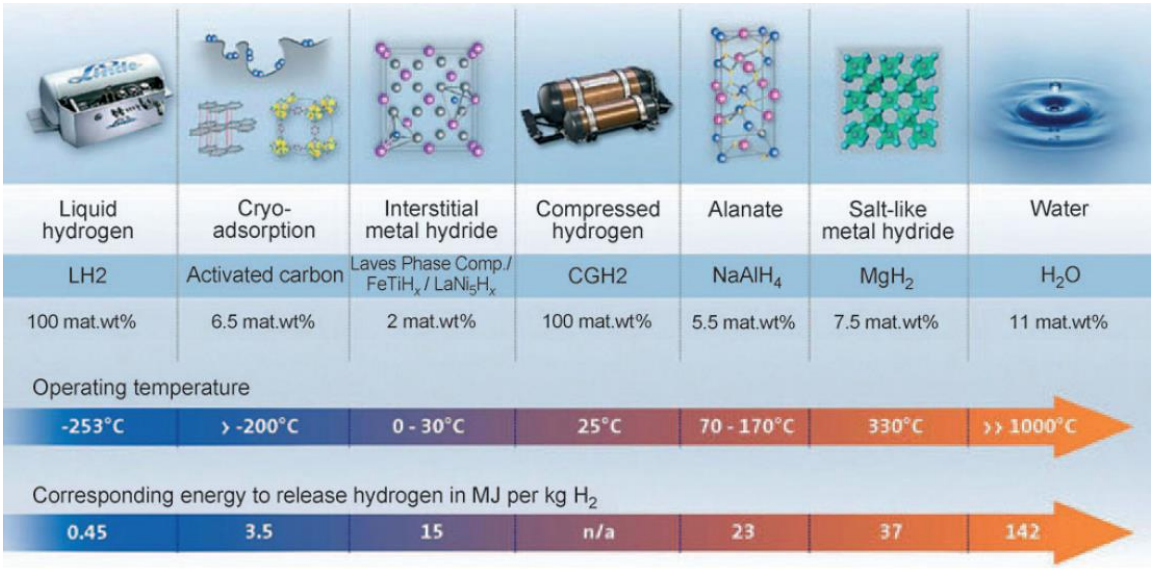

Figure 1.1.Hydrogen storage technologies and their respective operational conditions.[2]

1.2.1 Physical storage

This classification, as it names implies, encompasses methods that store hydrogen in its pure state (gaseous or liquid) and under this branch, three main categories stand out: compressed gaseous hydrogen, liquid hydrogen, and cryoadsorption on high-surface area materials.

1.2.1.1 Compressed gaseous hydrogen

Currently, high-pressure gas tanks (HPGT) are the best option for the automotive industry and are the benchmark for new fuel devices, with a few companies already using hydrogen-fuel systems in vehicles (e.g. BMW, Toyota, Hyundai, etc.). This method requires safe high-pressure vessels able to sustain significant loads of hydrogen at 350-700 bar (35-70 MPa)[3]. However, several implications

of HPGT restrict their number of applications due to the low energy density of the gas. There are two ways to increase the energy density, increasing the volume of the tank, or increasing the pressure of the gas. Increasing the volume of HPGT is not a reliable option for automobile vehicles as they require of compact designs for onboard applications. Increasing the pressure of the gas not only represents a latent risk for the user in case of accident or tank malfunction but, pressures above 70 MPa causes large deviations from the ideal gas and reduces the efficiency of the fuel system. Thus, certain applications and further development of HPGT are limited[3].

1.2.1.2 Liquid hydrogen

Hydrogen at cryogenic temperatures, -253 °C, is another form to store hydrogen using special tanks. This method offers a higher energy density than HPGT at 70 MPa, however, there are significantly more challenges when using liquid hydrogen for mobile and even stationary applications. Due to the hydrogen low enthalpy of phase change, from liquid to gas, hydrogen evaporates easily by the heat exchange from the environment, causing an increment in the pressure inside the tank, and because of this, venting is necessary for the proper functionality of the system. Significant amounts of hydrogen are lost due to evaporation and this represents a big engineering challenge. This issue can be minimized by increasing the volume of the tank, reducing the surface-to-area ratio. Thus, liquid hydrogen is more practical for stationary applications where the size and volume are not a restriction.

1.2.1.3 (Cryo-)Adsorption

Cryoadsorption is the borderline between physical and chemical storage, as hydrogen is not in the liquid or the gas state, but rather adhered at a molecular level by weak interactions with the adsorbent (physisorption) and the dissociation of hydrogen does not take place. In this method, hydrogen molecules are adsorbed at the surface, or inside the cavities, of porous materials, typically at cryogenic temperatures due to the low enthalpies of adsorption (2-5 kJ/mol)[3]. Materials with high-surface areas, such as metal-organic frameworks, carbon-porous materials, among others, are commonly used for hydrogen storage since the hydrogen capacity of the materials typically increases with surface area. This approach may overcome some of the downsides of using liquid hydrogen, although the volumetric hydrogen density is still lower than HPGTs. One of the major setbacks in this method is the amount of heat released during hydrogen adsorption, 2-5 MJ per Kg

of H_2 depending on the storing material; liquid nitrogen is commonly used to maintain low temperatures, i.e. around 80-200 kg of liquid N_2 are needed to store 1 kg of H_2[3].

1.2.2 Chemical storage

Generally speaking, in chemical storage, hydrogen is bounded to a metal or an organic compound by means of a chemical bond (covalent, metallic, or ionic). Organic compounds, such as amines or hydrocarbons, are a good way to safely store and transport hydrogen, however, there are many implications when using these as transportation methods. Complex reaction mechanisms may be needed in order to release the hydrogen for its utilization and these cannot be regenerated, but rather they need to be exchanged after use. Another method is to store solid-state hydrogen inside metals. This is a promising field of study for both mobile and stationary applications due to hydrides being a safe form of hydrogen storage able to achieve high volumetric energy densities, to operate under mild pressure and temperature conditions, and have good reversible sustainability with low cost of operation and maintenance. However, there are still challenges to overcome. These materials can be further categorized into two main groups depending on the type of bond with hydrogen: complex hydrides and interstitial metal hydrides (pure metals, alloys, and intermetallics).

1.2.2.1 Complex hydrides

Complex hydrides are characterized by the covalent bonding between hydrogen and the metallic element (or a non-metallic) with comparable electronegativity as hydrogen, e.g. beryllium, aluminum or boron, forming a complex anion. The charge of the anion is then balanced by a cation, typically by a lightweight element from the alkali or alkaline-earth groups, e.g. lithium, sodium, etc[4]. These materials can achieve storing capacities as high as 18.5 wt.% for the case of $LiBH_4$[5], however, these hydrides are too stable and have the disadvantage of producing toxic and volatile boranes when releasing hydrogen, which can eventually lead to a short life-cycle as a fuel system[6]. Other complex hydrides, such as NaAlH4, have a reversible storage capacity of 5.6 wt.% and can operate under mild temperature and pressure conditions (~130 °C and 0.1 MPa)[3], [4]. The downside of this material is the harsh conditions of re-hydrogenation which makes it unpractical for mobile applications. Nevertheless, these materials are still investigated as doping them with other elements can help to overcome these challenges.

1.2.2.2 Metal hydrides

The most studied materials for hydrogen storage are Mg and Mg-based alloys. Mg can form a stable binary hydride (MgH_2) with a maximum storage capacity of 7.6 wt.%[7], which is an interesting material for energy applications due to its lightweight density, high storage capacity, and the fact that Mg is an abundant element in earth's crust. However, the major setback of pure MgH_2 is the poor absorption and desorption kinetics, requiring high temperatures for operation. Extensive research has been carried out to improve the kinetics of the process by doping the material with rare-earth elements, transition and non-transitions elements, and by studying other Mg-based compositions[8]. Intermetallic systems in the form of AB_5 (e.g. $LaNi_5$), AB_2 (e.g. $ZrMn_2$), and other alike, have been also widely investigated and these are mainly composed of transitions metals. In comparison to the Mg-based alloys, intermetallics are heavier compounds and can only reach gravimetric capacities of around 2 wt.% with better absorption kinetics at room temperature[9]. Some transition metals like V, Ti, and Zr, are able to form stable binary hydrides at mild temperature and pressure conditions, with hydrogen capacities of around, but never exceeding, 2 H/*M*[10]. These are interesting elements to use for hydrogen storage as they allow a wide variety for alloy compositions that can be studied, and allow the modification of the hydrogen sorption properties by adding one of more elements into the base metal.

Figure 1.2 shows the hydrogen densities of a few selected materials, from each method above mentioned, in a plot describing the volumetric hydrogen density versus the gravimetric density of the materials[8].

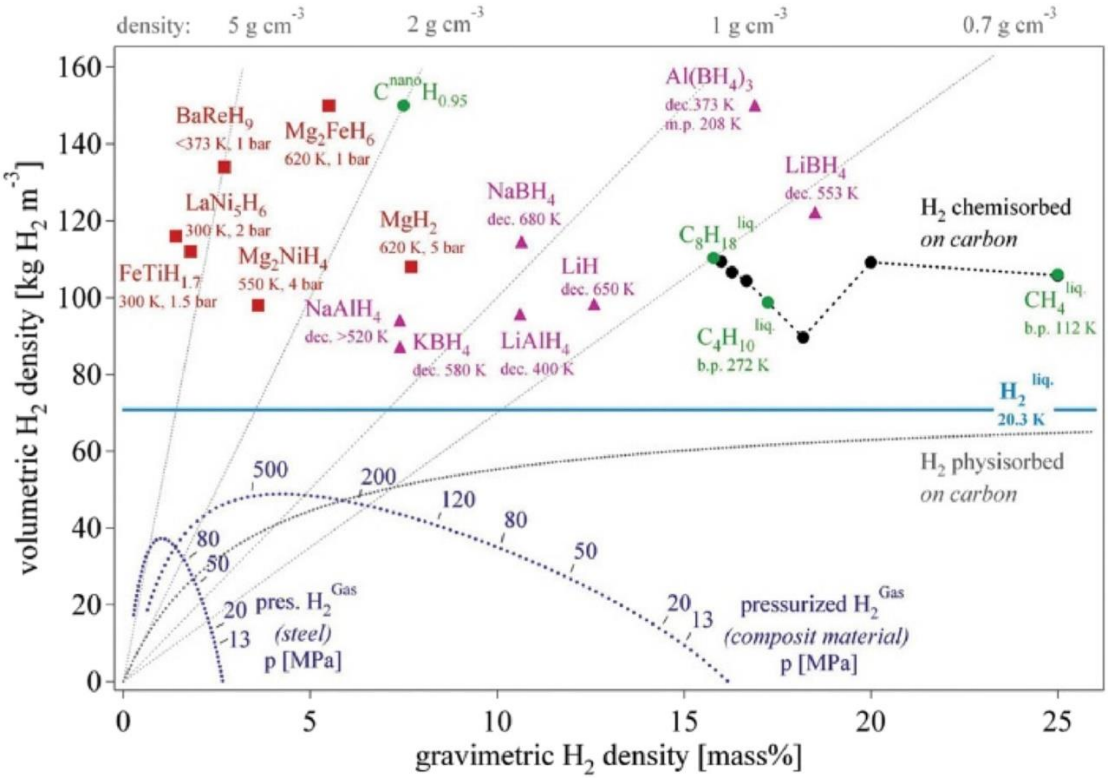

Figure 1.2. Volumetric vs gravimetric density plot of diverse hydrogen storage materials: high-pressure gas tanks, liquid hydrogen, intermetallics (red), complex hydrides (magenta), organic compounds (green), and carbon materials[8].

1.3 Metal hydride formation

Metal hydrides are formed from the reaction between hydrogen gas and a metal, where hydrogen is stored in the interstitial sites of the metallic lattice (interstitial metal hydrides). This phenomenon can be described by a complex process that involves: hydrogen adsorption at the surface, dissociation of the molecular hydrogen, penetration of the individual atoms, diffusion into the crystalline structure, and finally nucleation and growth of the hydride phase[6]. The location of the hydrogen atoms inside the metal causes an expansion of the crystal lattice, which is proportional to the hydrogen concentration, of about 2-3 Å^3 per hydrogen atom[11].

Figure 1.3 shows a simplified schematic of the hydrogenation process in metal interstitial hydrides. First, the molecular hydrogen is adsorbed at the surface of the metal by weak van der Waals interactions. Then, providing sufficient energy from the temperature and pressure conditions, the molecular hydrogen dissociates into individual atoms which then migrate into the subsurface of the

material and subsequently diffuse into the lattice, occupying random positions inside the material. The disordered occupation of hydrogen inside the metal is known as a solid solution, or *α-phase*. If the concentration of hydrogen is high enough, the hydrogen-hydrogen interactions begin to increase forming an ordered array of hydrogen atoms within the lattice forming what is known as a hydride phase, or *β-phase*. This process is reversible under certain temperature and pressure conditions.

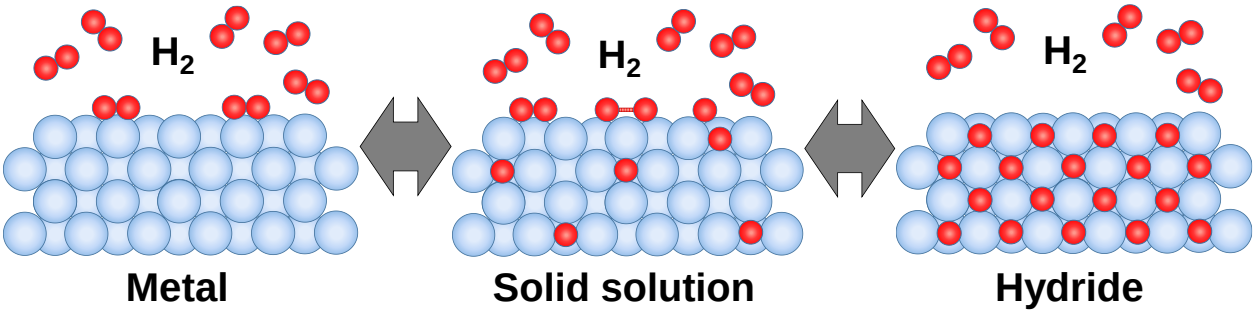

Figure 1.3. Schematic representation of the absorption process of hydrogen gas in solid metals.

Considering the chemical reaction between the solid metal and the gaseous hydrogen

$$M_{(s)} + H_{2(g)} \leftrightarrow MH_{2(s)} + \mathrm{Q}(heat) \qquad \text{Equation 1.1}$$

the thermodynamics of the reaction are described by the van't Hoff equation (Equation 1.2), establishing a correlation between the temperature for hydrogen absorption/desorption at a given equilibrium pressure,

$$\ln(P_{eq}) = \frac{\Delta H_r}{RT} - \frac{\Delta S_r}{R} \qquad \text{Equation 1.2}$$

where P_{eq} is the equilibrium pressure of the hydrogen gas, ΔH and ΔS are enthalpy and entropy change of the hydride formation reaction, respectively, R is the gas constant, and T is the temperature. To experimentally determine the thermodynamic properties of the solid-gas reaction, a van't Hoff plot ($\ln(P_{eq})$ *vs* T^{-1}) may be constructed by measuring several pressure-composition-isotherms (PCI) by at least three different temperatures, as illustrated in Figure 1.4.

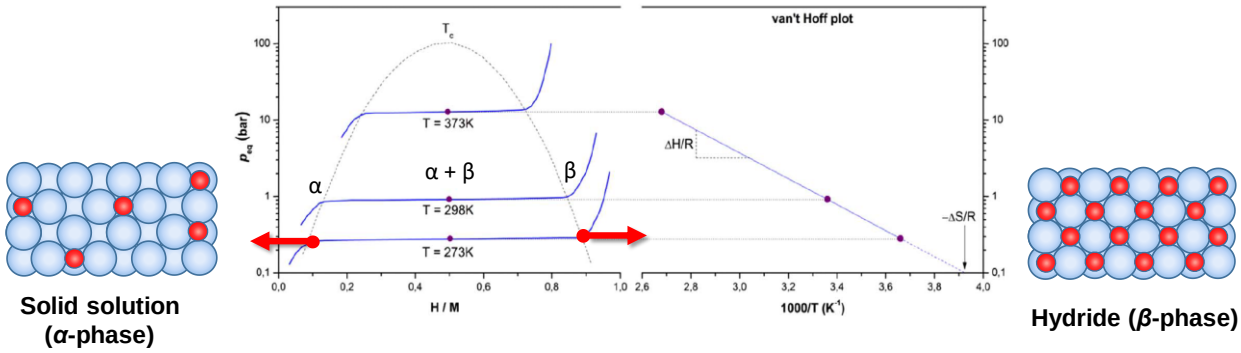

Figure 1.4. Illustration of a pressure-composition-isotherm at different temperatures for a hypothetical metal hydride and van't Hoff plot on the right for the determination of the thermodynamic properties[12].

PCI is the plot of H_2 pressure at equilibrium as a function of the hydrogen gas absorbed, expressed in H/*M* or wt.%. These PCI measurements provide insightful information about the mechanism of the hydrogenation reaction[13]. When the absorption process begins, at low hydrogen concentration, the hydrogen absorbed resides in random positions within the metallic structure forming a solid solution, or *α-phase*. Once surpassing certain hydrogen concentration, typically ~0.1 H/*M*, the *α*-phase begins to transform into the *β*-phase, and this process is characterized by the plateau region in the PCI plot. The plateau pressure is known as the equilibrium pressure for hydride formation (P_{eq}) and its length is equivalent to the maximum reversible storage capacity. The P_{eq} and the length of the plateau are strongly dependent on temperature, where higher temperatures typically increases the P_{eq}, and the storage capacity is reduced.

1.4 High-entropy alloys

This project will study a new paradigm of metallic materials known as *high-entropy alloys*, which are a relatively new classification of multi-component alloys mostly known for their remarkable mechanical properties and their peculiar crystalline structure[14].

High-entropy alloys (HEA) are disordered solid solutions constituted of at least five elements in near equimolar concentration, 5-35 at%, which can adopt simple crystalline structures such as body-centered cubic (*bcc*), face-centered cubic (*fcc*), and hexagonal close-packed (*hcp*)[15]. It has been suggested that the high configurational entropy of mixture is the cause of stabilization of the solid solutions[14]. These materials belong to a broader classification known as multi-principal element alloys (MPEA), which encompasses alloy compositions exploring the central region of the multi-component phase diagram (Figure 1.5a). Because HEAs are formed of at least 5 elements with

different atomic sizes and can adopt simple crystalline structures, these materials have higher lattice strain in their structure than more conventional alloys, as depicted in Figure 1.5b. This feature grants HEAs outstanding mechanical properties as well as other interesting optical, magnetic, and piezoelectric properties[16]. Recent works on high-entropy alloys have reported very interesting hydrogen absorption capacities too, even superior to some classical *bcc* alloys[17].

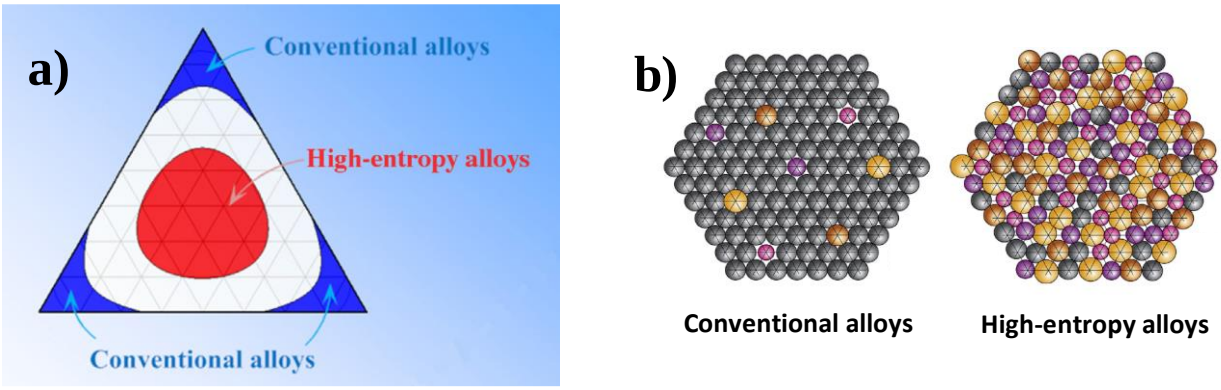

Figure 1.5. a) multi-component phase diagram highlighting the regions for conventional and high-entropy alloys, b) representation of the compositional difference between conventional and high-entropy alloys [14], [18].

One of the main characteristics of HEAs is the ability to form single-phase solid solutions, a key feature for the evaluation of their hydrogen sorption properties. Two important parameters can help predict the stability of the solid solutions in HEAs, namely *lattice distortion* and *valence electron concentration*. The lattice distortion (δ), as described by Yang and Zhang[19], is a parameter that quantifies the amount of strain in the lattice structure, involving the concentration and relative sizes of the atoms in the mixture, described by the following equation:

$$\delta\% = 100\% \sqrt{\sum_{i=1}^{n} c_i \left(1 - \frac{r_i}{\sum_{j=1}^{n} c_j r_j}\right)} \qquad \text{Equation 1.3}$$

where $c_{i,j}$ and $r_{i,j}$ are the atomic concentration and atomic radii of the *i*th and *j*th element in the mixture. Yang and Zhang[19] noticed a trend by studying several alloy compositions and the stability of their phase as a function of δ parameter, where they found that some alloys with δ values below a certain threshold tend to form single-phased solid solutions (δ%< 6.6%), while those with higher δ tend form other phases, such as intermetallics, precipitates, or amorphous phases (see Figure 1.6a). Same trend has been confirmed by different authors[18].

On the other hand, valence electron concentration, or VEC, is another parameter that can help predict the crystalline structure of the HEAs. Couzinié and Dirras[20] reported a similar approach by compiling several disordered single solid solutions (*bcc* and *fcc*) and other HEAs with multiple phases, and plot them as a function of VEC (Figure 1.6b). The authors found out that single-phased HEAs with VEC below 6 tend to form *bcc* structures, while those with higher VEC tend to adopt *fcc* structures. Similar trends have been confirmed by different authors[21], [22].

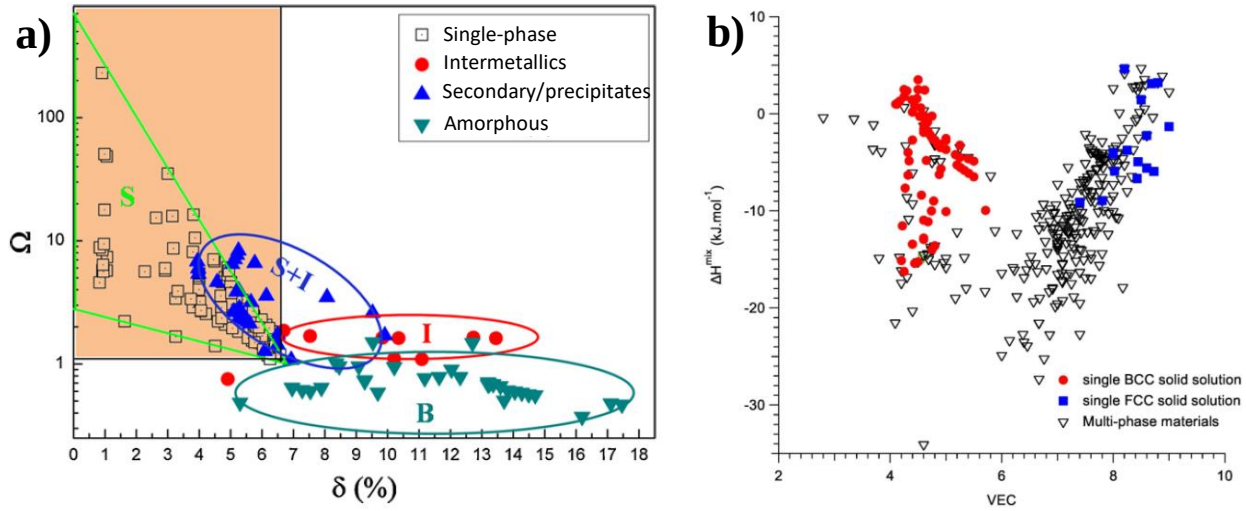

Figure 1.6. a) Phase stability in high-entropy alloys as a function of lattice distortion (δ) [19], and b) relationship between the valence electron concentration (VEC) and the crystalline structure of several HEAs [20]. Legend on a) Ω is a parameter defined by the relationship between the entropy and enthalpy of mixing, $\Omega = \frac{T\Delta S_{mix}}{|\Delta H_{mix}|}$.

1.4.1 Hydrogen storage in *bcc* HEAs: review

The hydrogen sorption properties of MPEAs and HEAs are scarcely investigated in literature and it is often reported for multiphase and intermetallic compounds[23]–[28], and only a few numbers of papers have reported the hydrogen sorption properties of single-phased alloys[17], [29]–[38]. A couple of these have attempted to relate the hydrogen sorption capacities in the MPEA with their fundamental properties such as the lattice distortion, lattice constant, valence electron concentration (VEC), or chemical concentration, by studying several alloy compositions [29], [37], [39]. However, up to date of this manuscript, there is no clear trend that can be generalized for MPEAs and HEAs due to the many degrees of freedom in multi-component alloys. Little-to-none conclusions can be drawn when comparing different studies reported in the literature, as each

system possesses different chemical composition that plays a role in the hydrogenation of the alloy. And yet it is not clear how individual, or a mixture of, elements can affect the overall properties of HEAs[14]. The objective of this doctoral project is to develop a new strategy towards the understanding of the fundamental properties of HEAs and metal hydrides by systematically studying the effect of a single variable on the alloy composition.

One of the first HEA studied for hydrogen storage was reported by Kunce *et al.*[31], where the authors prepared a single-phase TiVZrNbMo in equimolar composition by laser engineered net shaping (LENS), a technique commonly used for the syntheses of materials with porous microstructures. The alloy crystallized in a *bcc* structure and had a maximum hydrogen capacity of 0.5 H/*M* (0.6 wt.%) under 85 bar of equilibrium pressure at 50 °C, resulting in a hydrogen solid solution. This composition showed poor hydrogen capacity but fast kinetics at 50 °C. Being one of the first studies on HEAs, the authors concluded that the lattice distortion did not favor hydrogen absorption. However, nowadays, more evidence supports the contrary, and instead, the poor capacity in this composition might be related to the synthetic method employed (LENS), the degree of surface oxidation, and the lack of a proper activation treatment. Thus, higher capacity may be expected for TiVZrNbMo, since other alloys with similar compositions have demonstrated superior capacities.

Sahlberg *et al.*[17] have reported the synthesis and hydrogenation properties of a single-phase HEA TiVZrNbHf synthesized by arc melting, with an outstanding hydrogen capacity of 2.5 H/*M*. This hydrogen capacity is greater than most conventional *bcc* alloys and its individual elements too, which typically have a maximum capacity of ~2 H/*M*. In a later work[30], it was reported that hydrogen atoms of the hydride phase (2.5 H/*M*) have simultaneously occupied both the tetrahedral and octahedral interstitial sites in a body-centered tetragonal structure (*bct*), granting its superior hydrogen capacity. It was then hypothesized that the high lattice distortion in the HEA (δ= 6.8% of TiVZrNbHf) favored a superior hydrogen uptake.

Following the same trend of refractory HEAs, Zlotea *et al.*[36] have produced a single-phase TiZrNbHfTa which was hydrogenated at 300 °C, having a maximum hydrogen capacity of 2.0 H/*M* (1.7 wt.%). Interestingly, this alloy showed two plateau pressures in the PCI curve, where the alloy initially transforms into a mono-hydride phase at low equilibrium pressure, and then the di-hydride phase at 23 bar of equilibrium pressure. *In-situ* synchrotron radiation X-ray diffraction (SR-XRD) experiments demonstrated that the alloy undergoes a phase transformation from a *bcc* structure

(0.0 H/*M*) → *bct* structure (1.0 H/*M*) → *fcc* structure (2.0 H/*M*). The activation energy for hydrogen desorption is around 80.2 kJ/mol, as determined from TDS measurements.

Shen *et al.*[34] have reported the hydrogen-cycling properties of TiZrNbMoHf that has a single-phase transformation from the pristine *bcc* alloy to an *fcc* hydride phase, and is reversible upon hydrogen-cycling. The hydrogen capacity of this alloy was determined from the mass loss by thermo-gravimetric analysis, which is of 1.2 H/*M* (1.2 wt.%). It was further investigated, by the same group, the effect of Mo concentration where 10 at% of Mo had the highest capacity with 1.6 H/*M* (1.5 wt.%), however, no trend was observed between Mo concentration and the hydrogen capacity.

In a different approach, Nygård *et al.*[29] have reported a series of MPEAs with scaling lattice distortion and investigated their hydrogen sorption properties. To achieve this, they synthesized different alloys in the form of $TiVZr_{(z)}NbTa_{(1-z)}$ and $TiVZr_{(1+z)}Nb$ in which the amount of Zr relative to the alloy was controlled to tune the lattice distortion and the lattice constant of the *bcc* phase. All the alloys showed a maximum hydrogen capacity between 1.8-2.0 H/*M* but no trend was observed between the hydrogen capacity and the lattice distortion nor the lattice parameter. Interestingly, they found out that alloys with less Zr-content, < 12.5 at%, can withstand high temperatures for hydrogen desorption, up to 1000 °C, recovering the initial *bcc* structure. Meanwhile, the alloys with higher Zr-content, >12.5 at%, decompose in multiple *bcc* phases at high temperatures. Shortly after, the same group published a second study, this time, they studied several MPEAs with scaling valence electron concentration (VEC)[39], based on TiVNb*M* compositions (*M*= Zr, Hf, Ta, Cr, Mo, and a combination of these). They found a relationship of VEC with the hydride stability, where the temperature for desorption increases with higher values of VEC. Also, while most of the alloys absorbed around 2.0 H/*M*, the alloys with VEC > 5.0 showed lower hydrogen capacities; although only two alloys had a VEC higher than 5.0. This trend has already been seen for classical *bcc* alloys[40]. The hydrogen-cycling properties were also evaluated for the three most unstable alloys and only the composition TiVCrNb was able to reversible store hydrogen at room temperature up to 1.96 H/*M*.

Zepon *et al.*[32] reported the synthesis and hydrogenation of $MgZrTiFe_{0.5}Co_{0.5}Ni_{0.5}$ by high-energy ball milling, under inert conditions, which crystallized in a *bcc* structure and had a maximum capacity of 0.7 H/M (1.2 wt.%) at high temperatures (300 °C). The resulting hydride was a mixture of a *bcc* solid solution and an *fcc* hydride phase, as proven by *in-situ* SR-XRD experiments. Alternatively, they were the first to synthesize a direct hydride of the HEA by reactive ball milling,

which crystallized in a single *fcc* phase but the hydrogen capacity was not determined from this method.

In a different study worth mentioning[35], Zhang *et al*. investigated the effect of heat treatment and the hydrogen sorption properties of TiZrNbTa with little emphasis on the maximum capacity of the alloy. The study focuses on the chemical composition of the surface by X-ray photo-electron spectroscopy before and after the activation treatment, where the surface oxides transform into hydroxides and other complex oxides that allow faster absorption kinetics. The alloy showed a maximum hydrogen capacity of 1.8 H/*M* (1.7 wt.%).

1.5 Project objectives and proposal

The objective of this project is to prepare *bcc* HEAs based on a refractory quaternary alloy in the form of Ti-V-Zr-Nb-*M* and to evaluate the effect on the hydrogen sorption properties by adding a fifth element into the mixture. The motivation to use these refractory elements comes from their individual capability to form stable binary hydrides phases upon hydrogenation which all undergo a phase transformation from a *bcc* metal to a *fcc* hydride. The criteria to choose the fifth element *M* was encouraged to provide a diverse selection of elements from the periodic table with different properties (electronic configuration, molar weight, atomic size, and chemical properties); these elements are ***Mg***, ***Al***, and ***Ta***.

This project proposes the systematic study of the hydrogen sorption properties and structural characterization of refractory-based HEAs. Three different synthetic methods were employed and the hydrogen sorption properties of the same alloy were compared to determine the most suitable synthesis approach: high energy ball milling under inert and reactive atmospheres, and high-temperature arc melting. The hydrogen sorption and structural properties of the MPEA and HEAs were compared and evaluated by diverse manometric, thermo-desorption, and structural characterization techniques, together with the hydrogen-cycling properties.

The structure of this manuscript was divided into the following chapters:

Chapter 1 presents background and context to this project, briefly describing hydrogen as an energy carrier, materials for solid-state storage (or hydrides), our interest in MPEA and HEA, a review of literature on single *bcc* HEAs for hydrogen storage, and ends with the proposed objectives of this project.

Chapter 2 describes the methodologies used for the preparation of the MPEA and all the characterization techniques employed for the evaluation of their structural and hydrogen sorption properties.

*A **preliminary results segment*** is a complementary study to this project, it describes the research carried out during synthesis and phase optimization of the MPEAs, and discusses comparative results of the hydrogenation properties of the alloy Ti-V-Zr-Nb prepared by three different methods, with the intention to establish the most suitable route for the evaluation of the different MPEAs.

Chapter 3 to 6, systematically discusses the results of synthesis of the proposed MPEAs, Ti-V-Zr-Nb-*M* (*M*= Ta, Al, and Mg) and the characterization of their structural and hydrogen sorption properties, respectively.

Lastly, the manuscript will end with general conclusions, highlighting and comparing the most significant results from each MPEA, and providing the different perspectives for this project.

Bibliography

[1] C. Ronneau, *Énergie, pollution de l'air et développement durable*. Presses universitaires de Louvain, 2013.

[2] R. von Helmolt and U. Eberle, "Fuel cell vehicles: Status 2007," *Journal of Power Sources*, vol. 165, no. 2, pp. 833–843, Mar. 2007, doi: 10.1016/j.jpowsour.2006.12.073.

[3] U. Eberle, M. Felderhoff, and F. Schüth, "Chemical and Physical Solutions for Hydrogen Storage," *Angew. Chem. Int. Ed.*, vol. 48, no. 36, pp. 6608–6630, Aug. 2009, doi: 10.1002/anie.200806293.

[4] B. Bogdanovic, M. Felderhoff, and G. Streukens, "Hydrogen storage in complex metal hydrides," *Journal of the Serbian Chemical Society*, vol. 74, no. 2, pp. 183–196, 2009, doi: 10.2298/JSC0902183B.

[5] A. Züttel, P. Wenger, S. Rentsch, P. Sudan, Ph. Mauron, and Ch. Emmenegger, "LiBH4 a new hydrogen storage material," *Journal of Power Sources*, vol. 118, no. 1, pp. 1–7, May 2003, doi: 10.1016/S0378-7753(03)00054-5.

[6] Q. Lai *et al.*, "Hydrogen Storage Materials for Mobile and Stationary Applications: Current State of the Art," *ChemSusChem*, vol. 8, no. 17, pp. 2789–2825, 2015, doi: 10.1002/cssc.201500231.

[7] A. M. Abdalla, S. Hossain, O. B. Nisfindy, A. T. Azad, M. Dawood, and A. K. Azad, "Hydrogen production, storage, transportation and key challenges with applications: A review," *Energy Conversion and Management*, vol. 165, pp. 602–627, Jun. 2018, doi: 10.1016/j.enconman.2018.03.088.

[8] L. Ouyang *et al.*, "Magnesium-based hydrogen storage compounds: A review," *Journal of Alloys and Compounds*, vol. 832, p. 154865, Aug. 2020, doi: 10.1016/j.jallcom.2020.154865.

[9] E. Burzo, Ed., *Hydrogen Storage Materials*. Berlin Heidelberg: Springer-Verlag, 2018.

[10] S. Kumar, A. Jain, T. Ichikawa, Y. Kojima, and G. K. Dey, "Development of vanadium based hydrogen storage material: A review," *Renewable and Sustainable Energy Reviews*, vol. 72, pp. 791–800, May 2017, doi: 10.1016/j.rser.2017.01.063.

[11] A. Züttel, A. Remhof, A. Borgschulte, and O. Friedrichs, "Hydrogen: the future energy carrier," *Phil. Trans. R. Soc. A.*, vol. 368, no. 1923, pp. 3329–3342, Jul. 2010, doi: 10.1098/rsta.2010.0113.

[12] K. T. Møller, T. R. Jensen, E. Akiba, and H. Li, "Hydrogen - A sustainable energy carrier," *Progress in Natural Science: Materials International*, vol. 27, no. 1, pp. 34–40, Feb. 2017, doi: 10.1016/j.pnsc.2016.12.014.

[13] Ch. Lexcellent and G. Gondor, "Analysis of hydride formation for hydrogen storage: Pressure–composition isotherm curves modeling," *Intermetallics*, vol. 15, no. 7, pp. 934–944, Jul. 2007, doi: 10.1016/j.intermet.2006.11.002.

[14] D. B. Miracle and O. N. Senkov, "A critical review of high entropy alloys and related concepts," *Acta Materialia*, vol. 122, pp. 448–511, Jan. 2017, doi: 10.1016/j.actamat.2016.08.081.

[15] L. J. Bannenberg *et al.*, "Metal (boro-) hydrides for high energy density storage and relevant emerging technologies," *International Journal of Hydrogen Energy*, p. S0360319920331232, Sep. 2020, doi: 10.1016/j.ijhydene.2020.08.119.

[16] M. C. Gao, D. B. Miracle, D. Maurice, X. Yan, Y. Zhang, and J. A. Hawk, "High-entropy functional materials," *J. Mater. Res.*, vol. 33, no. 19, pp. 3138–3155, Oct. 2018, doi: 10.1557/jmr.2018.323.

[17] M. Sahlberg, D. Karlsson, C. Zlotea, and U. Jansson, "Superior hydrogen storage in high entropy alloys," *Scientific Reports*, vol. 6, no. 1, Dec. 2016, doi: 10.1038/srep36770.

[18] Y. F. Ye, Q. Wang, J. Lu, C. T. Liu, and Y. Yang, "High-entropy alloy: challenges and prospects," *Materials Today*, vol. 19, no. 6, pp. 349–362, Jul. 2016, doi: 10.1016/j.mattod.2015.11.026.

[19] X. Yang and Y. Zhang, "Prediction of high-entropy stabilized solid-solution in multi-component alloys," *Materials Chemistry and Physics*, vol. 132, no. 2–3, pp. 233–238, Feb. 2012, doi: 10.1016/j.matchemphys.2011.11.021.

[20] J.-P. Couzinié and G. Dirras, “Body-centered cubic high-entropy alloys: From processing to underlying deformation mechanisms,” *Materials Characterization*, vol. 147, pp. 533–544, Jan. 2019, doi: 10.1016/j.matchar.2018.07.015.
[21] S. Guo, C. Ng, J. Lu, and C. T. Liu, “Effect of valence electron concentration on stability of fcc or bcc phase in high entropy alloys,” *J. Appl. Phys.*, p. 6, 2011.
[22] M.-H. Tsai, K.-Y. Tsai, C.-W. Tsai, C. Lee, C.-C. Juan, and W. Yeh, “Criterion for Sigma Phase Formation in Cr- and V-Containing High-Entropy Alloys,” p. 7, 2013.
[23] Y.-F. Kao *et al.*, “Hydrogen storage properties of multi-principal-component CoFeMnTixVyZrz alloys,” *International Journal of Hydrogen Energy*, vol. 35, no. 17, pp. 9046–9059, Sep. 2010, doi: 10.1016/j.ijhydene.2010.06.012.
[24] I. Kunce, M. Polanski, and J. Bystrzycki, “Structure and hydrogen storage properties of a high entropy ZrTiVCrFeNi alloy synthesized using Laser Engineered Net Shaping (LENS),” *International Journal of Hydrogen Energy*, vol. 38, no. 27, pp. 12180–12189, Sep. 2013, doi: 10.1016/j.ijhydene.2013.05.071.
[25] I. Kunce, M. Polański, and T. Czujko, “Microstructures and hydrogen storage properties of La Ni Fe V Mn alloys,” *International Journal of Hydrogen Energy*, vol. 42, no. 44, pp. 27154–27164, Nov. 2017, doi: 10.1016/j.ijhydene.2017.09.039.
[26] P. Edalati *et al.*, “Reversible room temperature hydrogen storage in high-entropy alloy TiZrCrMnFeNi,” *Scripta Materialia*, vol. 178, pp. 387–390, Mar. 2020, doi: 10.1016/j.scriptamat.2019.12.009.
[27] V. Zadorozhnyy *et al.*, “Evaluation of hydrogen storage performance of ZrTiVNiCrFe in electrochemical and gas-solid reactions,” *International Journal of Hydrogen Energy*, vol. 45, no. 8, pp. 5347–5355, Feb. 2020, doi: 10.1016/j.ijhydene.2019.06.157.
[28] S.-K. Chen, P.-H. Lee, H. Lee, and H.-T. Su, “Hydrogen storage of C14-CruFevMnwTixVyZrz alloys,” *Materials Chemistry and Physics*, vol. 210, pp. 336–347, May 2018, doi: 10.1016/j.matchemphys.2017.08.008.
[29] M. M. Nygård, G. Ek, D. Karlsson, M. Sahlberg, M. H. Sørby, and B. C. Hauback, “Hydrogen storage in high-entropy alloys with varying degree of local lattice strain,” *International Journal of Hydrogen Energy*, vol. 44, no. 55, pp. 29140–29149, Nov. 2019, doi: 10.1016/j.ijhydene.2019.03.223.
[30] D. Karlsson *et al.*, “Structure and Hydrogenation Properties of a HfNbTiVZr High-Entropy Alloy,” *Inorganic Chemistry*, vol. 57, no. 4, pp. 2103–2110, Feb. 2018, doi: 10.1021/acs.inorgchem.7b03004.
[31] I. Kunce, M. Polanski, and J. Bystrzycki, “Microstructure and hydrogen storage properties of a TiZrNbMoV high entropy alloy synthesized using Laser Engineered Net Shaping (LENS),” *International Journal of Hydrogen Energy*, vol. 39, no. 18, pp. 9904–9910, Jun. 2014, doi: 10.1016/j.ijhydene.2014.02.067.
[32] G. Zepon *et al.*, “Hydrogen-induced phase transition of MgZrTiFe0.5Co0.5Ni0.5 high entropy alloy,” *International Journal of Hydrogen Energy*, vol. 43, no. 3, pp. 1702–1708, Jan. 2018, doi: 10.1016/j.ijhydene.2017.11.106.
[33] J. Montero, C. Zlotea, G. Ek, J.-C. Crivello, L. Laversenne, and M. Sahlberg, “TiVZrNb Multi-Principal-Element Alloy: Synthesis Optimization, Structural, and Hydrogen Sorption Properties,” *Molecules*, vol. 24, no. 15, p. 2799, Jul. 2019, doi: 10.3390/molecules24152799.
[34] H. Shen *et al.*, “A Novel TiZrHfMoNb High-Entropy Alloy for Solar Thermal Energy Storage,” *Nanomaterials*, vol. 9, no. 2, p. 248, Feb. 2019, doi: 10.3390/nano9020248.
[35] C. Zhang, Y. Wu, L. You, X. Cao, Z. Lu, and X. Song, “Investigation on the activation mechanism of hydrogen absorption in TiZrNbTa high entropy alloy,” *Journal of Alloys and Compounds*, vol. 781, pp. 613–620, Apr. 2019, doi: 10.1016/j.jallcom.2018.12.120.
[36] C. Zlotea *et al.*, “Hydrogen sorption in TiZrNbHfTa high entropy alloy,” *Journal of Alloys and Compounds*, vol. 775, pp. 667–674, Feb. 2019, doi: 10.1016/j.jallcom.2018.10.108.

[37] H. Shen *et al.*, “Compositional dependence of hydrogenation performance of Ti-Zr-Hf-Mo-Nb high-entropy alloys for hydrogen/tritium storage,” *Journal of Materials Science & Technology*, Jan. 2020, doi: 10.1016/j.jmst.2019.08.060.

[38] M. O. de Marco, Y. Li, H.-W. Li, K. Edalati, and R. Floriano, “Mechanical Synthesis and Hydrogen Storage Characterization of MgVCr and MgVTiCrFe High-Entropy Alloy,” *ADVANCED ENGINEERING MATERIALS*. WILEY-V C H VERLAG GMBH, POSTFACH 101161, 69451 WEINHEIM, GERMANY, doi: 10.1002/adem.201901079.

[39] M. M. Nygård, G. Ek, D. Karlsson, M. H. Sørby, M. Sahlberg, and B. C. Hauback, “Counting electrons - A new approach to tailor the hydrogen sorption properties of high-entropy alloys,” *Acta Materialia*, vol. 175, pp. 121–129, Aug. 2019, doi: 10.1016/j.actamat.2019.06.002.

[40] K. Sakaki, H. Kim, K. Asano, and Y. Nakamura, “Hydrogen storage properties of Nb-based solid solution alloys with a BCC structure,” *Journal of Alloys and Compounds*, vol. 820, p. 153399, Apr. 2020, doi: 10.1016/j.jallcom.2019.153399.

CHAPTER II

~ Materials & ~ Methods

CHAPTER 2. Materials & Methods

The idea of this project is to prepare HEAs (or MPEAs) based on refractory elements in the form of **Ti-V-Zr-Nb-*M*,** where *M* is substituted by elements with different physical, chemical, and electronic properties, and to evaluate their hydrogen sorption properties using diverse characterization techniques. In this chapter, three different synthesis routes for alloy preparation will be described, along with the characterization techniques used for the evaluation of the structural and hydrogenation properties of the MPEAs.

2.1 Synthesis of the alloys and related hydrides

The alloys reported in this manuscript were prepared from pure elemental powders, or bulk pieces, and used as purchased without further treatment. Each element was weighted on microbalances Metler Toledo (±0.0001 g) according to the desired stoichiometry. Table 2.1 lists the optimized composition of the main MPEAs studied in this project. Subsequently, the metals were mixed following the protocol for each synthetic approach: powder elements were used for ball milling, while bulk pieces (sheets, rods, pellets, or chips) were used for high-temperature arc melting. The characteristics of the as purchased elements are described in Table 2.2. For the direct hydride syntheses (reactive ball milling) and the hydrogenation experiments, pure H_2 from Alphagaz grade 6 N (99,9999 %) was used with a maximum pressure of 80 bar. For neutron diffraction experiments, deuterium gas (D_2) from Alphagaz (99.999 %) was used instead of hydrogen.

Table 2.1. Optimized chemical composition of the MPEAs presently studied in this manuscript.

Alloy composition	Ti at. %	V at. %	Zr at. %	Nb at. %	Mg at. %	Al at. %	Ta at. %
Ti-V-Zr-Nb	32.5	27.5	12.5	27.5	-	-	-
Mg-Ti-V-Zr-Nb	30	25	10	25	10	-	-
Al-Ti-V-Zr-Nb	30	25	10	25	-	10	-
Ta-Ti-V-Zr-Nb	30	25	10	25	-	-	10

Table 2.2. Characteristics of the metallic elements as purchased and provider.

Element	Form	Size	Purity	Distributor
Al	powder	0.3-1.0 mm	99+%	STREM chem
Mg	powder	150-850 µm	99.8%	Alfa Aesar
Nb	powder	<250 µm	99.80%	Alfa Aesar
Ta	powder	<100 µm	99.98%	STREM chem
Ti	powder	<100 µm	99.90%	Alfa Aesar
V	flakes	1-3 mm	99.70%	Alfa Aesar
Zr	powder	<150 µm	99.50%	Alfa Aesar
Ti	slugs	6x10 mm	99.99%	Alfa Aesar
Zr	pellets	3x3 mm	99.95%	Neyco
Nb	rods	10 mm dia.	99.95%	Alfa Aesar
V	chips	5x5 mm	99.70%	Alfa Aesar
Ta	sheet	0.05 mm thick	99.76%	Alfa Aesar

2.1.1 High-energy ball milling

High-energy ball milling (HEBM) is a mechanical alloying process in which powdered metals are alloyed by the collision of grinding balls inside a mill, fusing the elements (cold-welding), reducing the particle size to µm range and crystallite size to the nm scale[1]. There are different ball milling instruments, or setups, which are characterized by the motion of the mill, namely: attritor, vibrational (or shaker), drum, horizontal, and planetary mills. Planetary mills are one of the preferred instruments at a laboratory scale due to its high efficiency for alloying, yielding a fine and homogeneous powder material suitable to study the properties of alloys and nanocomposites[2].

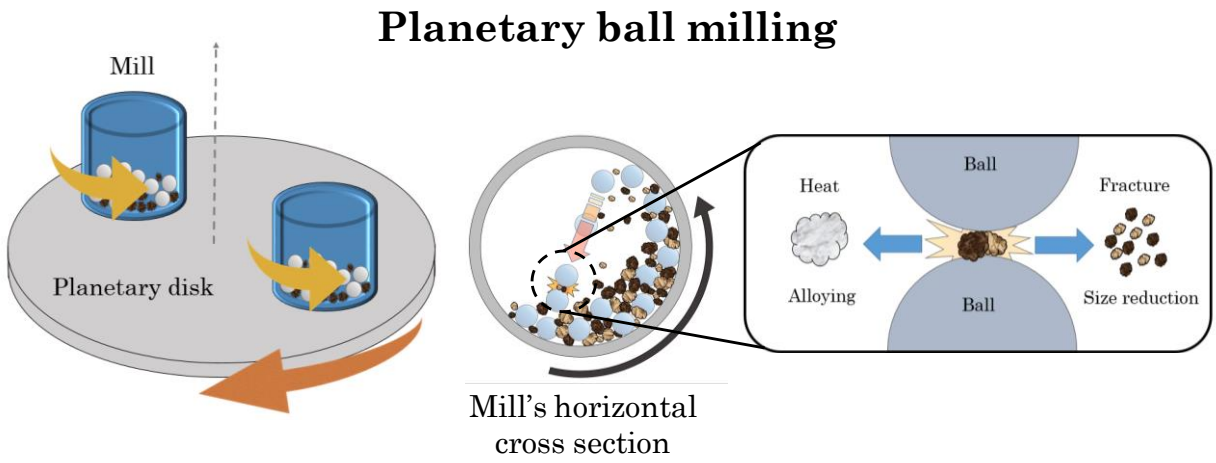

Figure 2.1. Planetary milling sketch and description of the mechanical alloying process.

In planetary instruments (Figure 2.1), the milling principle relies on the fast circulatory motion of grinding balls inside a cylindrical mill supported on a planetary disk, which rotates at high speed in the axial direction. Some ball milling instruments allow the independent rotation of the mill from that of the support disk in opposite direction to increase the relative speed of the grinding balls inside the mill. The energy to fuse the elements is introduced by means of mechanical force (kinetic energy) by the collision of two accelerated grinding balls as depicted in Figure 2.1. The crushed elements are then heated for a brief period reaching the fusion temperature of the metals, with thousands of collisions happening over time until the alloying is complete. Because the transfer of energy to fuse the elements is localized at the collision point, the overall temperature of the process is maintained below 100° C, appropriate for the synthesis of alloys containing elements with high-vapor pressures. In HEBM, several parameters influence the synthetic process but the most important to take into account are the rotation speed of the disk (and/or the mill), the total ball milling time, ball-to-powder weight ratio (b/p wt), and type and pressure of the gas inside the mill (inert or reactive)[1]. Under *inert* atmosphere (Ar), the synthesis produces an alloy in its *pristine* form. In *reactive* atmosphere (H_2), an *in-situ* chemical reaction with hydrogen occurs simultaneously during the alloying process, and the product of the synthesis is a direct hydride. Two experimental conditions will be further detailed for each method: Argon-Ball Milling (**ArBM**) and Reactive Ball Milling (**RBM**).

Argon ball milling

For this method, all sample preparation and manipulation were performed inside an Ar glove-box to avoid oxygen contamination. Each MPEA was prepared by weighing the elemental powders according to the stoichiometry in Table 2.1 (5 g per alloy), mixing the elements inside the mill with 80 cm^3 of volume. 7 mm stainless steel balls were used in a ball-to-powder weight ratio of 26:1. The mill was sealed using Viton gaskets to avoid gas leaking. The ArBM syntheses were carried out using a planetary mill from Fritsch instruments, Pulverisette 7, at a rotation speed of 700 rotation per minute (rpm), in cycles of 15 min of continuous ball milling with intervals of 15 min pause for cooling down.[1] The number of cycles and the synthesis conditions for each alloy composition are found in Table 2.3.

[1] An additional step is required for a successful and homogeneous synthesis. A hand-manipulation is critical after each 15 min of ball milling. The sample will often found itself attached onto the inner walls of the mill, as a hard crust. The crust will act as a shield against the ball-grinding and prevent the full homogeneization of the elements within. Therefore, it is necessary to scrap the crust off the walls using hard tools (e.g. chisel)

Table 2.3. Experimental conditions for ArBM synthesis in planetary mill Pulverisette 7, Fritsch, for a total mass of 5 g per alloy.

MPEA composition	disk speed	ball diameter	b/p wt ratio	ball milling time/cycle	no. of cycles
$Ti_{0.325}V_{0.275}Zr_{0.125}Nb_{0.275}$	700 rpm	7 mm	26:1	15 min	4
$Ti_{0.30}V_{0.25}Zr_{0.10}Nb_{0.25}Mg_{0.10}$	700 rpm	7 mm	26:1	15 min	8
$Ti_{0.30}V_{0.25}Zr_{0.10}Nb_{0.25}Al_{0.10}$	700 rpm	7 mm	26:1	15 min	4
$Ti_{0.30}V_{0.25}Zr_{0.10}Nb_{0.25}Ta_{0.10}$	700 rpm	7 mm	26:1	15 min	4

Reactive ball milling

Similar to ArBM, the sample preparation was carried out within an Ar glove-box. Each alloy was prepared by weighing and mixing the powdered elements with the compositions indicated in Table 2.1, with a total mass of 5 g each batch. This time, the volume of the mill is 220 cm^3 and 12 mm stainless steel balls were used in a ball-to-powder weight ratio of 60:1. Once the elements are loaded into the mill and sealed under Ar atmosphere, the mill is then taken out from the glove-box and connected to a manometric device to evacuate the Ar gas and to introduce ~70 bar of H_2. The syntheses were carried out using a planetary mill Pulverisette 4, from Fritsch, using high-pressure milling vials equipped with pressure and temperature sensors, purchased from Evicomagnetics. This instrument allows the independent rotation of the mill from the planetary disk. The speed of the disk was set to 400 rpm and 2 rpm for the mill in the opposite direction, resulting in an overall speed of 800 rpm. The syntheses were carried out in 2 hours of continuous ball milling. All synthesis details are listed in Table 2.4.

Table 2.4. Experimental conditions for RBM synthesis in a planetary mill Pulverisette 4, Fritsch. Each batch was made of 5 g total mass, the free-volume of the milling vial is about 166(±2) cm^3.

MPEA composition	disk (mill) speed	overall speed	ball diameter	b/p wt ratio	H_2 pressure	BM time / cycle
$Ti_{0.325}V_{0.275}Zr_{0.125}Nb_{0.275}$	400(-2) rpm	-800 rpm	12 mm	60:1	70 bar	120 min
$Ti_{0.30}V_{0.25}Zr_{0.10}Nb_{0.25}Mg_{0.10}$	400(-2) rpm	-800 rpm	12 mm	60:1	70 bar	120 min
$Ti_{0.30}V_{0.25}Zr_{0.10}Nb_{0.25}Al_{0.10}$	400(-2) rpm	-800 rpm	12 mm	60:1	70 bar	120 min
$Ti_{0.30}V_{0.25}Zr_{0.10}Nb_{0.25}Ta_{0.10}$	400(-2) rpm	-800 rpm	12 mm	60:1	70 bar	120 min

and crush any agglomerates to ensure full homogeneity. This manipulation must be done inside an Ar glove box to prevent oxidation and be repeated after each ball milling cycle.

2.1.2 High-temperature arc melting

Arc melting is a high-temperature fusion technique (HT-AM) widely used in the production of alloys at the industrial level, e.g. in steel manufacture, but it is also commonly found in laboratories at a smaller scale. Contrary to other high-temperature techniques in which the temperature is increased by heat radiation, HT-AM uses an electric discharge to melt and fuse the elements.

A typical laboratory arc melting instrument consists of a vacuum chamber containing two electrodes set at low potential difference (voltage) and connected to a welder generator to supply an electron current. When the current is high enough, an electric arc is created between the electrodes passing through the material inside the sample chamber, as illustrated in Figure 2.2. The flow of electrons heats the metals above their melting point until the fusion of the elements takes place. The MPEAs were synthesized using a homemade arc melting furnace with a tungsten tip used as the cathode, and a water-cooled copper crucible was used as the anode and sample holder.

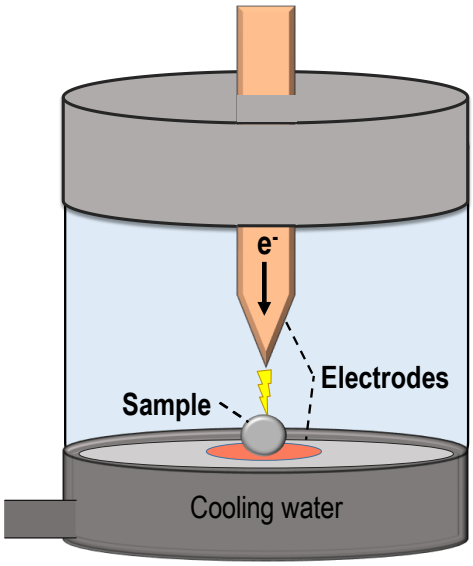

Figure 2.2. Schematic representation of the high-temperature arc melting instrument at ICMPE.

Each MPEA was prepared by cutting and weighting bulk pieces of the elements for a total mass of 3 g per alloy. The metals were placed into the copper crucible and evacuated using secondary vacuum (10^{-5} mbar) for 2 hours. Next, around 400 mbar of Ar were introduced as the inert atmosphere. The welder generator was set to supply a constant current of 90 amperes and the electric discharge was maintained for nearly 60 seconds in each melting. The alloy was re-melted 15-20 times to ensure complete homogeneity of the elements, flipping the ingot over after each melting.

2.1.3 Hydride synthesis: hydrogenation of alloys

Under certain pressure and temperature conditions, metals can have a spontaneous reaction with hydrogen leading to the formation of a hydride, as described in Chapter 1. Several characterization techniques require the use of full hydrides to study the hydrogen sorption properties, and these were directly prepared after the alloy syntheses (HTAM and ArBM) using a manometric device based on the Siervet's methodology[3].

Approximately 500 mg of each MPEA were hydrogenated (or deuterated) at 25 °C with a final equilibrium pressure of ~25 bar of H_2 (or D_2). For this, the alloys were loaded into a stainless-steel tube of known volume, sealed with commercial metal gaskets to prevent from leaking, and then connected onto the manometric Sievert's device. All samples were activated prior to hydrogenation by heating the sample in a resistance furnace at a constant temperature of 340 °C, while evacuating the cell for 2 hours with a base pressure of at least 10^{-3} mbar. Table 2.5 contains a general description of the experimental conditions used for the hydrogenation of the alloys.

Table 2.5. Experimental conditions for the hydrogenation of MPEAs (500 mg) on a Sievert's device using a stainless steel sample holder with calibrated volume.

MPEA composition	gas	P_{eq}	allowed absorption time	synthesis method
$Ti_{0.325}V_{0.275}Zr_{0.125}Nb_{0.275}$	H_2/D_2	25 bar	2 h	HTAM and ArBM
$Ti_{0.30}V_{0.25}Zr_{0.10}Nb_{0.25}Mg_{0.10}$	H_2/D_2	25 bar	2 h	ArBM
$Ti_{0.30}V_{0.25}Zr_{0.10}Nb_{0.25}Al_{0.10}$	H_2/D_2	25 bar	2 h	HTAM
$Ti_{0.30}V_{0.25}Zr_{0.10}Nb_{0.25}Ta_{0.10}$	H_2/D_2	25 bar	2 h	HTAM

2.2 Hydrogen absorption characterization

The understanding of the hydrogen sorption properties in metals and porous materials is crucial for the development of H_2 storage units, and these properties are often evaluated in terms of maximum hydrogen capacity, kinetics of absorption, and thermodynamics of reaction. The hydrogen storage capacity in metals and alloys is determined from the number of hydrogen moles absorbed divided by the moles of the metal (or alloy), described as elemental hydrogen per metal atom (H/*M*). Hydrogen capacity is also reported in the literature as weight percent, *wt.%*, which is determined by the mass (*m*) of the material and hydrogen instead:

$$wt.\% = \left(\frac{m_{H_2}}{m_{H_2}+m_{metal}}\right) x100 \qquad \text{Equation 2.1}$$

The hydrogen absorption properties of the MPEAs were evaluated using manometric techniques based on the Sievert's methodology.

2.2.1 Sievert's methodology

A common method to determine the hydrogen absorption/desorption properties in materials is by measuring the pressure change during the hydrogenation reaction. The relationship between the number of moles and the pressure of a gas can be generally described by the formula for ideal gases (Equation 2.2)

$$\boldsymbol{P}V = \boldsymbol{n}RT \qquad \text{Equation 2.2}$$

where P is the pressure of the gas, V is the volume, n the number of moles of the gas, R the gas constant, and T is the temperature. In a closed system under isothermal and isochoric conditions (constant temperature and constant volume) the pressure change during the reaction, ΔP, is equivalent to the number of moles absorbed/desorbed by the material, Δn, described as it follows

$$\boldsymbol{\Delta P}V = \boldsymbol{\Delta n}RT \qquad \text{Equation 2.3}$$

However, to correct from the ideal behavior of gases, additional elements are introduced into the equation, like gas compressibility, and therefore the *real gas* equation is used instead[3]. The hydrogen pressure can be determined using the experimental database of real gases from the National Institute of Standards and Technology (NIST). The calculations for the hydrogen storage capacity in this project were carried out using a homemade Macro Excel file (Microsoft office) or automatically given by the PCT-Pro 2000 SETARAM instrument (an automatic Sievert's device).

The Sievert's methodology uses this principle to measure the hydrogen capacity of materials in manometric devices, which typically consist of two chambers with calibrated and thermostated volumes (a reservoir and a sample holder) joined together by an isolation valve and connected to a vacuum line and H_2 supply. A pressure gauge in the reservoir measures the pressure of the system during the hydrogenation reaction. A typical Sievert's device is illustrated in Figure 2.3.

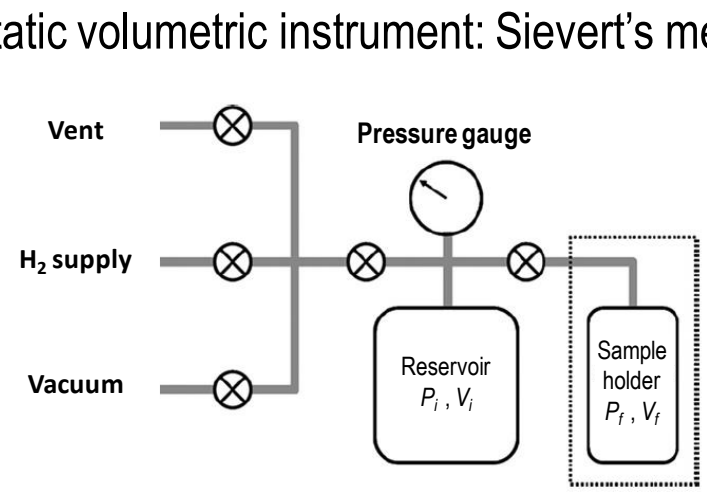

Figure 2.3. Schematic representation of a Sievert's instrument and principal components for the measurement of the hydrogen capacity.

In the Sievert's method, the reservoir is filled with hydrogen gas up to a pressure level while the sample holder is initially under static vacuum. When the isolation valve is opened, the volume of the gas expands and the pressure decreases, this relationship is described by Boyle's equation for isothermal conditions (Equation 2.4)

$$P_i V_i = P_f V_f \qquad \text{Equation 2.4}$$

where P and V are the pressure of the initial and final state. The sample inside the sample holder then absorbs H_2 further decreasing the gas pressure, and so the pressure change by absorption, ΔP, is equivalent to the hydrogen capacity of the material. Figure 2.4 shows highlights the different steps during a typical pressure measurement in a Sievert's device. Different absorption properties can be studied based on the Sievert's method: kinetics of absorption/desorption, pressure-compositions isotherms, and life-cycle performances.

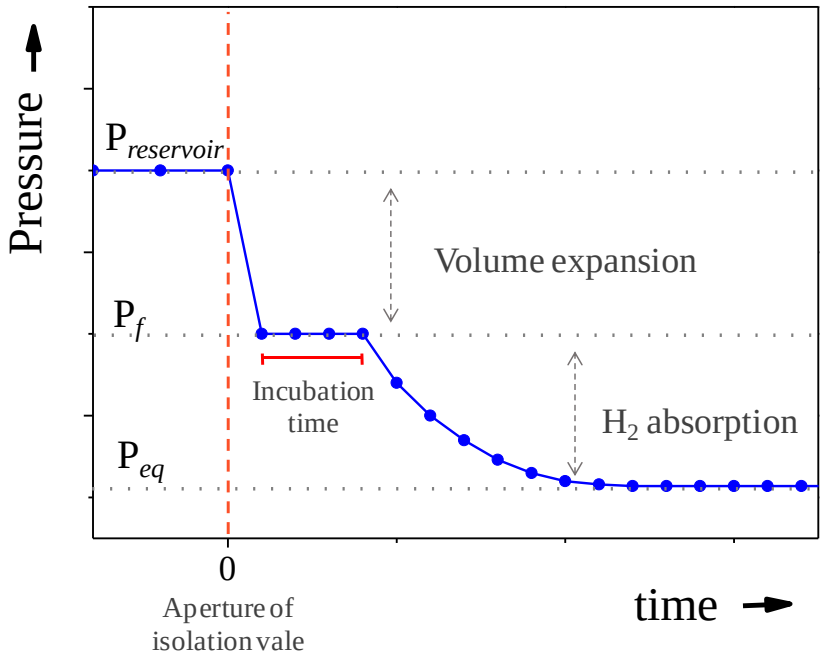

Figure 2.4. Pressure measurement in a Sievert's device and the characteristics of the hydrogen absorption curve. At t= 0, the isolation valve at the reservoir is open and the pressure drops due to volume expansion of the gas. In some cases, the hydrogenation reaction does not occur instantly and the pressure remains stable for a period known as the incubation time. Subsequently, the hydrogenation reaction takes place and the pressure further decreases due to hydrogen absorption, revealing what is known as the kinetic curve of absorption.

2.2.2 Kinetics of absorption

This study was performed to obtain general information about the MPEA absorption properties. The kinetic curve as depicted in Figure 2.4 reveals information about the speed of the hydrogenation process, the time for absorption, the maximum hydrogen capacity, and the incubation time if any. The measurement was prepared by loading ~300 mg of the sample into a stainless steel cell and sealed using metal gaskets, and subsequently connected to a manometric device. The sample was activated by heat treatment and then exposed to an initial pressure of around 40 bar, resulting in a final equilibrium pressure around 25 bar. The pressure was continuously recorded in isothermal conditions, and the temperature was thermostated using a water bath at 25 °C, or a resistance furnace for higher temperatures.

2.2.3 Pressure-composition isotherms

Pressure-composition-isotherm (PCI) is a measurement that allows the identification of the equilibrium pressure for hydride formation, the reversible storing capacity of the material, and

identification of possible phase transitions during hydrogenation[4]. These characteristics are embedded in a PCI curve, as illustrated in Figure 2.5.

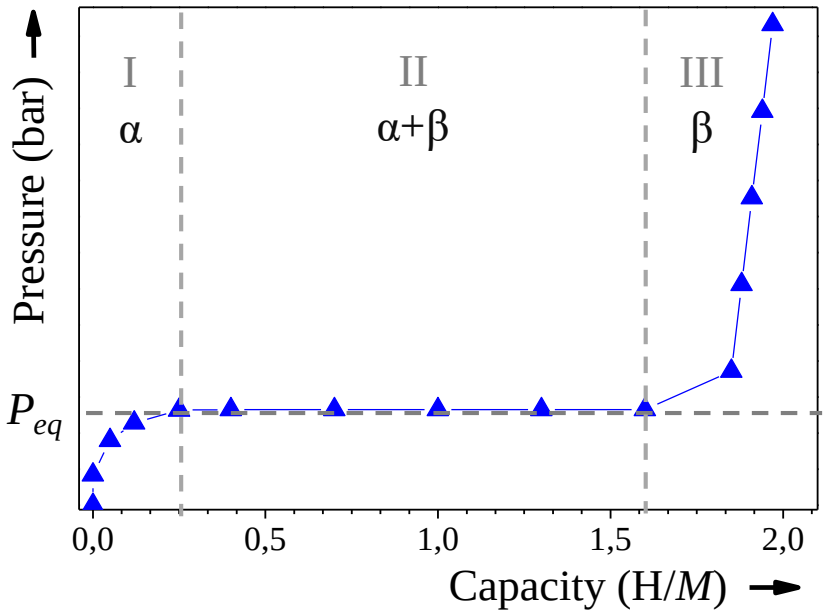

Figure 2.5. Characteristics in a typical PCI curve. A single plateau represents the transition from the α and β phase during hydrogenation, where α is a solid solution and β is the hydride phase.

The PCI curve illustrates the phase transition of the alloy during hydride formation and can be divided into three main stages: (*I*) the formation of the solid solution, *α*, (*II*) the formation of the hydride phase, β, in coexistence with the α-phase, and (*III*) the complete transformation to the β-phase at maximum H/*M*. These stages are defined by the plateau pressure where the α-phase coexists with the β-phase.

The PCI, in absorption, is measured by exposing the sample to a small dose of H_2 and wait for the reaction to reach equilibrium. The equilibrium pressure is then recorded and another dose of H_2 is then introduced. These steps are repeated by applying small increments of pressure until the sample shows no further hydrogen absorption. The equilibrium pressure at each point is then plotted as a function of hydrogen absorbed (H/*M*). These will result in a collection of points at discrete stages during the hydrogenation process. The same principle can be applied to construct a PCI plot during hydrogen desorption, using the same equations as before (Equation 2.3 and 2.4). However, at the starting point, the sample is fully hydrogenated and the pressure at the reservoir is decreased step by step and the equilibrium pressure is then recorded.

The PCI measurements were carried out using both, an automated Sievert apparatus PCTPro-2000, from SETARAM Instrumentations, and a home-made manometric device with calibrated volumes. All MPEA underwent the same activation treatment before the hydrogenation, which consisted of heating the sample to 340 °C under dynamic vacuum for 2 hours (10^{-3} mbar). Most of the PCIs were measured at 25 °C in a temperature-controlled water bath, or at a higher temperature using a resistance furnace.

2.2.4 Hydrogenation cycling test

Other important properties for hydrogen storage materials, besides their maximum capacity and kinetics, are the life-cycle and reversibility of the absorption/desorption reaction over several hydrogenation cycles. It is known that alloys can suffer from hydrogen-induced decomposition where the material loses part of its capacity due to irreversible structural deformation, e.g. phase segregation. This evaluation consists of measuring the hydrogen storage capacity of the alloys over several hydrogen absorption and desorption cycles.

Between 300-500 mg of the MPEAs were loaded into a stainless steel cell and submitted to activation before the first hydrogenation cycle, heating the sample under dynamic vacuum (340 °C, 10^{-5} mbar). All cycling tests were carried out at 25 °C and a final equilibrium pressure of 25 bar. Hydrogen desorption was carried out by heating the sample to 350-400 °C under a continuous secondary vacuum for 4-10 hours (10^{-5} mbar). All experimental conditions are listed in Table 2.6 for each alloy composition.

Table 2.6. Experimental conditions for the evaluation of the hydrogen-cycling properties.

MPEA composition	Absorption (25 bar H2)		Desorption (vacuum, 10^{-6} mbar)		No. of cycles	Synthesis method
	temp.	time	temp.	time		
$Ti_{0.325}V_{0.275}Zr_{0.125}Nb_{0.275}$	25 °C	2 h	340 °C	4 h	20	HTAM
$Ti_{0.30}V_{0.25}Zr_{0.10}Nb_{0.25}Mg_{0.10}$	25 °C	2 h	400 °C	10 h	12	ArBM
$Ti_{0.30}V_{0.25}Zr_{0.10}Nb_{0.25}Al_{0.10}$	25 °C	2 h	400 °C	10 h	20	HTAM
$Ti_{0.30}V_{0.25}Zr_{0.10}Nb_{0.25}Ta_{0.10}$	25 °C	2 h	400 °C	10 h	20	HTAM

2.3 Thermal analyses

To study the hydrogen desorption properties of the MPEAs, the corresponding hydride phases were characterized by two thermal techniques: thermo-desorption spectroscopy and differential scanning calorimetry. These techniques provide complementary information about the properties of the MPEAs during hydrogen desorption, such as the onset temperature of desorption, kinetics, phase transition, among others. Differential scanning calorimetry characterization was performed at the University of Saõ Carlos, Brazil, as part of two months of international collaboration from the French-Brazilian program COFECUB-CAPES.

2.3.1 Thermo-desorption spectroscopy

Thermo-desorption spectroscopy (TDS) is a characterization technique used to study the desorption behavior of the hydrides by supplying thermal energy at a constant heating rate while under dynamic vacuum. Upon heating, the thermal energy destabilizes the hydride phase, causing hydrogen to desorb from the material in the form of a gas[5]. A mass-spectrometer is coupled to the instrument to analyze the gases during desorption. The partial pressure of the hydrogen released is then plotted as a function of temperature revealing a desorption profile, where certain information can be subtracted such as the onset temperature for desorption (T_{onset}) and the temperature at maximum desorption rate (T_{max}).

TDS measurements were performed in a homemade instrument (Figure 2.6) that consists of a quadrupole mass spectrometer (QMS), Microvision Plus RGA from MKS instruments, connected to a vacuum rig and a turbopump for secondary vacuum pressure (10^{-6} mbar). A silica tube, which holds the sample, is connected at the instrument and placed inside an electric furnace. The temperature of the sample is monitored by a thermocouple in close contact with the material.

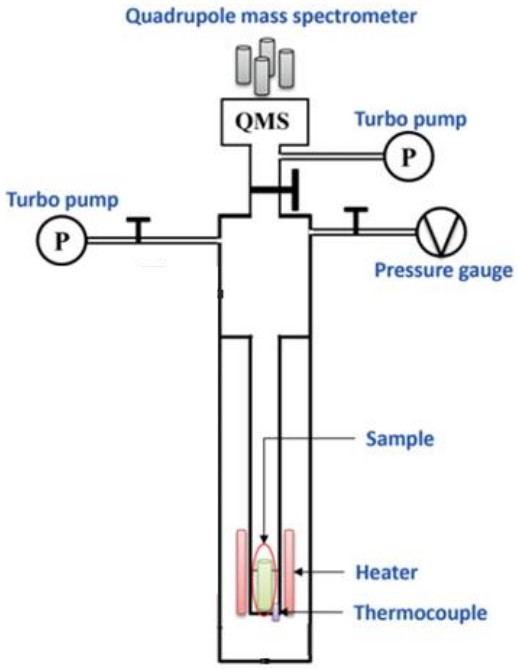

Figure 2.6. Schematic representation of the TDS instrument at the ICMPE and its components for the measurement of the hydrogen desorption properties.

A common TDS experiment was carried out by weighing 10-15 mg of the hydride and loaded into an aluminum crucible. The crucible was then mounted next to the thermocouple and placed inside the silica tube. The system was left under secondary vacuum for 1 hour, or until a base pressure reached 10^{-6} mbar. Each MPEAs were measured at a constant heating rate and heated by an electric furnace (T_{rate}= 1.0 °C/min).

2.3.2 Differential scanning calorimetry

Similar to TDS, differential scanning calorimetry (DSC) is another technique used to study the desorption properties of hydrides as a function of temperature. The main difference is that the DSC method measures the heat exchanged during the desorption reaction. The heat is calculated by measuring the temperature change during hydrogen desorption in adiabatic conditions and determined by the heat capacity of the alloy. The DSC method also incorporates a twin-test using a blank measurement as a reference to improve the precision of the measurement (Figure 2.7). The direction of the DSC signal indicates the nature of the reaction, endo- or exothermic. Additionally, the DSC curve can reveal other reactions, or processes, occurring upon heating such as, phase

transitions, chemical decomposition, or melting, to mention a few examples for metallic materials[6].

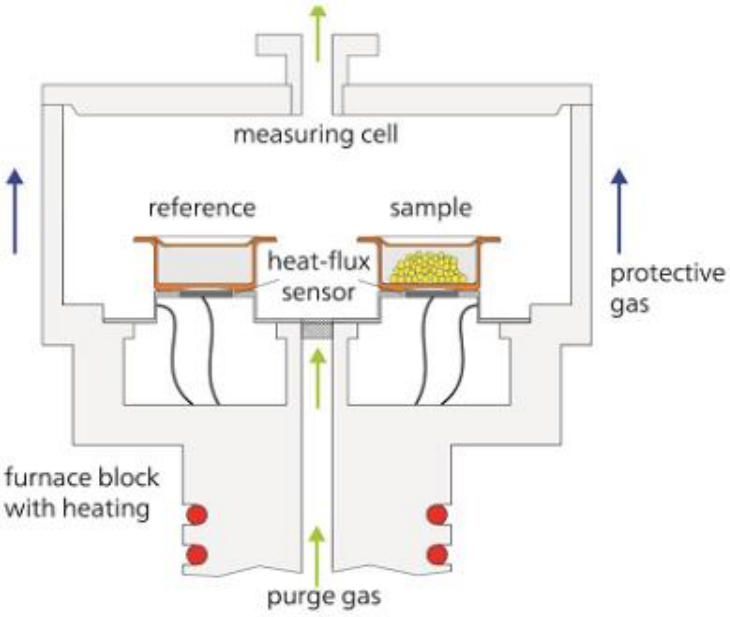

Figure 2.7. Schematic representation of the DSC instrument at Saõ Carlos University using a twin-measurement setup. The image is taken from https://www.netzsch-thermal-analysis.com/.

The DSC instrument at Saõ Carlos University, Brazil, consisted of a DSC apparatus (DSC 214) with incorporated thermo-gravimetric microbalances (STA 449C Jupiter) for in-situ thermo-gravimetric analysis (TGA) and coupled to a QMS (QMS 403 C Aëolos) for complementary characterization, all from Netzsch instruments. A typical measurement consisted of loading 10-20 mg of the hydride into an aluminum crucible and mounted into the instrument, along with a blank crucible. A constant flow of Ar, 10 ml/min, was used to purge the desorbed gases. A temperature ramp was set from 40 °C up to 600 °C, and a T_{rate}= 10 °C/min. The DSC signal and ion count from QMS are collected and plotted as a function of temperature.

2.4 Structural characterization: diffraction techniques

The most effective way to study the structural properties of a material is by exploiting the diffraction phenomena, where a radiation wave is coherently scattered by a crystalline material. The periodicity in the crystalline material causes interference of the scattered waves, and act constructively at specific angles, revealing a diffraction pattern over a wide range of diffraction angles. The structural

properties of the material can then be subtracted from the diffraction pattern by a structural refinement, such as the crystal structure, lattice parameters, atom position in the unit cell, phases, etc[7], [8].

2.4.1 Principle of diffraction

Any diffraction characterization is based on Bragg's law, describing a diffraction over a planar and periodical array of atoms and establishing a relationship between the diffraction angle, the wavelength, and the interplanar spacing. An incoming monochromatic beam with wave vector k is diffracted with an angle perpendicular to the plane, with a wave vector k' (see Figure 2.8). The angle between both vectors is known as the Bragg angle, 2θ. Since we are only considering coherent scattering, $|k|$ and $|k'|$ must have identical length, $1/\lambda$. When a second wave is diffracted by the plane below, k'', it travels an extra length, 2Δ, due to the distance between the diffracting planes, d_{hkl}. Most of the time, the extra traveled distance causes the wave vectors k' and k'' to be out-of-phase, resulting in destructive interference. Bragg's equation tells us that constructive interference (or diffraction) will only occur when 2Δ is an integer multiply of the radiation wavelength, $n\lambda$.

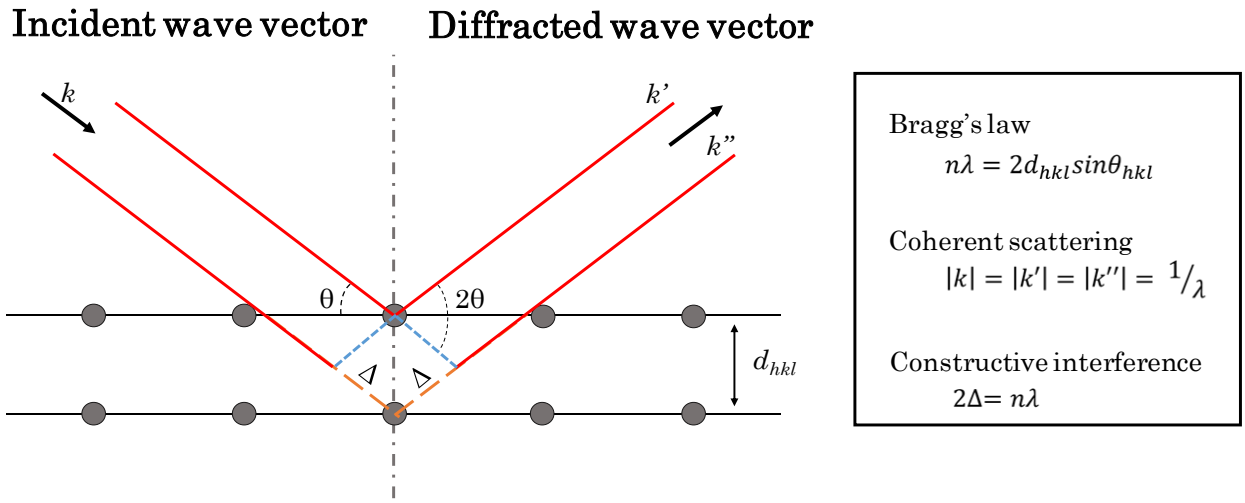

Figure 2.8. Geometrical representation of Bragg's law and coherent scattering of the wave by crystal planes hkl.

Many diffractometers use the Bragg-Brentano geometry to collect the diffraction signals as a function of Bragg angle, as pictured in Figure 2.9. In this configuration, the radiation source and the detector are mounted onto two mechanical arms in symmetrical positions and move accordingly to scan over a wide range of 2θ, while the sample remains still and flat. X-rays and neutrons are the two most common radiation probes used for structural characterization.

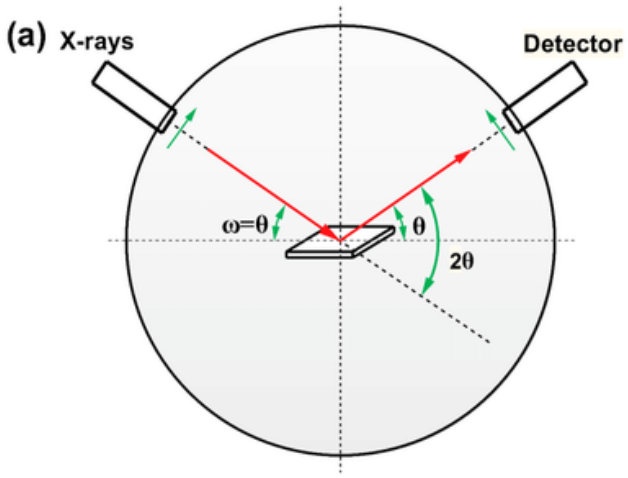

Figure 2.9. Illustration of the Bragg-Brentano geometry in laboratory powder X-ray diffraction.

2.4.2 Laboratory X-ray diffraction

X-ray radiation is one of the most common probes used to study diffraction (XRD) due to easy accessibility in laboratory instruments, generating wavelengths with magnitudes close to the unit cell parameters of many crystalline materials. In laboratory XRD, X-rays are produced by bombarding electrons towards a metal target, exciting the core electrons of the atom and emitting characteristic X-rays by the photo-emission effect. Here, a Bruker D8 Advance powder diffractometer was used for the structural characterization of the MPEAs before and after hydrogenation. The characteristic X-rays come from the K_α emission from a copper anticathode with wavelength λ= 1.5406 Å. And the scanning ranged from 20-90° in 2θ domain.

2.4.3 Synchrotron radiation X-ray diffraction

Synchrotron radiation (SR-XRD) is a more powerful source for X-ray diffraction, using high energy X-rays of 3-40 keV[9]. In SR-XRD, electrons are accelerated near the speed of light and injected into a vacuum ring. The highly energetic electrons are bent using strong magnetic coils to run through the circumference of the ring. The change in the trajectory of the electron beam releases electromagnetic radiation, X-rays, with small and tunable wavelengths. There are many advantages of SR-XRD over laboratory XRD, few worth mentioning are: the radiation wave from SR sources has a higher brightness and brilliance than that from laboratory X-rays, which improves the signal-to-noise ratio and reduces the time of acquisition for measurement; the X-ray beam is highly

collimated, and monochromatic, granting a better 2θ angle resolution, and; the energy spectrum for X-rays produced in SR can be tuned on command for different purposes[10].

SR-XRD measurements were performed at the Cristal beamline in SOLEIL synchrotron facilities in France. The hydride samples were prepared by grinding the material below 20 μm particle size using a hand-pestle and mortar and subsequently loaded into capillary tubes of 0.1 and 0.2 mm of diameter. The silica capillary was cut to 5 cm length and sealed using a torch. The energy of the X-rays was set to 17.008 keV, equivalent to a wavelength of λ= 0.72896 Å. The acquisition time was of 10 minutes approximately in a scanning range from 1° - 85° (2θ) and the collection of data was carried out using a Debye-Scherrer (or capillary) geometry.

2.4.4 Neutron diffraction

Neutrons are small particles that show wave-like properties such as interference due to the wave-particle dualism proposed by Louis de Broglie. This allows the use of neutrons as a probe to exploit Bragg's law of diffraction. There are some notable differences when using X-rays and neutrons as diffraction probes due to their nature and interaction with matter. X-rays are electromagnetic waves that are scattered from the interaction with the electron cloud, and its cross-section typically increases whit the atomic number, *Z*. Lightweight elements such as hydrogen have none-to-little interaction with X-rays. Elements with low, or none, scattering cross-section are considered transparent to diffraction. On the other hand, neutrons are non-charged particles that will interact mainly with the nuclei of the atom. The size of the cross-section in neutron scattering does not follow a trend in the periodic table of the elements and instead, this seems random. Interestingly, neutrons have a significant large cross-section for smaller elements like hydrogen, and can even discriminate between its isotopes (Figure 2.10). This is particularly attractive for the structural characterization of hydrides because it allows to locate hydrogen within the unit cell. Although, hydrogen is usually replaced with deuterium to have a better diffraction resolution. It is because of these differences that neutron and X-ray diffraction are complementary techniques for structural characterization.

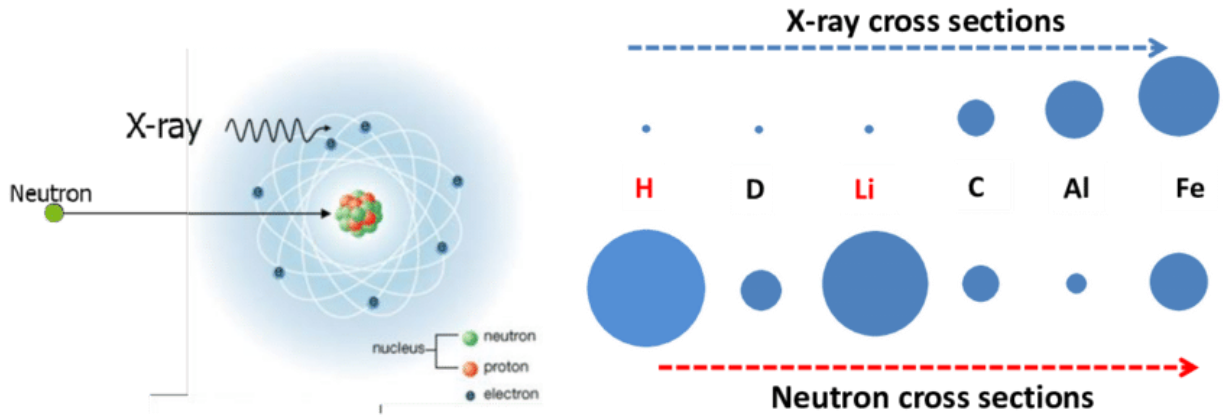

Figure 2.10. Schematic representation and main differences of interaction between X-ray and neutron diffraction. The cross-section size for X-rays and neutrons is a vague representation and these are not scale relative to each other.

Neutron diffraction characterization was carried out at the Institut Laue-Langevin in Grenoble, at the D1B beamline for neutron diffraction, using thermalized neutrons flux with wavelength λ= 1.28 Å. The *ex-situ* neutron characterization of MPEAs was done on the deuteride phases at room temperature using a vanadium can as the sample holder. Additionally, *in-situ* neutron diffraction experiments were performed during deuterium desorption to study the phase transformation of the material. For this experiment, approximately 3 g of each alloy were loaded into a silica tube capable to withstand high vacuum pressures (10^{-6} mbar), and placed inside a furnace. The tube was suspended vertically in the path of the neutron beamline and connected to the vacuum rig from the top. The sample was then heated at a constant rate of 1 °C/min and the diffraction data were collected from 1° - 128° with a 0.1° step in 2θ angle.

2.4.5 The Rietveld method: structural refinement

A typical diffraction pattern holds significant information about the structural properties of a material particularly given by the position (2θ), the shape, and the intensity of the diffraction peaks. This information can be subtracted from a full-pattern decomposition of the experimental diffraction pattern[7]. The Rietveld method, as it was proposed in the mid-60s, is by far the most accepted method to determine crystallographic data due to its assertiveness for structural refinement. The Rietveld method uses the experimental powder diffraction data as a scaffold, starting from a similar crystal structure, and the structural and instrumental parameters are refined

to fit the observed data in iterative calculations. The effectiveness of the fitting relies on the minimization of the function by the least square method (Equation 2.5),

$$\Phi = \sum_{i=1}^{n} w_i \left(Y_i^{obs} - Y_i^{calc}\right)^2 \qquad \text{Equation 2.5}$$

where n is the number of data points from the diffraction pattern, Y_i^{obs} and Y_i^{calc} is the observed and calculated intensity at any given point i, respectively, and w_i is the weight assigned at the ith data point determined by the variance from the observed data. Assuming diffraction from a single-phase, the integrated intensity can be calculated considering different peak-shape and intensity factors, described by Equation 2.6,

$$Y_i^{calc} = b_i + S_i \sum_{i=1}^{n} M_{hkl} \cdot LP_i \cdot A_i \cdot T_{hkl} \cdot E_{hkl} \cdot |F_{hkl}|^2 \qquad \text{Equation 2.6}$$

where b_i corresponds to the background intensity and S_i to the scale factor. M_{hkl} is the multiplicity factor accounting from multiple Bragg reflections from different crystal planes (hkl). LP_θ is the Lorentz-polarization factor related to the geometry of diffraction and takes into account partial polarization of the wave after scattering. The absorption factor, A_i, is only considered when the sample absorbs a fraction of the incident beam, this factor is often neglected in metals and alloys. T_{hkl} accounts for the preferential orientation, when crystallites tend to align in certain directions breaking the random distribution symmetry. The extinction factor, E_{hkl}, considers that a reflected beam does not reach the detector by being reflected back into the sample from a plane above. And the structure factor, $|F_{hkl}|^2$, which is the square factor of the absolute value of the structure amplitude, F_{hkl}. The structure amplitude factor accounts for the scattering ability of the atoms. When multiple atoms are in the unit cell, the amplitude of scattering is described by the complex function in Equation 2.7,

$$F_{hkl} = \sum_{j=1}^{m} g^j \cdot t^j(s) \cdot f^j(s) \cdot exp\left[2\pi i h \cdot \left(hx^j + ky^j + lz^j\right)\right] \qquad \text{Equation 2.7}$$

where m is the number of atoms in the unit cell, g^j is the population factor of each atom, t^j is a temperature factor accounting for the thermal vibrations of the atoms, $s = \sin\theta_{hkl}/\lambda$, f^j is the atomic scattering factor which describes the interaction between the wave and the atom, i is a complex number, and $(hx^j + ky^j + lz^j)$ represents the fractional coordinates of the jth atom.

Other instrumental and experimental factors affecting the position and shape of the peak are also considered during the lattice refinement, e.g. the position and resolution of the detector, quality of

the radiation beam, nature of the sample (crystallite size, defects), to mention a few. These contributions are reflected in the shape and width of the diffraction peak, and these parameters are refined using a pseudo-Voigt function, a linear combination of Gaussian and Lorentzian functions. To fit the experimental peak profile, the model Thompson-Cox-Hastings pseudo-Voigt[8] was used during the structural refinement. All refinement calculations were done using Fullprof Suite, a software specially designed for crystallographic characterization using the Rietveld method[5][6].

Agreement factors

The quality of the refinement is evaluated by different factors that quantify the fitting of the calculated profile and the structural parameters against the observed ones. The figures of merit are:

weight profile residual $$R_{wp} = \left[\frac{\sum_{i=1}^{n} w_i\left(Y_i^{obs} - Y_i^{calc}\right)^2}{\sum_{i=1}^{2} w_i\left(Y_i^{obs}\right)^2}\right]^{1/2} \times 100\%$$

expected profile residual $$R_{exp} = \left[\frac{n-P}{\sum_{i=1}^{2} w_i\left(Y_i^{obs}\right)^2}\right]^{1/2} \times 100\%$$

goodness of the fit $$\chi^2 = \frac{\sum_{i=1}^{n} w_i\left(Y_i^{obs} - Y_i^{calc}\right)^2}{n-P} = \left[\frac{R_{wp}}{R_{exp}}\right]^2$$

Bragg residual $$R_B = \frac{\sum_{j=1}^{m}\left|I_j^{obs} - I_j^{calc}\right|}{\sum_{i=1}^{m} I_j^{obs}} \times 100\%$$

where n is the total number of measured points, m is the number of independent Bragg reflections, I_j^{obs} and I_j^{calc} are the integrated intensity of the jth Bragg peak (observed and calculated), and P is the number of free least-squares parameters.

From these equations, it is clear that the value for each factor should be as low as possible for a good fit. All factors, except R_B, include the contribution of the background in their calculation and thus the values are affected by the signal-to-background ratio. Because of this, the values of the agreement factors may differ between the different techniques and instruments employed (neutrons, XRD, SR-XRD) and there is not a threshold value to dictate if the refinement is good enough. However, to a certain degree, the "absolute quality" can be established by the goodness of the fitting parameter, χ^2, which is the relationship between the *weight profile residual* and the *expected profile residual*, as well as the Bragg residual factor, R_B, since this is independent of the background signal.

2.5 Microstructural characterization

It is known that hydrogen absorption and desorption can cause irreversible deformation to the material structure (e.g. phase decomposition, and/or segregation) affecting their hydrogen sorption performance over H_2 cycling. The MPEAs were characterized, before and after hydrogen-cycling, by scanning electron microscopy and energy dispersive spectroscopy to evaluate their microstructure and chemical composition.

2.5.1 Scanning electron microscopy

Scanning electron microscopy (SEM) is a high-resolution imaging technique based on the interaction between an electron beam and matter, producing a variety of signals which hold information about the sample composition and microstructure[11]. In SEM, electrons are generated by thermionic heating (e.g. field emission gun) inside a vacuum column and accelerated by an anode below the electron source. The potential difference of the anode can be controlled to tune the energy of the electron beam, 1-40 keV. The SEM column contains at least one (optic or magnetic) lens to focus the electron beam and an electromagnetic coil that bends the beam allowing the characteristic scanning feature of SEM. The main components of SEM instrument are depicted in Figure 2.11.

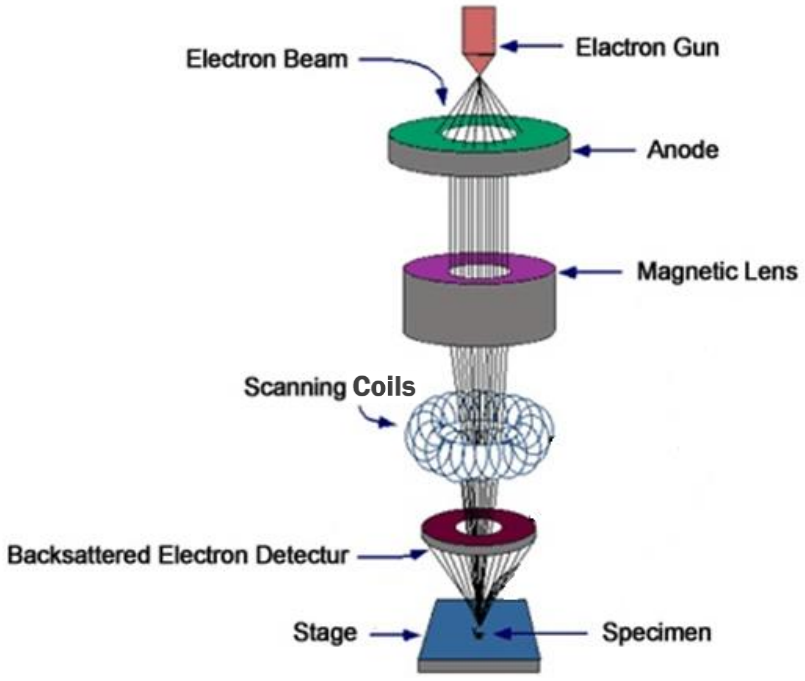

Figure 2.11. Schematic representation of a SEM instrument and its main components for microstructural characterization.

Multiple detectors may be incorporated inside the sample chamber to collect different signals from electron-matter interaction (e.g. backscattered electron detector, secondary electron detector, X-ray detector, etc.), see Figure 2.12. Since electrons are charged particles and they interact heavily with matter, these signals are usually collected from the surface of the sample, 1-10 nm in depth.

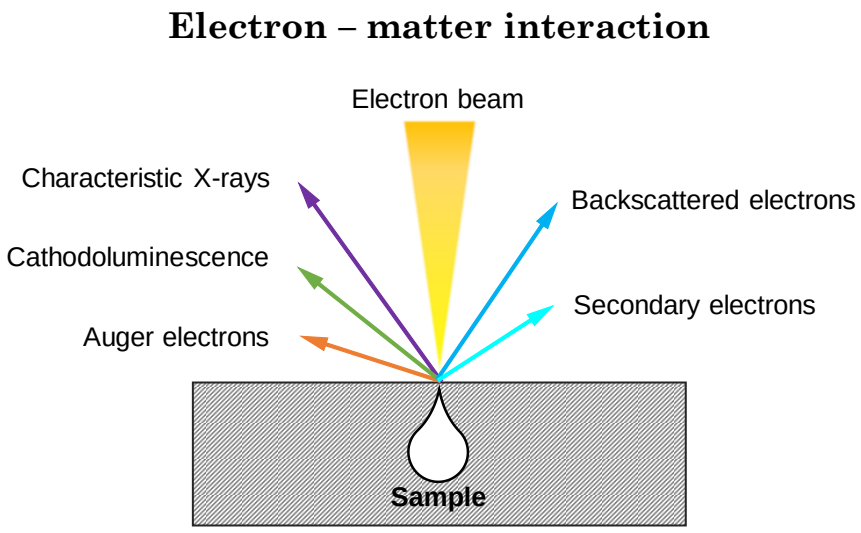

Figure 2.112. Typical signals generated from the electron-matter interaction during SEM characterization.

Back-scattered electrons (BSE) are the result of the elastic interaction of the electron beam with the sample, where the scattered electrons conserve their initial energy. This signal is collected by a BSE detector just above the sample. The number of BSE reaching the detector increases with the atomic number, and thus, heavier elements have a brighter signal. Because of this, BSE images can show different phases in the microstructure by the contrast in brightness. Secondary electrons (SE) are the result of inelastic interaction where the electron beam ionizes atoms and low-energy electrons are ejected. In contrast to BSE, SE do not provide chemical information of the sample but rather a 3D rendering image of the sample's surface and morphology.

2.5.2 Energy dispersive spectroscopy

Adding an X-ray detector into the SEM chamber allows to obtain complementary chemical information by collecting the characteristic X-rays emitted by the sample, a technique known as energy dispersive spectroscopy (EDS). One of the possible outcomes from the electron-atom interaction is the excitation of a core-electron leaving a hole. Then, an electron from a higher energy level may decay to fill the hole emitting a photon. Since electrons in the atom have discrete energy

levels and are particular for each element, the characteristic X-ray will have an electron energy equivalent to the difference between the core and shell levels of an atom. Collecting these characteristic X-rays will provide qualitative and quantitative information about the sample's chemical composition.

For SEM and EDS characterization, the hydrides in the form of coarse powder were immobilized in epoxy resin and finely polished using tissue microfiber and alumina of 3 μm. Only the hydrides from the first and last hydrogenation cycles (n= 10, or 20) were characterized by SEM-EDS. The surface of the samples was coated with a Pd layer of 1.3 nm thick. SEM characterization was performed on a Merlin SEM instrument from Carl Zeiss, using 10 keV of beam energy for scanning and chemical mapping (EDS). The chemical analysis was performed by the AZtec software from the EDS detector.

Bibliography

[1] J. Huot, D. B. Ravnsbæk, J. Zhang, F. Cuevas, M. Latroche, and T. R. Jensen, "Mechanochemical synthesis of hydrogen storage materials," *Progress in Materials Science*, vol. 58, no. 1, pp. 30–75, Jan. 2013, doi: 10.1016/j.pmatsci.2012.07.001.

[2] O. D. Neikov, "Introduction," in *Handbook of Non-Ferrous Metal Powders (Second Edition)*, O. D. Neikov, S. S. Naboychenko, and N. A. Yefimov, Eds. Oxford: Elsevier, 2019, pp. xvii–xxi.

[3] T. P. Blach and E. MacA. Gray, "Sieverts apparatus and methodology for accurate determination of hydrogen uptake by light-atom hosts," *Journal of Alloys and Compounds*, vol. 446–447, pp. 692–697, Oct. 2007, doi: 10.1016/j.jallcom.2006.12.061.

[4] Ch. Lexcellent and G. Gondor, "Analysis of hydride formation for hydrogen storage: Pressure–composition isotherm curves modeling," *Intermetallics*, vol. 15, no. 7, pp. 934–944, Jul. 2007, doi: 10.1016/j.intermet.2006.11.002.

[5] A. M. de Jong and J. W. Niemantsverdriet, "Thermal desorption analysis: Comparative test of ten commonly applied procedures," *Surface Science*, vol. 233, no. 3, pp. 355–365, Jul. 1990, doi: 10.1016/0039-6028(90)90649-S.

[6] J. F. Fernández, F. Cuevas, and C. Sánchez, "Simultaneous differential scanning calorimetry and thermal desorption spectroscopy measurements for the study of the decomposition of metal hydrides," *Journal of Alloys and Compounds*, vol. 298, no. 1, pp. 244–253, Feb. 2000, doi: 10.1016/S0925-8388(99)00620-9.

[7] V. Pecharsky and P. Zavalij, *Fundamentals of Powder Diffraction and Structural Characterization of Materials, Second Edition*, 2nd ed. Springer US, 2009.

[8] J. Rodriguez-Carvajal, "FULLPROF: a program for Rietveld refinement and pattern matching analysis," in *satellite meeting on powder diffraction of the XV congress of the IUCr*, 1990, vol. 127.

[9] F. Baudelet, R. Belkhou, V. Briois, A. Coati, P. Dumas, and Al. Et, "Soleil a New Powerful Tool for Materials Science," *Oil & Gas Science and Technology - Rev. IFP*, vol. 60, no. 5, pp. 849–874, Sep. 2005, doi: 10.2516/ogst:2005060.

[10] H. Cheng *et al.*, "Synchrotron radiation X-ray powder diffraction techniques applied in hydrogen storage materials - A review," *Progress in Natural Science: Materials International*, vol. 27, no. 1, pp. 66–73, Feb. 2017, doi: 10.1016/j.pnsc.2016.12.007.

[11] W. Zhou, R. Apkarian, Z. L. Wang, and D. Joy, "Fundamentals of Scanning Electron Microscopy (SEM)," in *Scanning Microscopy for Nanotechnology: Techniques and Applications*, W. Zhou and Z. L. Wang, Eds. New York, NY: Springer, 2007, pp. 1–40.

~Preliminary results~

Preliminary Results

Prior to the main results, this chapter will discuss two preliminary studies that helped to establish the experimental conditions for the evaluation and characterization of the MPEAs in the form of Ti-V-Zr-Nb-*M*. These studies are the cornerstone for a novel strategy to study the hydrogenation properties of MPEAs and their relationship with their composition and structural properties.

(**I**)Due to the high lattice distortion in MPEAs, certain compositions tend to crystallize as a mixture of multiple phases, which is undesirable for this project. To avoid the formation of secondary phases when adding new elements into the base composition, Ti-V-Zr-Nb-*M* (*M*= Mg, Al, Ta), the chemical composition needs to be optimized and ensure the formation of only single-phased MPEAs. Therefore, the first segment of this "preliminary results" is dedicated to the optimization of the chemical composition for the quaternary and quinary alloys with the intention to obtain single-phased materials.

(**II**)Additionally, there are two common techniques for alloy preparation: one at low temperature (e.g. ball-milling - HEBM) and one at high temperature (e.g. arc melting - HT-AM), each owning advantages and limitations. Each method produces a material with certain microstructure (i.e. crystallite size, lattice defects, surface area, etc.) that can affect the hydrogen sorption properties. Thus, the second segment discusses a comparative study on the hydrogenation performance of the quaternary alloy (Ti-V-Zr-Nb with optimized composition) produced by ArbM, HT-AM, and RBM, with the purpose to establish the best synthetic approach.

(I) Chemical Optimization

The criteria to "optimize" the chemical composition is driven by the obtention of a single-phased alloys with *bcc* structure for all four compositions in this project $Ti_v V_w Zr_x Nb_y$-M_z (*M*= Mg, Al, Ta). The lattice distortion, δ, serves as a guiding parameter in search of single-phased alloys, as it was proposed by Ye *et al.*[1], where materials below a certain threshold (δ< 7-8%) tend to form single phases. Additionally, the atomic percentages, *at.%*, for each element in the system must be in agreement with the proposed definition for high entropy alloys, 5-35 at%[2].

This analysis was carried out for the quaternary MPEA and one quinary HEA prepared by ArBM, since is the only technique suitable to synthesize all MPEAs including the Mg-containing composition.

(I.I) Equimolar compositions

Quaternary alloy (TiVZrNb)

The quaternary composition in equimolar concentration $\mathbf{Ti_{0.25}\,V_{0.25}\,Zr_{0.25}\,Nb_{0.25}}$ was prepared by mixing all elements together in ArBM and has a lattice distortion of δ= 6.9 % with a VEC value of 5.5, thus the alloy is expected to form a *bcc* structure[3], [4]. The synthesis was carried out in cycles of continuous ball milling for 15 minutes followed by another 15 minutes of pause. At every 15 minutes of ball milling, a sample was analyzed by XRD to follow the phase evolution as a function of ball milling time. It is known that milling techniques tend to introduce defects into the structure due to extensive grinding.

The diffraction patterns of the synthesis over 150 minutes of total ball milling time are plotted and stacked in Figure 1. In the first 15 minutes of ball milling, multiple phases were identified corresponding mainly to the pure elemental powders. After 30 minutes of ball milling, a new phase started to grow at the expense of the initial phases. This continued until a single phase was formed at 60 minutes of ball milling, where the alloy adopted a *bcc* structure, marked with black stars (*). Further ball milling caused amorphization of the phase, manifested by a broadening of the diffraction peaks at 120 and 150 minutes. This is a common consequence in mechanical alloying

techniques like HEBM due to extensive grinding of the material, reducing the crystallite size and introducing defects into the lattice[5], [6].

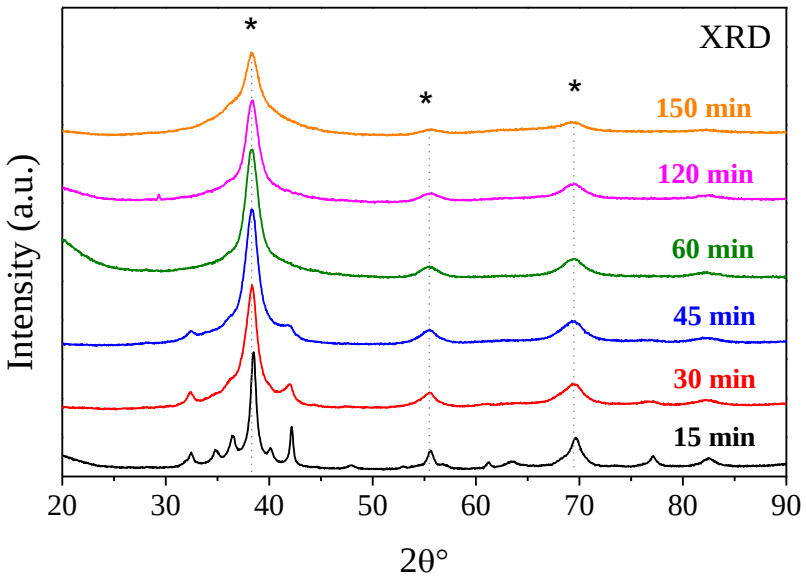

Figure 1. XRD patterns of $Ti_{0.25}V_{0.25}Zr_{0.25}Nb_{0.25}$ at different ball milling times during ArBM synthesis.

The synthesis of the quaternary alloy has an optimal ball milling time of 60 minutes to produce a single-phased alloy with minor defects. Adding a new element into the quaternary composition increases the complexity of the synthesis and phase crystallization, therefore, a similar study was carried out for a quinary alloy in equimolar composition.

Quinary alloy (MgTiVZrNb)

The next synthesis was done for the high-entropy alloy containing Mg in equimolar composition: **$Mg_{0.20}Ti_{0.20}$ $V_{0.20}$ $Zr_{0.20}$ $Nb_{0.20}$**, with a lattice distortion δ= 7.3 and VEC of 4.0. Compared to the quaternary compositions, the quinary system has a larger δ value and lower VEC. In this case, an almost single *bcc* phase was only obtained after 135 minutes of total ball milling time (Figure 2 *left*). Small diffraction contributions on the left side of the main diffraction peak at ~39° in 2θ (*magenta*) suggest the presence of a secondary phase. Phase analysis was carried out using the powder crystallographic databases PDF2 and PDF4 in EVA software from Bruker Instruments for the -samples at 15 and 135 minutes of ball milling (see Figure 2 *right*). The phase analysis suggests that

the impurity corresponds to traces of Zr, marked with the blue inverse triangle (▼). A small Fe contamination is also noticed and unavoidable in HEBM.

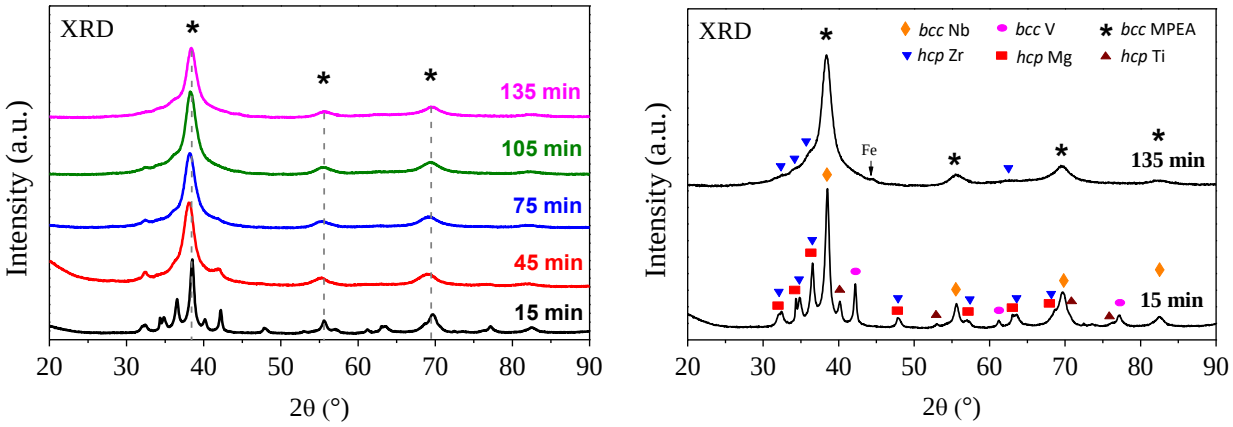

Figure 2. (left) XRD patterns of $Mg_{0.20}Ti_{0.20}V_{0.20}Zr_{0.20}Nb_{0.20}$ at different ball milling times during ArBM synthesis, (right) phase identification analysis for ball-milled material after 15 and 135 minutes.

SEM characterization reveals the presence of a minor secondary phase (*light gray*) on the main phase (*gray*), as noticed by the contrast in the BSE image in Figure 3. Both phases were analyzed by EDS and the results of chemical analysis are listed in Table 1. The main phase has a chemical composition close to nominal with slightly less Zr-content, while the minor phase (impurity) has a chemical composition rich in Zr.

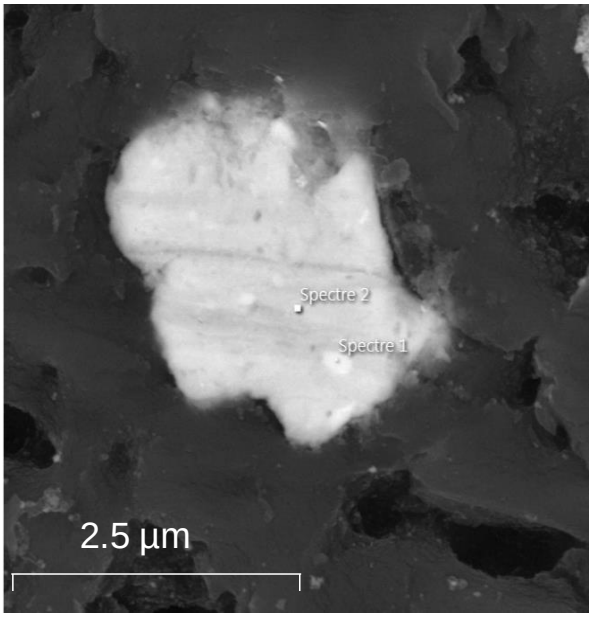

Figure 3. Backscattered electron image (SEM) of the as-prepared $Mg_{0.20}Ti_{0.20}V_{0.20}Zr_{0.20}Nb_{0.20}$ by ArBM.

Table 1. Chemical analyses (EDS) on the two phases observed in the BSE image for the equimolar $Mg_{0.20}Ti_{0.20}V_{0.20}Zr_{0.20}Nb_{0.20}$.

Element at%	Nominal	MPEA	Impurity
Ti	20,0	20,5 (±0.6)	11,1 (±1.0)
V	20,0	19,5 (±0.7)	9,7 (±1.2)
Zr	20,0	17,6 (±1.3)	49,3 (±3.0)
Nb	20,0	20,9 (±0.8)	15,0 (±1.3)
Mg	20,0	21,5 (±0.4)	14,9 (±0.9)

In summary, a significant amount of Zr is segregated into a second phase as characterized by XRD and EDS. These findings suggest there is a maximum uptake of Zr into the structure of the main *bcc* phase (MgTiVZrNb). Additionally, the lattice distortion for the equimolar composition is rather high, δ= 7.3%, which is at the empirical limit for single-phased alloys[1]. Therefore, the Zr-content must be reduced to avoid the formation of secondary phases.

In conclusion, reducing the Zr-content not only will avoid phase segregation, but it will also reduce the lattice distortion since the atomic radii of Zr (r= 1.59 Å) is the second largest in the mixture and significantly bigger than Ti, V, and Nb (r= 1.45, 1.31, and 1.43 Å respectively). Therefore, to optimize the chemical composition in pursuit of a single-phased material, the Zr-content will be halved to 10 at%.

(I.II) Non-equimolar composition

For this approach, diverse Mg-quinary alloys were synthesized by ArBM fixing the Zr concentration to 10 at% while varying the content of the other elements, with particular interest on the fifth element (in this case, Mg). As a first attempt, only the Zr concentration was fixed at 10 at%, while the rest of the elements kept an equiatomic concentration, giving the following composition $Mg_{0.225}Ti_{0.225}V_{0.225}Zr_{0.10}Nb_{0.225}$. This composition, coincidentally, has the same lattice distortion as the equimolar alloy, 7.3%. This is because Mg is the largest atom in the mixture (r= 1.60 Å) with relatively high concentration (~1/4), causing a large disparity due to the size mismatch of the elements. A third Mg-containing alloy was prepared, this time, with reduced Mg-content, $Mg_{0.10}Ti_{0.30}V_{0.25}Zr_{0.10}Nb_{0.25}$. This composition has a lattice distortion of 6.6%. Figure 4 shows the XRD patterns of the different Mg-alloys prepared under the same synthesis conditions.

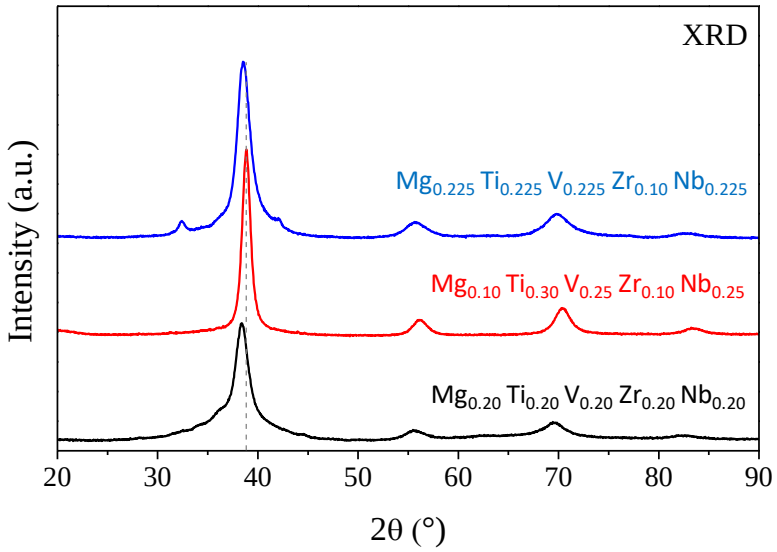

Figure 4. XRD patterns of three different Mg-Ti-V-Zr-Nb compositions synthesized by ArBM.

The alloy with the highest Mg-content (*blue*, $Mg_{0.225}Ti_{0.225}V_{0.225}Zr_{0.10}Nb_{0.225}$) reveals the presence of secondary phases in the XRD pattern, with broad diffraction peaks for the main *bcc* phase. On the other hand, the sample containing only 10 at% of Mg (*red*) crystallized as a single *bcc* phase with narrow peaks. The crystallinity of the latter is far better than the other two compositions, showing narrower and symmetric peaks in the XRD pattern. The composition $Mg_{0.10}Ti_{0.30}V_{0.25}Zr_{0.10}Nb_{0.25}$ has the smallest lattice distortion among the three compositions with a δ= 6.6% (see Table 2). These results are good agreement with the observations made by Yang *et al.*[7] and Ye *et al.*[1], where alloys tend to form single-phase solid solutions at lower δ. Also, the three compositions formed a main *bcc* phase, their VEC values are between 4.0 - 4.3 which is in good agreement with the observations by Couzinié *et al.*[3].

Table 2. Stoichiometry of the quinary HEA Mg-Ti-V-Zr-Nb and their calculated lattice distortion (δ) and valence electron concentration (VEC) [4], [7], as well as brief observations of the XRD patterns after the synthesis of each composition. Legend: r stands for experimental atomic radii of the metallic elements and all values were taken from reference[8].

r=	**Ti** *(1.45 Å)*	**V** *(1.31 Å)*	**Zr** *(1.59 Å)*	**Nb** *(1.43 Å)*	**Mg** *(1.60 Å)*	δ/ %	*VEC*	Observations
	0.20	0.20	0.20	0.20	0.20	7.3	4.0	broad peaks, *bcc* +secondary phases
	0.225	0.225	0.10	0.225	0.225	7.3	4.0	broad peaks, *bcc* +secondary phases
	0.30	0.25	0.10	0.25	0.10	6.6	4.3	narrow peaks, single *bcc*

Therefore, the composition $Mg_{0.10}Ti_{0.30}V_{0.25}Zr_{0.10}Nb_{0.25}$ is the only one forming a single-phased alloy and it also fulfills the criteria established for HEA definition. For that reason, the rest of the MPEAs proposed in this project were synthesized following the same chemical composition $Ti_{0.30}V_{0.25}Zr_{0.10}Nb_{0.25}$ - $M_{0.10}$ (M= Mg, Al, Ta), or an equivalent for the quaternary alloy $Ti_{0.325}V_{0.275}Zr_{0.125}Nb_{0.275}$ (Figure 5).

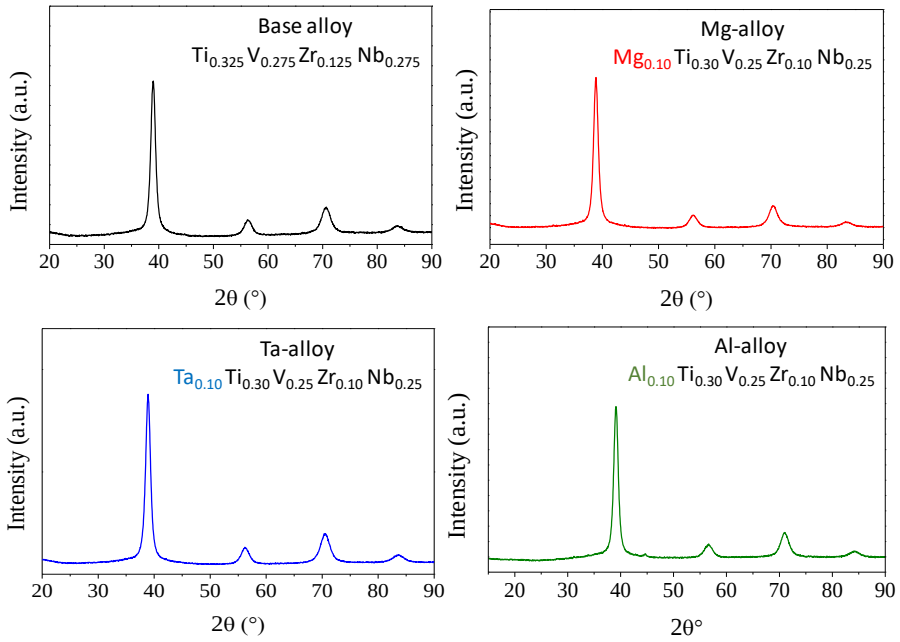

Figure 5. XRD of different MPEAs $Ti_{0.30}V_{0.25}Zr_{0.10}Nb_{0.25}$-$M_{0.10}$ (M= Mg, Al, Ta) prepared by ArBM.

Table 3. Stoichiometry of the proposed HEA and their respective calculated lattice distortion (δ) and valence electron concentration (VEC)[4], [7]. Legend: r stands for experimental atomic radii of the metallic elements and all values were taken from reference[8].

r=	Ti (1.45 Å)	V (1.31 Å)	Zr (1.59 Å)	Nb (1.43 Å)	Mg (1.60 Å)	Al (1.43 Å)	Ta (1.43 Å)	δ/ %	VEC
	0.375	0.275	0.125	0.275				6.0	4.6
	0.30	0.25	0.10	0.25	0.10			6.6	4.3
	0.30	0.25	0.10	0.25		0.10		5.5	4.4
	0.30	0.25	0.10	0.25			0.10	5.5	4.6

All proposed alloys have a lattice distortion below δ= 6.6% and VEC below 4.6, see Table 3, and all of them crystallized in single *bcc* phase solid solutions. The optimal ball milling time for synthesis was 60 minutes for all compositions, except for the Mg-containing alloy, which was 120 min. With these results, the experiments of chemical optimization are concluded. The next section will evaluate the hydrogenation properties of the quaternary alloy with the optimized composition prepared by the three synthesis methods described in Chapter 2.

(II) Analysis of three different syntheses methods.

This segment presents the characterization of the **quaternary alloy** prepared by ArBM, HT-AM, and RBM, with optimized composition $Ti_{0.325}V_{0.275}Zr_{0.125}Nb_{0.275}$ with δ= 6.0%, and discusses the main differences in their hydrogen sorption properties and the relationship with their microstructure. The objective of this study was to determine the most suitable synthesis approach among the three methods available at the ICMPE: ArBM, HT-AM and RBM.

The comparison of results will be based on the maximum hydrogen capacity (H/*M*), temperature for hydrogen desorption (T_{onset}), hydrogenation cycling performances, and an assessment of the crystalline structure before and after hydrogenation. Analyzing these differences will also provide insightful information about the relationship between the hydrogenation performances and their microstructure. The results of this comparative study were published in the journal *Molecules* in 2019[9].

> Author's comment: the discussion of results in this section focuses mainly on the performances for each synthetic method, rather than a full description and analysis of individual results. Detailed discussions for each analysis are fully disclosed in the upcoming and dedicated Chapters.

(II.I) Synthesis of $Ti_{0.325}V_{0.275}Zr_{0.125}Nb_{0.275}$: ArBM and HT-AM

The quaternary alloy with optimized composition was successfully prepared by ArBM in a single phase as described earlier in this chapter. For HT-AM, similar to ArBM, the alloy was characterized by XRD during synthesis after every five melts until a single phase was obtained. In this case, 20 re-melts were necessary to produce a single phase. Both methods have produced a *bcc* alloy (*Im-3m* space group) with very similar lattice parameters: (ArBM) a_{bcc}= 3.270(1) Å, and (HT-AM) a_{bcc}= 3.261 (1) Å, as determined by the Rietveld refinement of the XRD patterns in Figure 6.

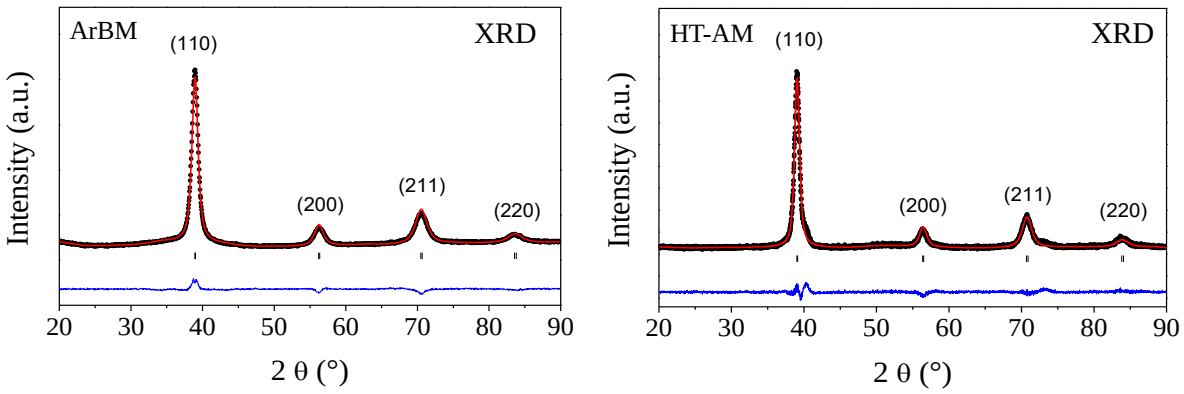

Figure 6. XRD and corresponding Rietveld refinements of $Ti_{0.325}V_{0.275}Zr_{0.125}Nb_{0.275}$ with a bcc structure (Im-3m) for the alloys prepared by ArBM (left) and HT-AM (right). The observed data (experimental) is represented in black dots and the red line corresponds to the calculated data; the difference between the observed and calculated profiles is represented in blue.

(II.II) Synthesis of the hydride $Ti_{0.325}V_{0.275}Zr_{0.125}Nb_{0.275}$-$H_x$ by RBM

In RBM, the alloying and the hydrogenation processes occur simultaneously during ball milling, resulting in the direct synthesis of a hydride phase: $\mathbf{Ti_{0.325}V_{0.275}Zr_{0.125}Nb_{0.275}H_x}$. Sensors within the milling jar allow the quantification of the total hydrogen absorption by the pressure change before and after synthesis. A kinetics plot of absorption can be obtained by continuously recording the temperature and pressure during synthesis and using the mathematical model proposed by Zhang *et al.*[10] (Figure 7 *left*). The maximum hydrogen capacity was determined to be 1.8 H/*M* (2.6 wt.%) and a single hydride phase, $Ti_{0.325}V_{0.275}Zr_{0.125}Nb_{0.275}H_{1.8}$, was obtained after 60 minutes of RBM, as confirmed by XRD (Figure 7 *left*).

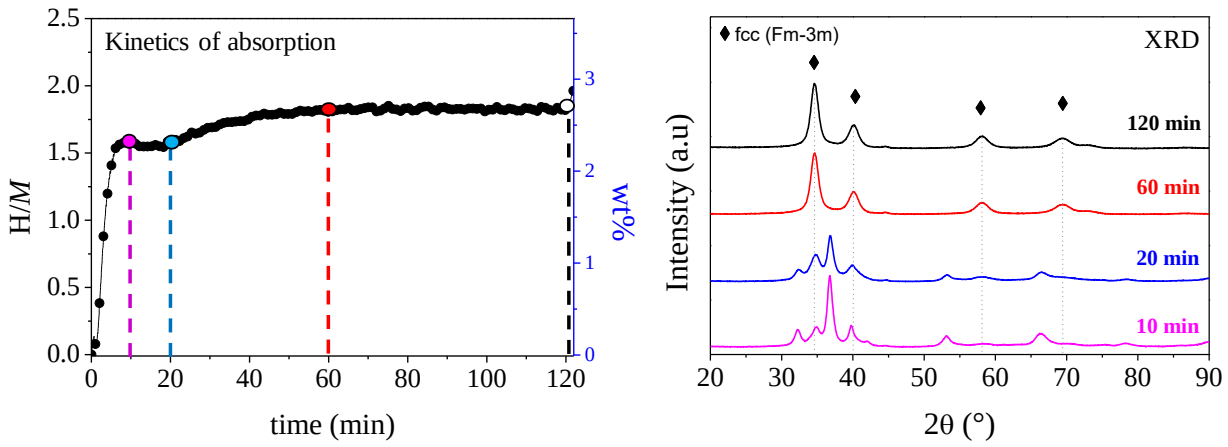

Figure 7. Kinetics of absorption (left) and XRD patterns at different ball milling times during RBM synthesis of the alloy $Ti_{0.325}V_{0.275}Zr_{0.125}Nb_{0.275}H_x$ (right).

It is worth to further analyze and discuss the profile of kinetics curve in RBM synthesis, particularly in the synthesis of MPEAs. Initially, within the first minutes of ball milling, the kinetic curve shows a fast hydrogen absorption followed by a saddle point around 1.5 H/*M*. Then, the capacity slowly increases up to a maximum of 1.8 H/*M* where it remains constant after 60 minutes of ball milling. To understand the mechanism of the alloying process, XRD analysis was performed at different periods during RBM synthesis, t= 10, 20, 60, and 120 minutes, and the diffraction patterns of these are plotted in Figure 7 *right,* revealing the phase evolution with RBM time.

Most of the diffraction peaks at 10 minutes of ball milling (*magenta*) were identified as the elemental hydrides from the alloy composition (TiH_2, VH, ZrH_2, and NbH). This explains the rapid hydrogen absorption seen in the first minutes in the kinetic curve. At 20 minutes (*blue*), a new phase has become more apparent and it grew larger at the expense of the others signals. This new phase, marked with black diamonds (◊), corresponds to the hydride phase of the MPEA. Only after 60 minutes of RBM (*red*), a single-phased hydride was achieved with the maximum hydrogen capacity (1.8 H/*M*). Further ball milling time did not improve the hydrogen capacity and the crystalline structure suffered no change after 120 minutes of ball milling (*black*).

In conclusion, a direct hydride of $Ti_{0.325}V_{0.275}Zr_{0.125}Nb_{0.275}H_x$ was successfully synthesized in single phase by the RBM method, reaching a maximum hydrogen capacity of 1.8 H/*M*. The produced hydride was pyrophoric and therefore, all RBM samples were always manipulated and kept in a high-purity Ar glovebox.

Additional remarks

These findings provide insightful information about the reaction mechanism in the formation of (MPEAs and HEAs) hydrides by RBM. First, only two reactions will take place during RBM synthesis: a solid-gas (S-G) reaction leading to the formation of hydrides, and a solid-solid (S-S) reaction which fuses the metals in the solid-state.

In the first minutes of ball milling, only the S-G reaction takes place resulting in the formation of the elemental hydrides, as determined by the phase analysis in the XRD pattern. At this point, the energy transferred by HEBM is kinetically dissipated through fracture and reduction of the particle size. Once the material is finely powdered to μm scale, the S-S reaction will take place between the elemental hydrides in the mixture, until the alloying is complete. Between 10-25 minutes of ball milling, the hydrogen capacity has an irregular behavior where the capacity drops into a saddle before increasing steadily up to a maximum. This means that both reactions occur simultaneously in an intrinsic and complex mechanism. Nevertheless, once the material is completely alloyed, the S-G reaction will stop when equilibrium is reached.

(II.III) Hydrogenation of the *bcc* alloys: ArBM and HT-AM

The *bcc* alloys described in (II.I) were subsequently hydrogenated by performing PCI measurements on the samples at constant temperature (see Figure 8). Prior to these measurements, the alloys have been exposed to air during sample manipulation.

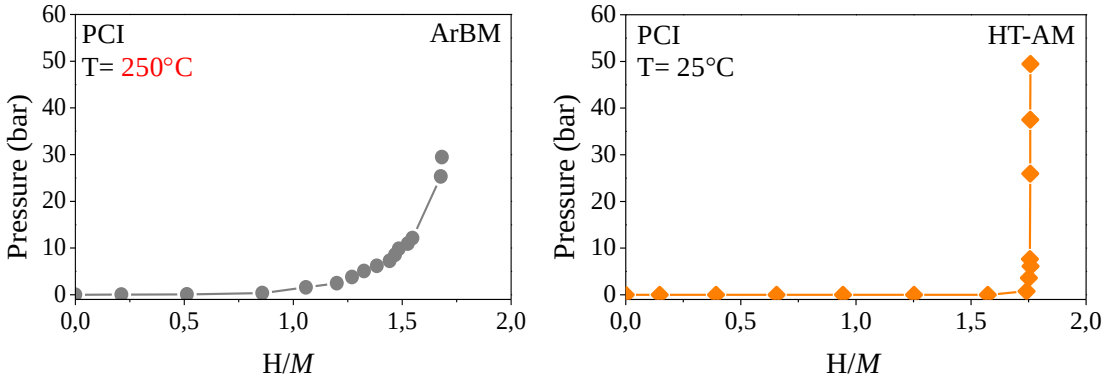

Figure 8. Pressure-composition isotherms of the $Ti_{0.325}V_{0.275}Zr_{0.125}Nb_{0.275}$ samples synthesized by ArBM (left) and HT-AM (right).

In both methods, the PCI curve shows a single-plateau region with an equilibrium pressure below the limits of detection of the Sievert's instrument, in the range of 10^{-2} bar. The maximum absorption capacities for each sample are 1.7 H/*M* (ArBM), 1.8 H/*M* (HT-AM), and 1.8 H/*M* (RBM). The only remarkable difference between ArBM and HT-AM samples is the poor kinetics of absorption displayed by the ArBM sample at room temperature conditions, and because of this, the PCI was recorded at 250 °C.

The HT-AM sample showed good absorption kinetics at 25 °C while the ArBM showed the poorest performance. The poor kinetics in the ArBM sample can be explained by oxidation on the sample's surface. As a fine powder, the ArBM sample has a high surface-to-volume ratio and the oxide layer at the surface hinders the hydrogen absorption into the alloy. Therefore, higher temperatures were necessary to crack the oxide layer exposing a reactive surface to hydrogen. This effect was not observed for the HT-AM sample probably due to its larger particle size (low surface-to-volume ratio).

The resulting hydrides from each method were then characterized by XRD and the structural properties determined by Rietveld analysis, shown in Figure 9. All hydrides have crystallized in *fcc* structures (Fm-3m)[1] with lattice parameters a_{fcc}= 4.548(1) Å (ArBM), a_{fcc}= 4.493(1) Å (HT-AM), and a_{fcc}= 4.474(1) Å (RBM).

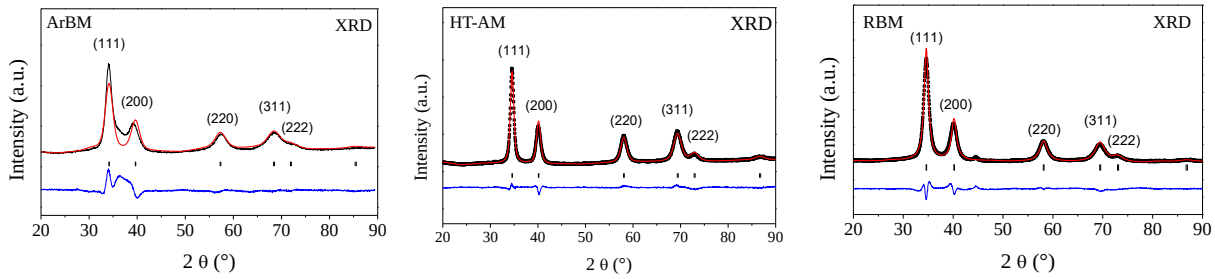

Figure 9. XRD and corresponding Rietveld analysis of the hydride $Ti_{0.325}V_{0.275}Zr_{0.125}Nb_{0.275}H_x$ with fcc structure (Fm-3m) for each preparation method: ArBM (left, χ^2= 40.9), HT-AM (middle, χ^2= 6.10), and RBM (right, χ^2= 11.1). The observed data (experimental) is represented in black dots and the red line corresponds to the calculated data; the difference between the observed and calculated profiles is represented in blue.

[1] Notice that the hydride in this manuscript is described as an *fcc* structure, whereas in the published article[9], the hydride phase is described with a *bct* structure. This is because the lattice refinement can be similarly described by both structures and it was later agreed that a *fcc* is the simplest lattice for the hydride phase. More will be discussed in the following chapters.

The fitting of the refinement for the HTAM and RBM samples are good enough for a single *fcc* structure (χ^2= 6.10 and 11.1 respectively), however, this factor is significantly higher for the ArBM sample (χ^2= 40.9). The difference between the observed diffraction data and the calculated profile for the ArBM sample suggests the presence of a secondary phase. This may be explained by the incomplete hydrogenation in ArBM (1.7 H/*M*) as compared to its HT-AM and RBM counterparts (1.8 H/*M*), where a portion of the material remains as a solid solution with hydrogen in *bcc* structure. The diffraction peak (110) in the *bcc* solid solution rises at around 35-40° 2θ, depending on its hydrogen content, which is in between the diffraction peaks (111) and (200) of the *fcc* structure, just as seen in the XRD pattern of the ArBM sample.

In summary, the ArBM material had the lowest hydrogen capacity and the poorest crystallinity among the three methods, most probably due to surface oxidation issues.

(II.IV) Hydrogen desorption of the hydrides: ArBM, HT-AM, and RBM

The corresponding hydrides were subsequently characterized by thermo-desorption spectroscopy (TDS) where the samples are heated at a constant temperature rate (2.5 °C/min) while under dynamic secondary vacuum (10^{-6} mbar). The partial pressure of the gas desorbed (H_2) is then recorded as a function of the temperature, revealing a characteristic desorption profile. Figure 10 shows the normalized TDS curves measured from each method. The onset temperature of desorption (T_{onset}) and temperature of maximum desorption rate (T_{max}) for each synthetic method are: ~280 and 340 °C for ArBM (grey), ~220 and 250 °C for HT-AM (orange), and ~180 and 210 °C for RBM (green), respectively.

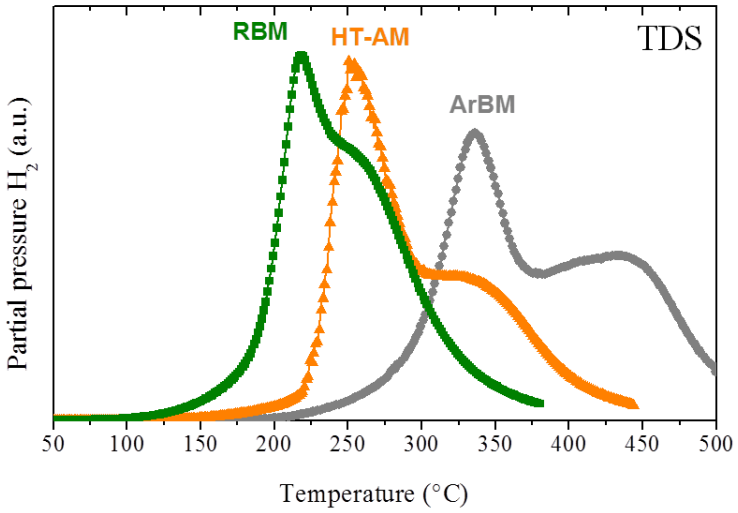

Figure 10. Normalized TDS curves of the hydrides $Ti_{0.325}$ $V_{0.275}$ $Zr_{0.125}$ $Nb_{0.275}H_x$ from each synthetic method (RBM, HT-AM and ArBM) at a constant heating rate (2.5 °C/min).

The three alloys display similar desorption profiles with a main desorption peak followed by a second desorption event after 30-60 °C. The lowest temperatures of desorption were observed for the RBM sample followed by HT-AM, and lastly, ArBM.

These differences can also be accredited to a degree of surface oxidation in each sample, and ArBM being the most affected by oxidation. The resulting hydride of the HT-AM sample is in the form of coarse powder, still a larger particle size than a ball-milled sample, and thus the material is less affected by surface oxidation. And finally, the RBM sample has the lowest degree of surface oxidation as it was manipulated and stored under Ar atmosphere without air exposure.

After hydrogen desorption, the crystalline structure of the "desorbed" phase was characterized by XRD and Rietveld refinement (Figure 11). All alloys have adopted the *bcc* structure with similar lattice parameters for each method: (ArBM) a_{bcc}= 3.268(1) Å, (HT-AM) a_{bcc}= 3.253 (1) Å, and (RBM) a_{bcc}= 3.277 (1) Å.

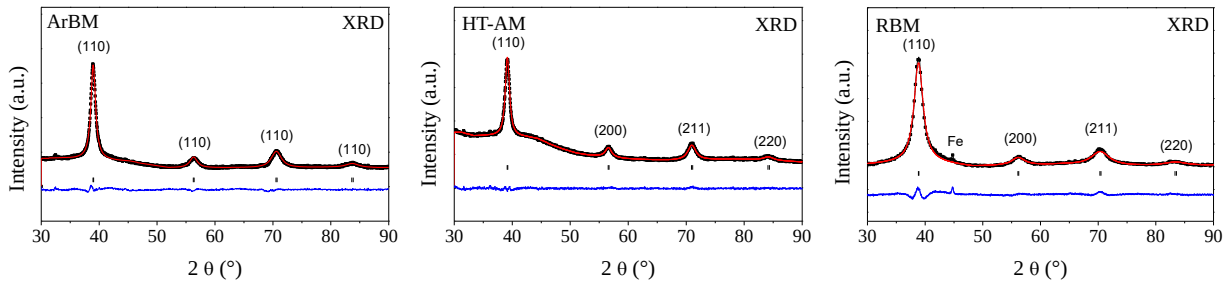

Figure 11. XRD and corresponding Rietveld analysis on the desorbed $Ti_{0.325}V_{0.275}Zr_{0.125}Nb_{0.275}$ with bcc structure (Im-3m) for the three synthetic methods: ArBM (left), HT-AM (middle), and RBM (right). The observed data (experimental) is represented in black dots and the red line corresponds to the calculated data; the difference between the observed and calculated profiles is represented in blue.

In all cases, the alloys have recovered the initial *bcc* structure after desorption with similar lattice parameters to those prepared initially by ArBM and HT-AM (section II.I). This proves the full reversibility of the material upon hydrogen absorption and desorption, and no phase decomposition was noticed from the XRD and Rietveld analyses.

Similarly to the previous conclusion, the ArBM sample had the poorest desorption performance among the three materials. Again, this trend can be explained by the effect of surface oxidation in the samples, and this effect increases with the reduction of the particle size.

(II.V) Hydrogen absorption/desorption cycling

The reversible storage capacity was evaluated in terms of hydrogen capacity (H/*M* and wt.%) by submitting the alloys to several hydrogen absorption and desorption cycles at room temperature. For this evaluation, only the RBM and HTAM samples were investigated since they showed better performances than ArBM. The hydrogenation of the alloy was carried out by exposing the sample to at least 25 bar of H_2 equilibrium pressure at 25 °C. For hydrogen desorption, the sample was heated up to 400 °C for 240 minutes under dynamic vacuum. The results of the hydrogen-cycling evaluation are plotted in Figure 12.

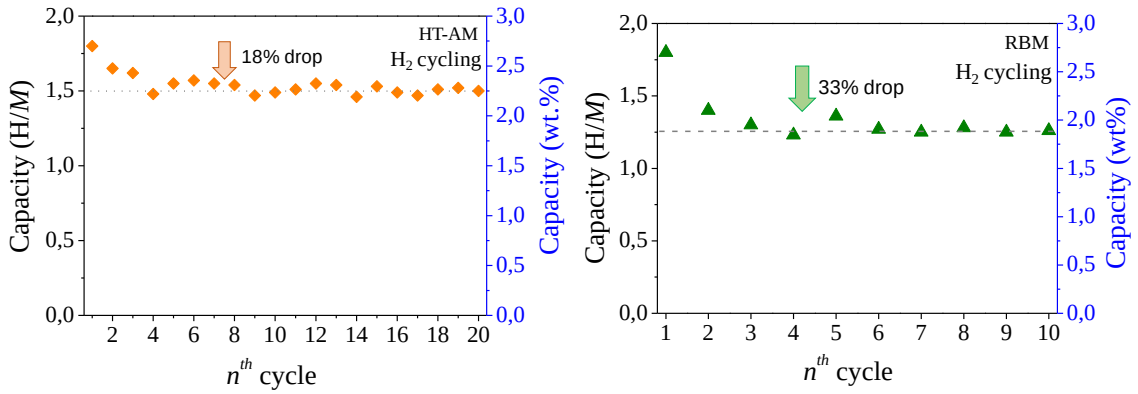

Figure 12. Hydrogen cycling evaluation of the MPEA $Ti_{0.325}V_{0.275}Zr_{0.125}Nb_{0.275}$ prepared by HT-AM (left) and RBM (right).

The cycling tests reveal a fade of the maximum hydrogen capacity for the first 4 cycles followed by a stabilization of the capacity around 1.25 H/*M* and 1.50 H/*M*, for RBM and HT-AM, respectively. The stabile storage capacity is indicated by the dashed line in Figure 12. Both alloys have demonstrated to withstand hydrogen-cycling and recover approximately 67% (RBM) and 82% (HT-AM) of their initial capacity.

The HT-AM showed a superior cycling performance than the RBM sample, and this may be a consequence of the material microstructure. It is well known that hydrogen absorption/desorption causes irreversible damage to the structure of the alloy due to the expansion and contraction of the lattice. RBM samples are more susceptible to this effect due to the many defects and strain in their microstructure consequence of the extensive grinding in ball milling.

(II.VI) Summary and conclusions

The alloy with composition $Ti_{0.325}V_{0.275}Zr_{0.125}Nb_{0.275}$ was successfully synthesized by three different methods and its hydrogen absorption and desorption properties were evaluated in terms of maximum hydrogen capacity, reversible storage capacity, kinetics of absorption, temperature of desorption, and temperature at maximum desorption rate; these results are listed in Table 2. The results from the structural refinement and the lattice constants of the pristine, the hydride, and the desorbed phase, are listed in Table 3.

Table 2. Hydrogen absorption/desorption properties of $Ti_{0.325}V_{0.275}Zr_{0.125}Nb_{0.275}$ prepared by three different methods: ArBM, HT-AM, and RBM.

	Hydrogen absorption			Hydrogen desorption		Cycling
Synthesis method	H/*M* (wt.%)	P_{eq}	kinetics	T_{onset}	T_{max}	Reversible capacity
ArBM	1,7 (2,5)	$<10^{-2}$ bar	slow	280 °C	340 °C	N/A
HT-AM	1,8 (2,6)	$<10^{-2}$ bar	fast	220 °C	250 °C	82%
RBM	1,8 (2,6)	$<10^{-2}$ bar	fast	180 °C	210 °C	67%

Table 3. Lattice parameters of $Ti_{0.325}V_{0.275}Zr_{0.125}Nb_{0.275}$ prepared by three different methods: ArBM, HT-AM, and RBM, in their pristine, hydride, and desorbed phase respectively.

	Pristine a_{bcc}	Hydride a_{fcc}	Desorbed a_{bcc}
ArBM	3.270(1) Å	4.548(1) Å	3.268(1) Å
HT-AM	3.261 (1) Å	4.497(1) Å	3.253 (1) Å
RBM	-	4.474(1) Å	3.277 (1) Å

Overall, the three synthetic methods have produced the same alloy with similar hydrogen sorption properties. The HT-AM method has demonstrated great results in all evaluations and particularly on the hydrogen-cycling test, showing the highest reversible storage capacity. Additionally, the HT-AM sample was able to perform well even after being exposed to O_2.

In conclusion, the HT-AM method will be the privileged choice for the preparation of MPEAs in this manuscript, when applicable. In case the alloy cannot be prepared by HT-AM, ArBM will be implemented instead and the samples will be stored and manipulated under Ar to avoid surface oxidation and deterioration of their hydrogenation properties. Additionally, an activation treatment will be implemented for all samples prior to the first hydrogenation to improve the kinetics of absorption during the evaluation of their properties.

Bibliography

[1] Y. F. Ye, Q. Wang, J. Lu, C. T. Liu, and Y. Yang, "High-entropy alloy: challenges and prospects," *Materials Today*, vol. 19, no. 6, pp. 349–362, Jul. 2016, doi: 10.1016/j.mattod.2015.11.026.

[2] D. B. Miracle and O. N. Senkov, "A critical review of high entropy alloys and related concepts," *Acta Materialia*, vol. 122, pp. 448–511, Jan. 2017, doi: 10.1016/j.actamat.2016.08.081.

[3] J.-P. Couzinié and G. Dirras, "Body-centered cubic high-entropy alloys: From processing to underlying deformation mechanisms," *Materials Characterization*, vol. 147, pp. 533–544, Jan. 2019, doi: 10.1016/j.matchar.2018.07.015.

[4] S. Guo, C. Ng, J. Lu, and C. T. Liu, "Effect of valence electron concentration on stability of fcc or bcc phase in high entropy alloys," *J. Appl. Phys.*, p. 6, 2011.

[5] J. Huot, D. B. Ravnsbæk, J. Zhang, F. Cuevas, M. Latroche, and T. R. Jensen, "Mechanochemical synthesis of hydrogen storage materials," *Progress in Materials Science*, vol. 58, no. 1, pp. 30–75, Jan. 2013, doi: 10.1016/j.pmatsci.2012.07.001.

[6] A. Zeaiter, D. Chapelle, F. Cuevas, A. Maynadier, and M. Latroche, "Milling effect on the microstructural and hydrogenation properties of TiFe0.9Mn0.1 alloy," *Powder Technology*, vol. 339, pp. 903–910, Nov. 2018, doi: 10.1016/j.powtec.2018.08.085.

[7] X. Yang and Y. Zhang, "Prediction of high-entropy stabilized solid-solution in multi-component alloys," *Materials Chemistry and Physics*, vol. 132, no. 2–3, pp. 233–238, Feb. 2012, doi: 10.1016/j.matchemphys.2011.11.021.

[8] Gordon Aylward and Tristan Findlay, "SI Chemical Data, 3rd edition," *J. Chem. Educ.*, vol. 72, no. 5, p. A109, May 1995, doi: 10.1021/ed072pA109.1.

[9] J. Montero, C. Zlotea, G. Ek, J.-C. Crivello, L. Laversenne, and M. Sahlberg, "TiVZrNb Multi-Principal-Element Alloy: Synthesis Optimization, Structural, and Hydrogen Sorption Properties," *Molecules*, vol. 24, no. 15, p. 2799, Jul. 2019, doi: 10.3390/molecules24152799.

[10] J. Zhang *et al.*, "Highlighting of a Single Reaction Path during Reactive Ball Milling of Mg and TM by Quantitative H_2 Gas Sorption Analysis To Form Ternary Complex Hydrides (TM = Fe, Co, Ni)," *J. Phys. Chem. C*, vol. 115, no. 11, pp. 4971–4979, Mar. 2011, doi: 10.1021/jp2005293.

CHAPTER III

~ Ti-V-Zr-Nb ~

CHAPTER 3: Base alloy, Ti-V-Zr-Nb

The quaternary alloy Ti-V-Zr-Nb is the first of the series of MPEAs studied in this project and it will serve as the reference alloy with base properties to evaluate the effect of an extra element into the composition. The results of synthesis and characterization will be discussed in this chapter for the optimized composition $Ti_{0.325}\,V_{0.275}\,Zr_{0.125}\,Nb_{0.275}$, which has a calculated lattice distortion, δ, of 6.0%[1], [2]. The quaternary alloy will be sometimes referred to as ***the base alloy*** in this manuscript for simplicity.

3.1 Synthesis of Ti-V-Zr-Nb

The quaternary alloy was prepared by HT-AM, mixing the elements and melting altogether under a constant electric arc for 1 minute, and re-melted 20 times until the alloy had adopted a single phase. The structural characterization of the as-cast alloy was carried out by powder X-ray diffraction (XRD) and the structural parameters were determined from the Rietveld refinement analysis of the diffraction pattern (Figure 3.1).

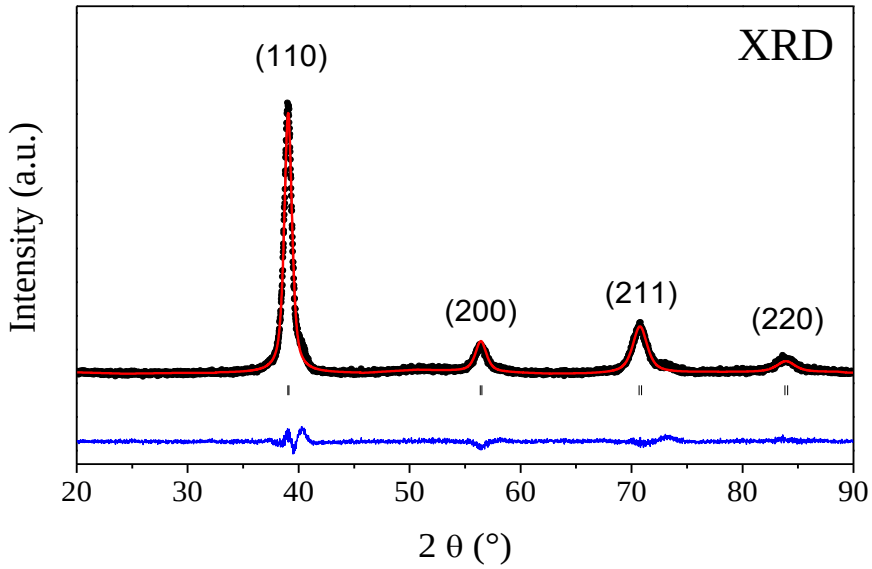

Figure 3.1. XRD of $Ti_{0.325}V_{0.275}Zr_{0.125}Nb_{0.275}$ and corresponding Rietveld refinement with bcc structure (Im-3m) and lattice parameter a_{bcc}= 3.261(1) Å. The observed data (experimental) is represented in black dots and the red line corresponds to the calculated data; the difference between the observed and calculated profiles is represented in blue.

The as-cast alloy crystallized in a *bcc* structure (*Im-3m* space group) with lattice parameter a_{bcc}= 3.261(1) Å, as determined by the Rietveld analysis. It has been reported elsewhere[3], the synthesis of a single-phased TiVZrNb in equimolar composition with a *bcc* lattice parameter slightly larger than the reported here, a_{bcc}= 3.308(1) Å. This is normal as Zr is the largest atom in the composition and therefore, increasing its concentration will cause an expansion of the lattice constant.

3.2 Hydrogenation of Ti-V-Zr-Nb

After synthesis, the as-cast alloy was cut into smaller pieces for the hydrogen absorption characterization. Prior to hydrogenation, the alloy was submitted to an activation treatment to promote the kinetics of the reaction and avoid long incubation times after exposing the alloy to hydrogen. This allowed the material to rapidly absorb hydrogen even at low H_2 pressures at 25 °C. The activation treatment was carried out by heating the sample up to 340 °C for 2 hours under dynamic vacuum.

Once the sample was activated, a pressure-composition isotherm (PCI) was recorded at 25 °C for the quaternary alloy (Figure 3.2). The PCI curve reveals a single-plateau region at low equilibrium pressure and a maximum hydrogen storage capacity of 1.8 H/*M* (2.7 wt.%). The equilibrium pressure for hydride formation is below the limits of detection of the Sievert's instrument (10^{-2} bar) and therefore, the precise value of equilibrium pressure was not measured.

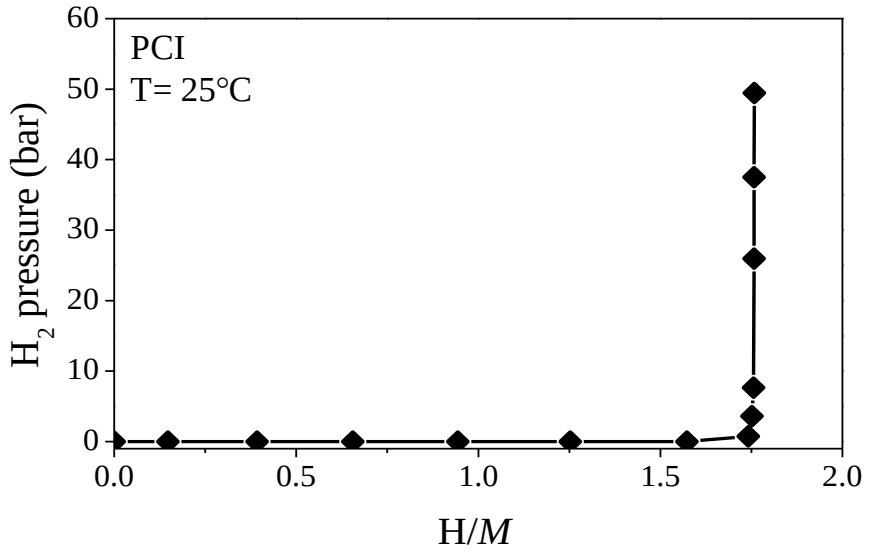

Figure 3.2. Pressure-composition isotherm of $Ti_{0.325}V_{0.275}Zr_{0.125}Nb_{0.275}$ measured at 25 °C.

The appearance of a plateau pressure in the PCI curve is an indication of a phase transformation upon hydrogen absorption, from a (disordered) hydrogen-metal solid solution to an (ordered) hydride phase. The PCI curve above suggests a single-phase transformation from the pristine *bcc* alloy (0.0 H/*M*) to a full-hydride phase (1.8 H/*M*), similar to TiVZrNbHf HEA reported elsewhere, [4], [5]. This behavior is unlike most conventional *bcc* alloys, where the alloys often have two plateau regions, one at low equilibrium pressures reaching 1 H/*M*, or partial capacity, and a second plateau at higher equilibrium pressures reaching higher capacities[6], [7].

The crystalline structure of the resulting hydride (1.8 H/*M*) was then characterized by laboratory XRD. The diffraction pattern of the hydride phase can be similarly fitted by the Rietveld method using either a *fcc* (Fm-3m) or *bct* (I4/mmm) structures, see Figure 3.3.

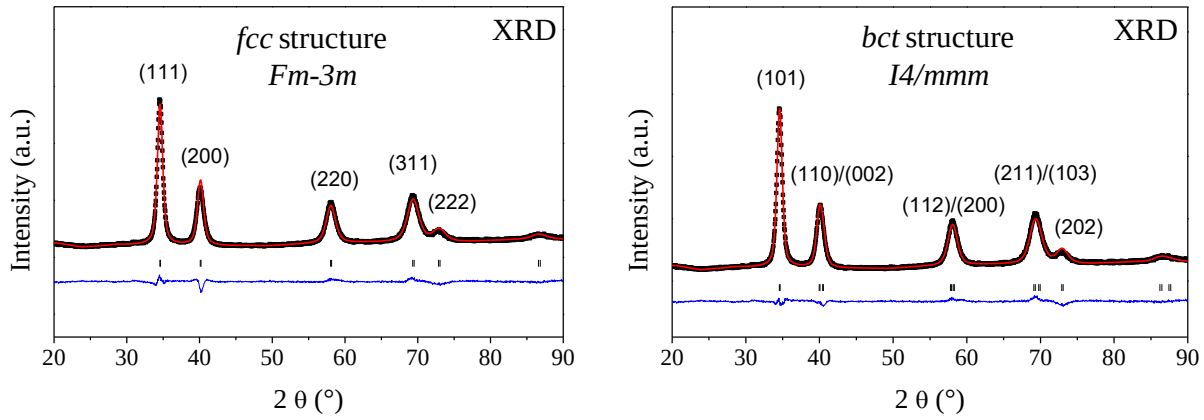

Figure 3.3. XRD of the hydride $Ti_{0.325}V_{0.275}Zr_{0.125}Nb_{0.275}H_{1.8}$ and corresponding Rietveld analysis fitting for a fcc (left) and bct (right) structures. The observed data (experimental) is represented in black dots and the red line corresponds to the calculated data; the difference between the observed and calculated profiles is represented in blue.

The confidence factors of the refinements, χ^2 and R_B, have very similar values for both structures and the real structure cannot be simply determined from these (χ^2= 3.86 and R_B= 2.51 for the *fcc*, and; χ^2= 3.27 and R_B= 3.11 for the *bct*). The lattice constants calculated for each structure are as follow: a_{fcc}= 4.493(1) Å, and a_{bct}= 3.188(1) Å and c_{bct}= 4.459(1) Å.

The fact that the hydride phase can be similarly described by these structures is due to a breakage in the symmetry of the cubic unit cell, where a distortion of the *c*-axis in the *fcc* structure leads to the formation of a tetragonal phase body-centered (*bct*), as illustrated in Figure 3.4[5].

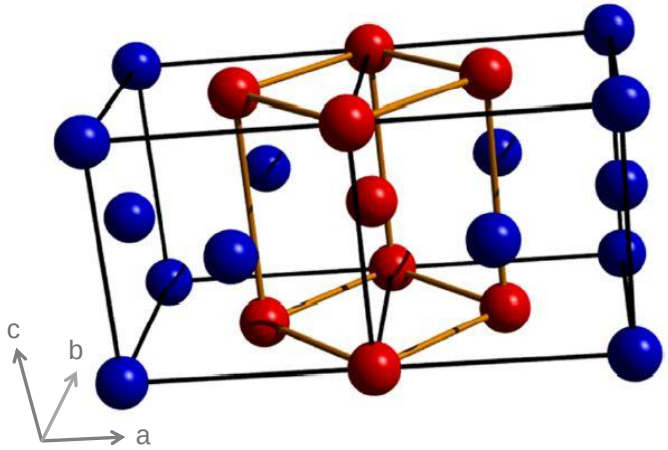

Figure 3.4. Symmetry break along the c-axis of the cubic structure and the formation of a tetragonal structure. The fcc structure is defined by the black edges and the bct structure by the orange lines[5].

In further attempt to discriminate between the *fcc* and *bct* structure, the hydride phase was then characterized by synchrotron radiation XRD (SR-XRD) at the CRISTAL beamline in SOLEIL, France. The results of SR-XRD and the corresponding Rietveld analysis for the *fcc* structure is shown in Figure 3.5. The radiation wavelength used was λ= 0.7289 Å.

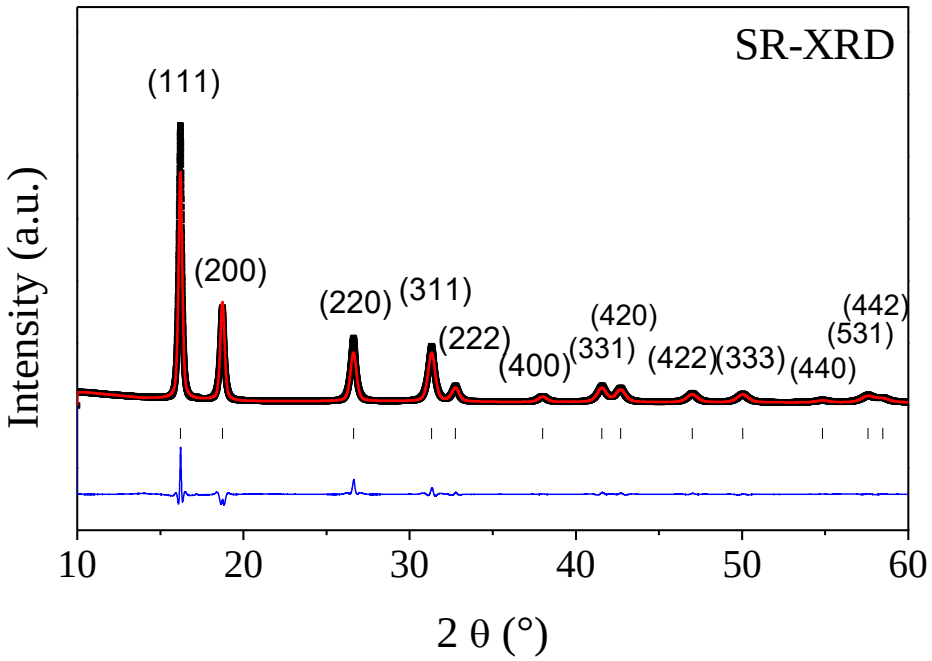

Figure 3.5. SR-XRD of the $Ti_{0.325}V_{0.275}Zr_{0.125}Nb_{0.275}H_{1.8}$ hydride and corresponding Rietveld analysis with a fcc structure (Fm-3m) and lattice parameter a_{fcc}= 4.478(1) Å. The observed data (experimental) is represented in black dots and the red line corresponds to the calculated data; the difference between the observed and calculated profiles is represented in blue.

The diffraction peaks in SR-XRD can be indexed in both *fcc* (a_{fcc}= 4.478(1) Å) and *bct* (not shown - a_{bct}= 3.172(1) Å and C_{bct}= 4.464(1) Å) structures. Similar to the results from laboratory XRD, however, only the refinement of the *fcc* structure is presented in the figure above. Since both structural refinements yield similar confidence factors, we propose as a working hypothesis: the hydride phase of $Ti_{0.325}V_{0.275}Zr_{0.125}Nb_{0.275}$ adopts the simplest lattice which is the *fcc* structure.

In summary, the quaternary alloy has a maximum hydrogen capacity of 1.8 H/*M* (2.7 wt.%) with and equilibrium pressure for hydride formation below 10^{-2} bar at 25 °C. The PCI curve suggests that the hydride formation occurs in a single-step from a pristine *bcc* alloy (a_{bcc}= 3.261(1) Å) to a hydride phase with *fcc* structure (a_{fcc}= 4.478(1) Å), as determined by SR-XRD.

3.3 *In-situ* neutron diffraction

As mentioned in Chapter 2, neutron diffraction (nD) is a complementary structural characterization technique due to its interaction with lightweight elements, such as hydrogen and deuterium. This allows locating the position of deuterium atoms within the unit cell. Additionally, *in-situ* nD was employed to study the phase transformation of the alloy upon hydrogen desorption. The nD experiments were carried out at the ILL neutron facilities in Grenoble, France. Figure 3.6 shows the *ex-situ* neutron diffraction of the hydride (deuteride) sample measured in a vanadium can and its corresponding Rietveld refinement with a *fcc* structure.

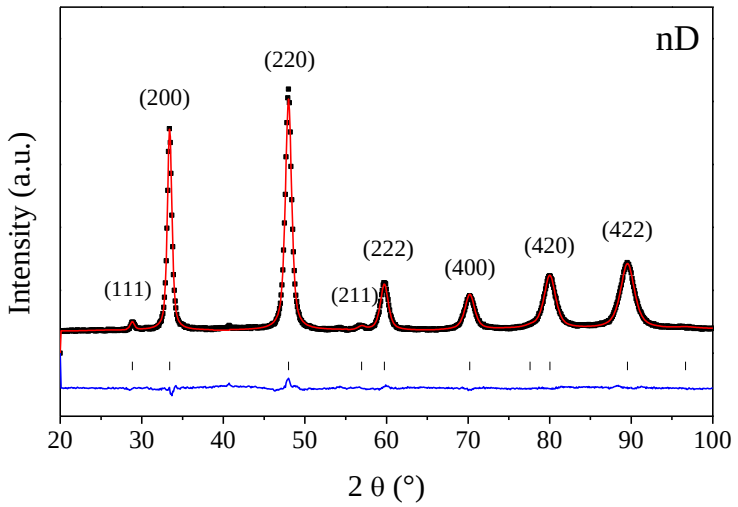

Figure 3.6. Ex-situ nD of the $Ti_{0.325}V_{0.275}Zr_{0.125}Nb_{0.275}D_{1.8}$ and corresponding Rietveld analysis with a fcc structure (Fm-3m) and lattice parameter a_{fcc}= 4.475(1) Å. The observed data (experimental) is represented in black dots and the red line corresponds to the calculated data; the difference between the observed and calculated profiles is represented in blue.

The Rietveld analysis confirms the formation of a single-phased hydride with *fcc* structure and a lattice parameter of a_{fcc}= 4.475(1) Å, in good agreement with the results from SR-XRD. The position of deuterium (or hydrogen) atoms were determined to occupy the tetrahedral interstitial sites of the *fcc* structure (see Figure 3.7).

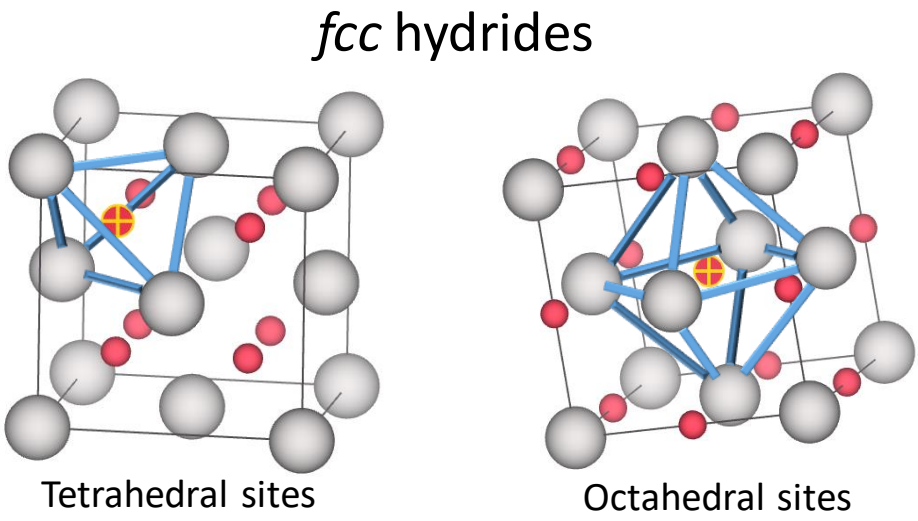

Figure 3.7. Available sites for hydrogen localization in fcc hydrides[8]. The metal atoms represented by the grey spheres are indistinguishable from each other in HEAs, and the interstitial hydrogen atoms are represented by the red spheres in the tetrahedral and octahedral sites.

Next, *in-situ* neutron diffraction experiments were performed on the deuteride phase to study the phase transformation upon (D_2) desorption. The experiment consisted of loading the sample into a silica tube and heating it at a constant temperature rate of 1 °C/min up to ~430 °C, while evacuating under dynamic vacuum (10^{-5} mbar). The neutron thermo-diffractogram in Figure 3.8 shows the diffraction signals of the sample as a function of temperature and a color scale indicating the relative intensities of the diffraction peaks over 2θ angle. The pressure of the turbopump, during vacuuming, was continuously recorded during heating and the pressure readings are plotted next to the thermo-diffractogram as a function of temperature revealing a desorption profile.

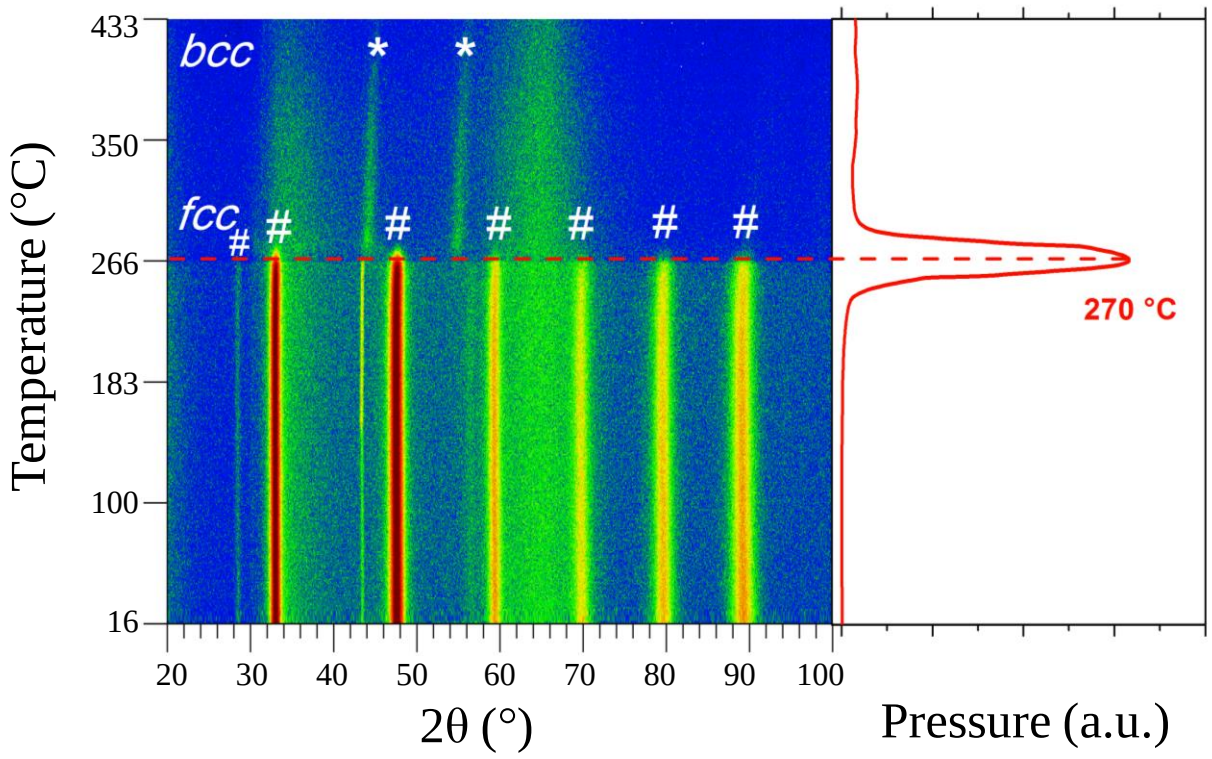

Figure 3.8. In-situ neutron diffraction of $Ti_{0.325}V_{0.275}Zr_{0.125}Nb_{0.275}D_{1.8}$ heated at a constant temperature rate of 1 °C/min and the pressure readings during deuterium desorption.

At room temperature, the diffraction peaks of the hydride phase are marked with the hash symbol (#), while the broad signals observed at 32-36° and 60-70° belong to the silica tube used as the sample holder. The hydride phase remains stable with increasing temperature, from room temperature up to ~270 °C, where the diffraction signals vanish instantly, and a new phase appears. This phase transition is in good agreement with the unique event observed in the pressure profile on the right, thus relating the phase transformation of the alloy with hydrogen desorption at around 270 °C. The new diffraction peaks, marked with the star symbol (*), correspond the *bcc* structure of the alloy. The diffraction peaks of the desorbed phase are very weak due to the low thermal neutron cross-section of the elements involved (Ti, V, Zr, and Nb)[9]. After 270 °C, the *bcc* peaks shift towards a higher 2θ angle with increasing temperature and this is due to hydrogen being released from the *bcc* solid solution, shrinking the lattice in consequence.

From the nD experiment, it is clear that only a one phase transformation takes place for the quaternary alloy during hydrogen desorption, and it can be assumed the quaternary alloy has a single-phase transformation upon hydrogen absorption too. This confirms the hydrogenation

profile seen in the PCI curve with a single plateau region. Moreover, the hydrogen atoms are localized in the tetrahedral sites of the *fcc* structure

3.4 *Thermo-desorption characterization*

The hydrogen desorption properties of the quaternary alloy were investigated by thermo-desorption spectroscopy (TDS), where the hydride was submitted to a constant heating ramp (T_{rate}) of 1 °C/min under dynamic vacuum (10^{-6} mbar). The partial pressure of desorbed hydrogen is plotted as a function of temperature, showing a characteristic desorption profile of the quaternary alloy, shown in Figure 3.9.

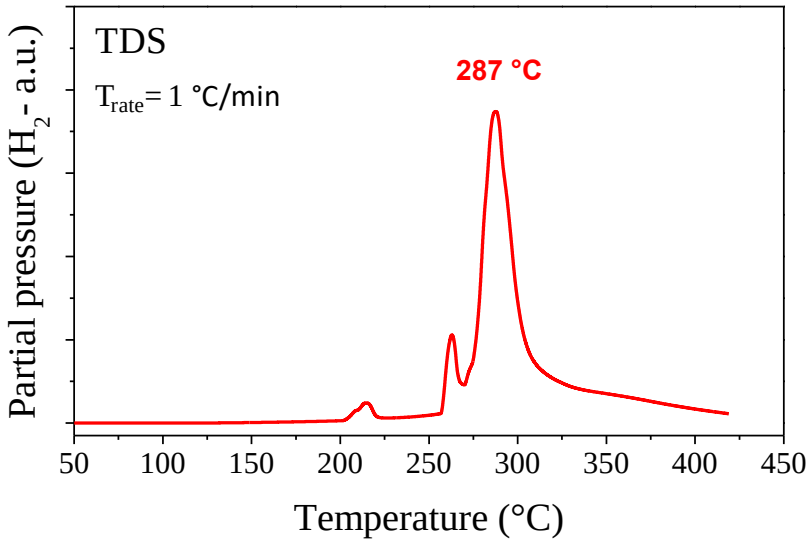

Figure 3.9. TDS curve of $Ti_{0.325}V_{0.275}Zr_{0.125}Nb_{0.275}H_{1.8}$ upon a constant heating rate of 1 °C/min.

The TDS curve reveals a main desorption peak with a temperature for maximum desorption rate (T_{max}) at 287 °C and an onset temperature at around ~275 °C. The desorption profile is in good agreement with the nD experiment, both showing a single desorption event at ~287 and 270 °C, respectively; the small temperature difference can be explained by the different environment and experimental conditions used in each measurement, which varies for both instruments (e.g. the amount of sample, the vacuum pressure, heat transfer rate, etc.).

After TDS, the desorbed phase of the alloy was characterized by XRD (Figure 3.10) showing a *bcc* structure with similar lattice constant as the as-cast alloy (desorbed: a_{bcc}= 3.253(1) Å and, as-cast: a_{bcc}= 3.261(1) Å). This confirms the reversibility of the alloy upon hydrogen absorption/desorption.

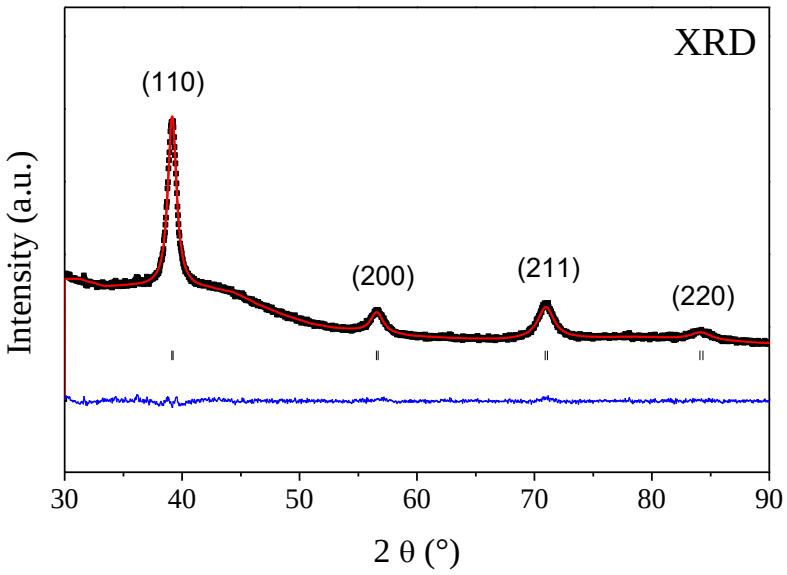

Figure 3.10. XRD of the desorbed $Ti_{0.325}V_{0.275}Zr_{0.125}Nb_{0.275}$ and corresponding Rietveld refinement with bcc structure (Im-3m) and lattice parameter a_{bcc}= 3.253(1) Å. The observed data (experimental) is represented in black dots and the red line corresponds to the calculated data; the difference between the observed and calculated profiles is represented in blue.

Based on these results, the conditions for hydrogen desorption can be established for the evaluation of the hydrogen-cycling properties of the MPEA. The quaternary alloy can absorb hydrogen at very low equilibrium pressure, as observed in the PCI curve, therefore, the hydrogen desorption must be carried out under dynamic vacuum at a temperature above the T_{max}.

3.5 *Hydrogen absorption/desorption cycling*

With the established conditions for desorption, the alloy was then submitted to multiple cycles of hydrogen absorption and desorption, and evaluated in terms of hydrogen capacity expressed as H/*M* and wt.% (Figure 3.11). The sample was initially activated through heat treatment at 340 °C for 2 hours under dynamic vacuum. The absorption conditions consisted of a single dose of H_2 with a final equilibrium pressure of 25 bar at a constant temperature of 25 °C (thermostated in a water bath). The hydrogen desorption was carried out by heating the hydride up to 400 °C for 4 hours under dynamic vacuum (10^{-5} mbar), and the sample was left to cool down before the next absorption cycle.

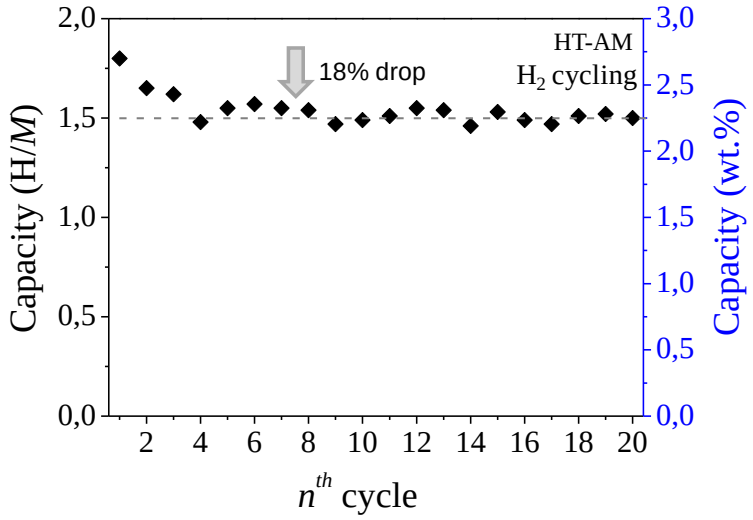

Figure 3.11. Evaluation of the hydrogen capacity $Ti_{0.325}V_{0.275}Zr_{0.125}Nb_{0.275}$ in terms of H/M and wt.% as a function of the number of hydrogen absorption/desorption cycles.

The quaternary alloy has an initial hydrogen capacity of 1.8 H/*M* in the first hydrogenation cycle and gradually decreases over the next 3 cycles, followed by a stabilization of the capacity at 1.5 H/*M* (2.3 wt.%), which remained constant up to 20 hydrogenation cycles. The stable capacity is represented by the dashed line, which represents 82% of the maximum storage capacity.

Structural, chemical, and thermo-desorption characterization after hydrogen-cycling

To study the effect of hydrogen-cycling on the material structure and the hydrogen sorption properties, the corresponding desorbed and hydride phases after 20 cycles were characterized by laboratory XRD, SEM-EDS, and TDS.

First, the structural properties of the desorbed alloy and hydride phase after cycling were studied by XRD, and compared to the diffraction patterns of the as-cast alloy and the hydride in the first hydrogenation cycle (1.8 H/*M*), see Figure 3.12.

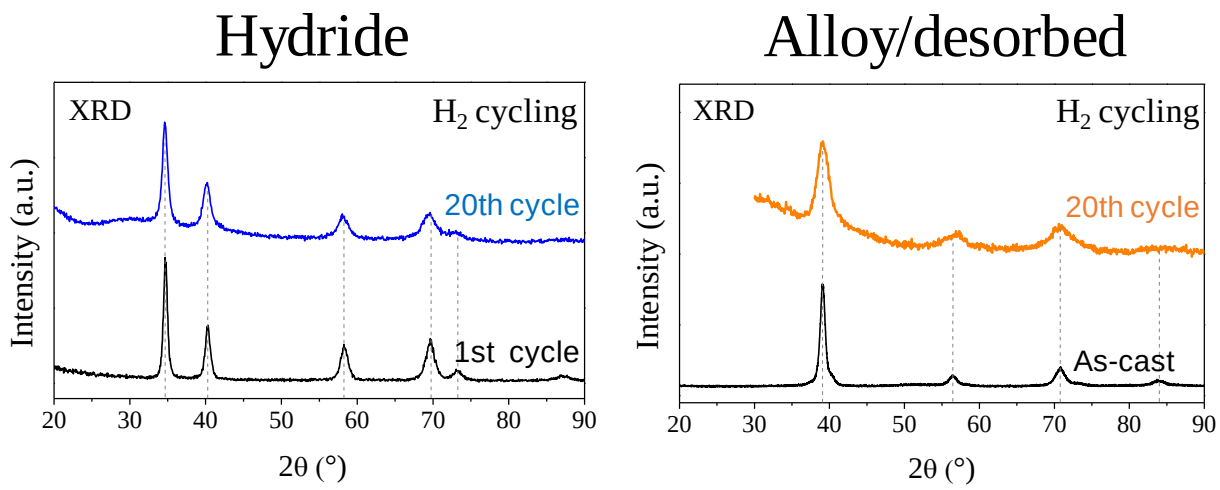

Figure 3.12. XRD patterns $Ti_{0.325}V_{0.275}Zr_{0.125}Nb_{0.275}$ before and after hydrogen-cycling. Left: hydride phases. Right: as-cast and desorbed phases.

The crystal structure of the cycled alloys, in both phases, is very similar to their initial counterparts, and there is no evidence of hydrogen-induced decomposition. Both phases have similar lattice parameters in the 1st (a_{bcc}= 3.261(1) Å, and a_{fcc}= 4.478(1) Å) and in the 20th (a_{bcc}= 3.253(1) Å, and a_{fcc}= 4.489(1) Å) hydrogenation cycle. The crystalline structure of the quaternary alloy with optimized composition can withstand hydrogen-cycling for at least 20 cycles. Nonetheless, it is noticeable a broadening of the diffraction peaks after hydrogen-cycling, this is due to the effect of hydrogen-embrittlement in metals. The enlargement of the diffraction peaks can be explained by a refinement of the crystal grains upon hydrogen-cycling, and the increased amounts of defects and strain in the structure lessen the crystallinity of the alloy. We hypothesize that the loss of crystallinity might be responsible for the decrease of H_2 capacity.

Next, SEM and EDS were carried out to study the chemical composition of the microstructure before and after hydrogen-cycling. This was performed on the hydride phases from the 1st and 20th hydrogenation cycles. Figure 3.13 shows the BSE images of a representative area at different magnification for each cycle.

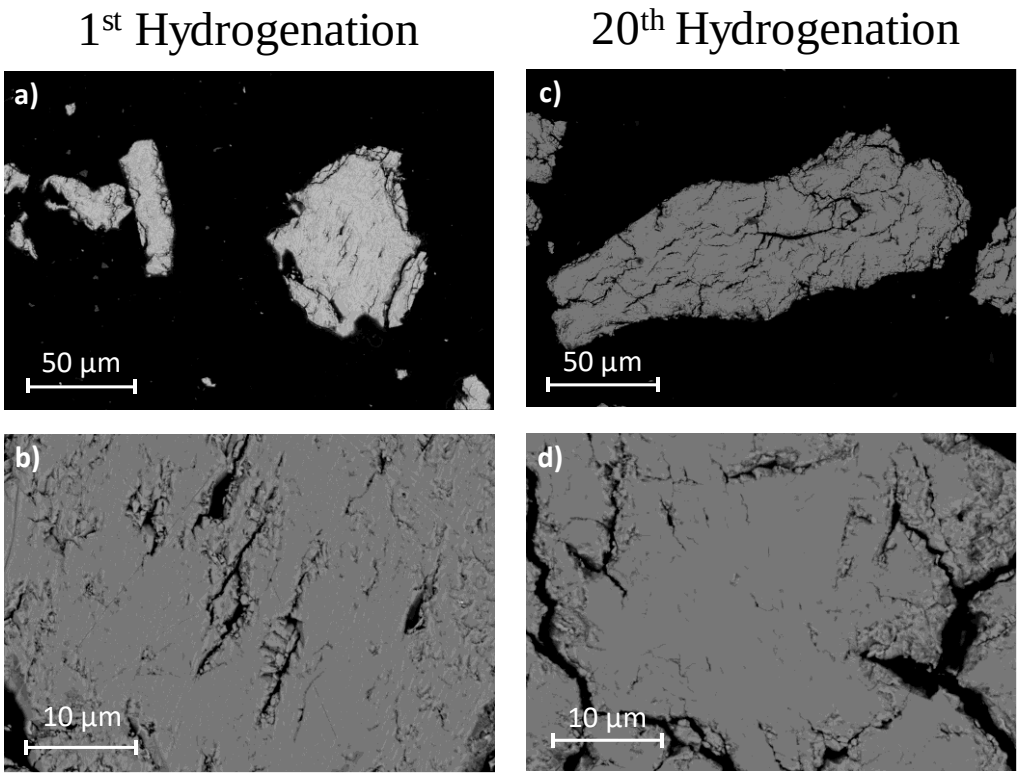

Figure 3.13. BSE images of $Ti_{0.325}V_{0.275}Zr_{0.125}Nb_{0.275}H_x$ in the 1st (a and b) and the 20th (c and d) hydrogenation cycle.

The absence of contrast of the BSE images on the 1st hydride (*a* and *b*) and the 20th hydride (*c* and *d*) suggests a homogeneous phase throughout the surface of the material. A significant amount of cracks and fissures are observed for the 20th hydrogenation cycle and only a few of them on the 1st hydrogenation. This is expected as the crystal lattice of the alloy transforms upon hydrogen absorption and desorption, expanding and contracting the unit cell repeatedly with each cycle. The material then losses its high crystallinity due to the severe strain caused by hydrogen and the refining of the grain boundaries, characterized by the enlargement of the diffraction peaks on the XRD patterns in Figure 3.12.

Chemical analysis by EDS was performed on the hydride phase to check the atomic concentration of the material before and after hydrogen-cycling. The element distribution images (chemical mapping) are presented in Figure 3.14 and Figure 3.15 for the first and last hydrogenation cycles, respectively.

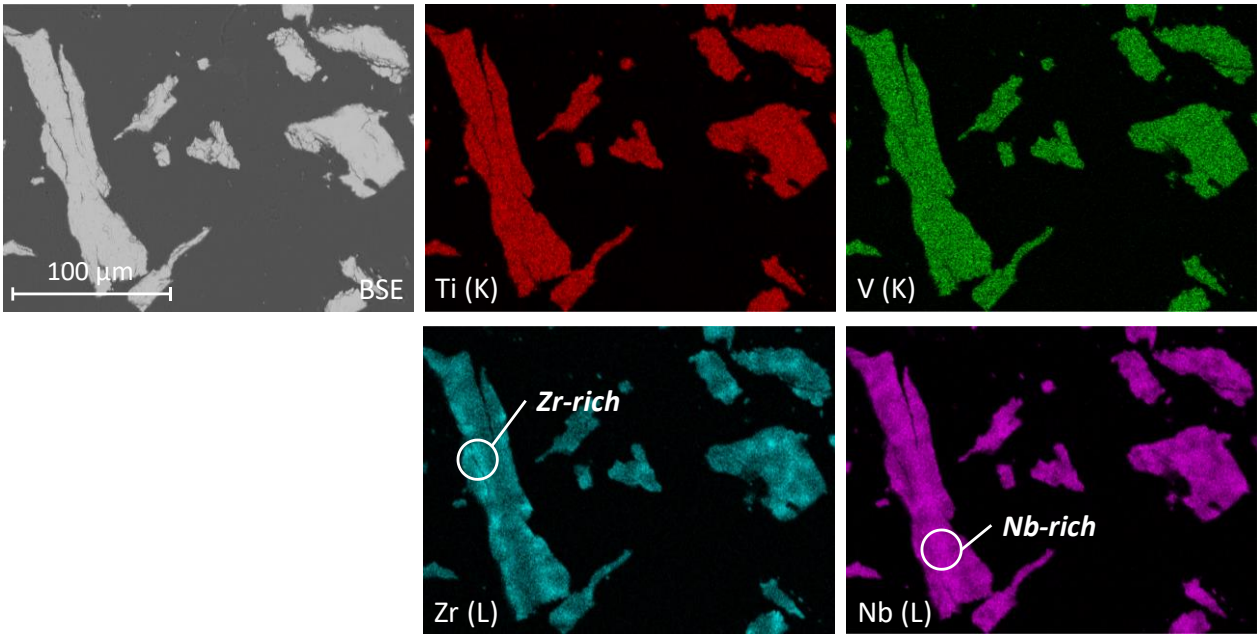

Figure 3.14. EDS chemical mapping of $Ti_{0.325}V_{0.275}Zr_{0.125}Nb_{0.275}$ in the 1st hydrogenation cycle (1.8 H/M).

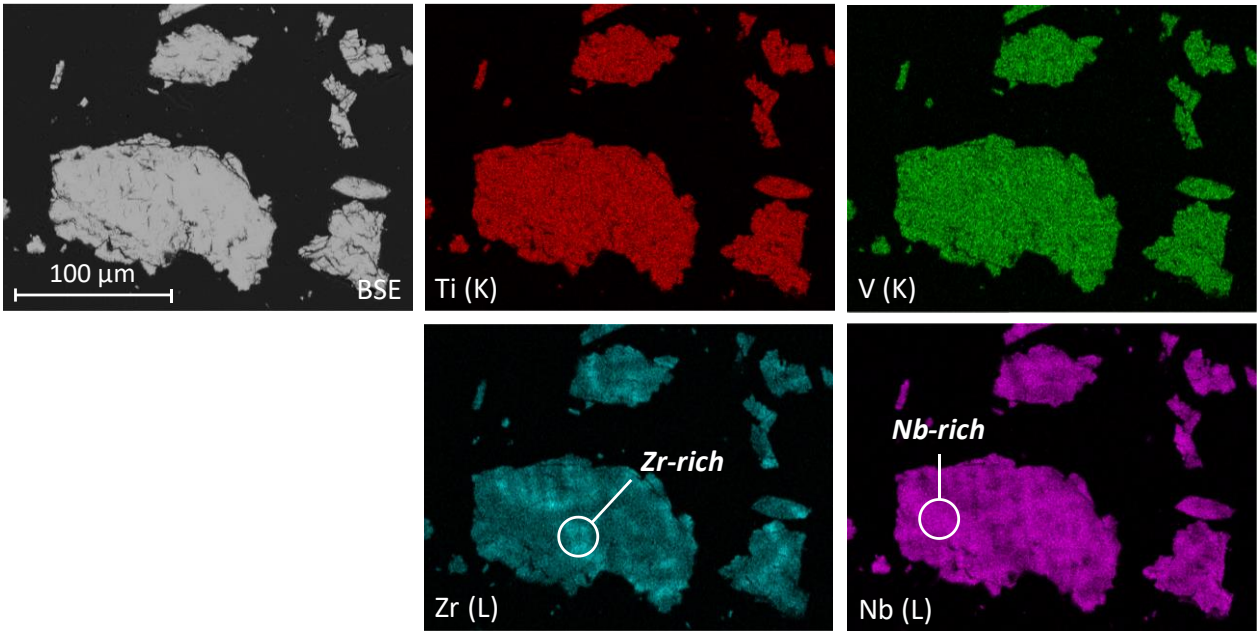

Figure 3.15. EDS chemical mapping of $Ti_{0.325}V_{0.275}Zr_{0.125}Nb_{0.275}$ in the 20th hydrogenation cycle (1.5 H/M).

The BSE images show a homogeneous microstructure on the 1st and 20th hydrogenation samples, however, the element distribution analysis reveals few regions rich in Zr with reduced Nb-content. Meanwhile, Ti and V elements are homogeneously distributed throughout the microstructure. The results of the chemical analyses are listed in Table 3.1 and Table 3.2 for the 1st and 20th hydrogenation

cycle, respectively. The quantification of the atomic concentration was determined using the Ti (K), V (K), Zr (L), and Nb (L) lines from the photon emission of core-electrons.

Table 3.1. Chemical analysis (EDS) of the different phases in the alloy $Ti_{0.325}V_{0.275}Zr_{0.125}Nb_{0.275}$ from the 1st hydrogenation cycle (1.8 H/M).

	Element	Ti	V	Zr	Nb
Nb-rich	Average, at%	32.1	26.9	10.8	30.2
	Standard deviation	0.3	0.4	0.8	1.1
Zr-rich	Average, at%	32.2	25.5	21.8	20.5
	Standard deviation	0.3	0.4	1.7	1.4
Overall mapping composition, at%		32.4	27.1	13.2	27.3

Table 3.2. Chemical analysis (EDS) of the different phases in the alloy $Ti_{0.325}V_{0.275}Zr_{0.125}Nb_{0.275}$ from the 20th hydrogenation cycle (1.5 H/M).

	Element	Ti	V	Zr	Nb
Nb-rich	Average, at%	32.5	26.7	10.8	30.0
	Standard deviation	0.3	0.4	0.5	0.9
Zr-rich	Average, at%	31.7	24.6	25.3	18.4
	Standard deviation	0.3	1.0	2.0	1.5
Overall mapping composition, at%		32.3	27.1	13.2	27.4

The atomic concentration in both phases (*Zr-rich* and *Nb-rich*) has close values to the nominal composition, with small chemical modulation, and this is true for both hydrides, before and after hydrogen cycling. Also, the atomic composition of both hydrides are similar between each other, within the error bar, and there is no indication of phase segregation after 20 hydrogenation cycles. These results support the structural and chemical stability of the quaternary alloy to withstand hydrogen-cycling without phase decomposition.

Finally, the hydride phase after 20 cycles was submitted to TDS characterization under the same experimental conditions as the first hydride, in section 3.4. The normalized TDS curves from both hydrides are plotted in Figure 3.16.

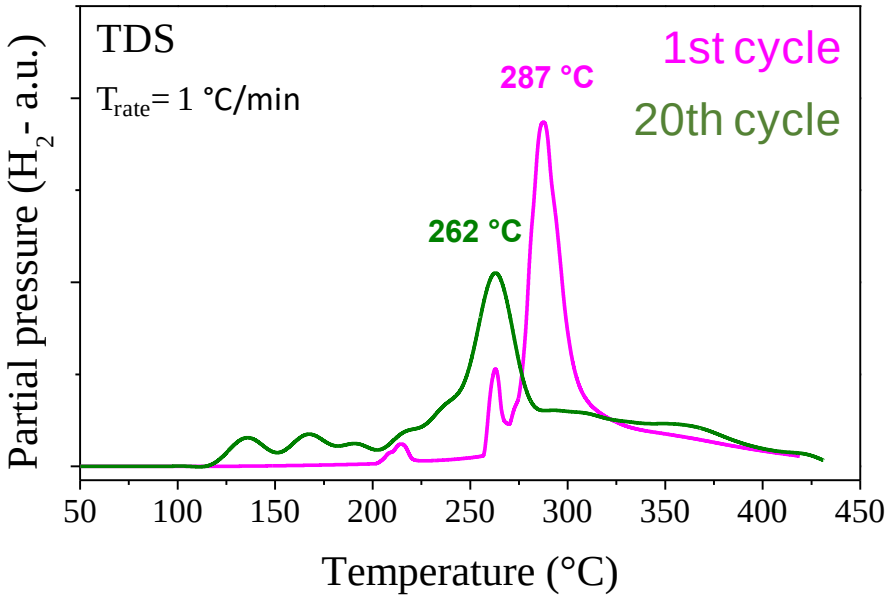

Figure 3.16. Normalized TDS curves of $Ti_{0.325}V_{0.275}Zr_{0.125}Nb_{0.275}H_x$ in the 1st (magenta) and 20th (green) hydrogenation cycle upon a constant heating rate of 1 °C/min.

The desorption profile of the cycled alloy is very similar to that of the first hydrogenation with a main desorption peak but shifted to a lower temperature, T_{max}= ~262 °C and 287 °C, respectively, suggesting faster kinetics for the cycled alloy. This may be explained in accordance with the conclusion from XRD. The reduction of the particle size and refinement of the grains after hydrogen-cycling shortens the diffusion lengths for hydrogen desorption, and therefore, the kinetics of desorption was improved.

In summary of the hydrogen-cycling evaluation, the quaternary alloy has demonstrated good performances with a reversible storage capacity of 82%, or 1.5 H/*M* (2.3 wt.%). XRD diffraction proves that the alloy retain the *bcc* and *fcc* structures of the initial alloy even after 20 hydrogenation cycles. The chemical analysis by EDS confirms the chemical stability of the alloy upon cycling and shows no indications of phase decomposition.

3.6 *Discussion with reported cases in the literature*

As an initial report on the hydrogen sorption properties, the results of the quaternary alloy, $Ti_{0.325}$ $V_{0.275}$ $Zr_{0.125}$ $Nb_{0.275}$, will be compared with the equimolar composition TiVZrNb reported in the literature[3], [10].

The quaternary alloy with optimized composition crystallized in a *bcc* structure (a_{bcc}= 3.261(1) Å) and underwent a phase transition upon hydrogenation into a *fcc* (a_{fcc}= 4.478(1) Å), with a maximum hydrogen capacity of 1.8 H/*M*. The lattice distortion calculated for this composition is δ= 6.0%. In comparison, the equimolar composition[3] has shown a phase transformation from a *bcc* structure (a_{bcc}= 3.308 (1) Å) to a *fcc* hydride (a_{fcc}= 4.534(1) Å), reaching a maximum hydrogen uptake of 2.0 H/*M* with a calculated lattice distortion of δ= 6.9%. The lattice constants of the equimolar compositions are slightly larger than our system, as well as the lattice distortion. This is consistent as Zr is the largest atom in the mixture and increasing its concentration will cause an expansion of the lattice and will increase the size disparity between the rest of the elements[1]. The H/*M* and δ values are slightly larger for the equimolar composition than those of the optimized composition, this may suggest a relationship between H/*M* and δ for MPEAs, however, this is still a working hypothesis[4] and more evidence is required to support this, as other factors may be involved in the absorption of hydrogen (e.g. chemical affinity towards hydrogen, valence electron concentration, etc).

The hydrogen desorption properties of the equimolar composition, TiVZrNb, were investigated by DSC, showing a main endothermic reaction with a desorption tail until around 500 °C. For the optimized composition, the TDS and nD experiments show a main desorption peak with a minor desorption tale, particularly noticed from the shift of the diffraction peaks in the thermo-diffractogram. However, the desorbed phase of the equimolar alloy decomposed into two *bcc* structures, probably due to the high temperature used in the DSC analysis (~1000 °C). In an earlier study of the same group, the authors investigated a series of alloys with different Zr-content and it was concluded that MPEAs with Zr-concentrations higher than 12.5 at% tend to decompose into two *bcc* phases after hydrogen desorption[10].

Bibliography

[1] Y. F. Ye, Q. Wang, J. Lu, C. T. Liu, and Y. Yang, "High-entropy alloy: challenges and prospects," *Materials Today*, vol. 19, no. 6, pp. 349–362, Jul. 2016, doi: 10.1016/j.mattod.2015.11.026.

[2] Gordon Aylward and Tristan Findlay, "SI Chemical Data, 3rd edition," *J. Chem. Educ.*, vol. 72, no. 5, p. A109, May 1995, doi: 10.1021/ed072pA109.1.

[3] M. M. Nygård, G. Ek, D. Karlsson, M. Sahlberg, M. H. Sørby, and B. C. Hauback, "Hydrogen storage in high-entropy alloys with varying degree of local lattice strain," *International Journal of Hydrogen Energy*, vol. 44, no. 55, pp. 29140–29149, Nov. 2019, doi: 10.1016/j.ijhydene.2019.03.223.

[4] M. Sahlberg, D. Karlsson, C. Zlotea, and U. Jansson, "Superior hydrogen storage in high entropy alloys," *Scientific Reports*, vol. 6, no. 1, Dec. 2016, doi: 10.1038/srep36770.

[5] D. Karlsson *et al.*, "Structure and Hydrogenation Properties of a HfNbTiVZr High-Entropy Alloy," *Inorganic Chemistry*, vol. 57, no. 4, pp. 2103–2110, Feb. 2018, doi: 10.1021/acs.inorgchem.7b03004.

[6] S. Kumar, A. Jain, T. Ichikawa, Y. Kojima, and G. K. Dey, "Development of vanadium based hydrogen storage material: A review," *Renewable and Sustainable Energy Reviews*, vol. 72, pp. 791–800, May 2017, doi: 10.1016/j.rser.2017.01.063.

[7] R. B. Schwarz, "Hydrogen Storage in Magnesium-Based Alloys," *MRS Bulletin*, vol. 24, no. 11, pp. 40–44, Nov. 1999, doi: 10.1557/S0883769400053446.

[8] K. T. Møller, T. R. Jensen, E. Akiba, and H. Li, "Hydrogen - A sustainable energy carrier," *Progress in Natural Science: Materials International*, vol. 27, no. 1, pp. 34–40, Feb. 2017, doi: 10.1016/j.pnsc.2016.12.014.

[9] D. J. M. King *et al.*, "High temperature, low neutron cross-section high-entropy alloys in the Nb-Ti-V-Zr system," *Acta Materialia*, vol. 166, pp. 435–446, Mar. 2019, doi: 10.1016/j.actamat.2019.01.006.

[10] M. M. Nygård, G. Ek, D. Karlsson, M. H. Sørby, M. Sahlberg, and B. C. Hauback, "Counting electrons - A new approach to tailor the hydrogen sorption properties of high-entropy alloys," *Acta Materialia*, vol. 175, pp. 121–129, Aug. 2019, doi: 10.1016/j.actamat.2019.06.002.

CHAPTER IV

~ Ti-V-Zr-Nb-Ta ~

CHAPTER 4: Ti-V-Zr-Nb-Ta

This project aims to implement a new strategy towards the understanding of the hydrogen sorption properties of MPEAs by studying the effect of adding a fifth element into the quaternary composition in the form of Ti-V-Zr-Nb-*M*. Three different elements were initially chosen for this project: *M*= Ta, Al, and Mg. The first one is a refractory element with similar properties as the elements in the base composition, and the last two, are lightweight elements which is a desired property for any storage unit. In this chapter, the synthesis and characterization of the Ta-containing alloy will be discussed for the optimized composition $Ti_{0.30}V_{0.25}Zr_{0.10}Nb_{0.25}Ta_{0.10}$ that has a calculated lattice distortion of 5.5%[1], [2] and VEC of. The results of this chapter were published in 2020[3].

4.1 Synthesis of Ti-V-Zr-Nb-Ta

The most suitable approach to synthesize an alloy purely made of refractory elements is by HT-AM[4], even though this composition was successfully prepared by ArBM, as demonstrated in the *preliminary results* section. The alloy was synthesized by mixing the elements and melting altogether in an Ar chamber under a constant electric arc for approximately 60 seconds per melting. The alloy adopted a single phase after 15 re-melts and the results of XRD are shown in Figure 4.1 along with its corresponding Rietveld refinement analysis.

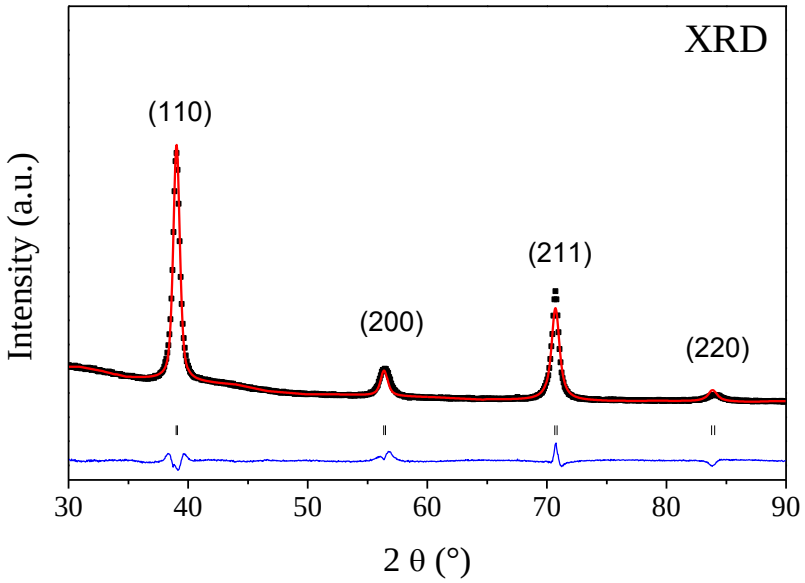

Figure 4.1. XRD of $Ti_{0.30}V_{0.25}Zr_{0.10}Nb_{0.25}Ta_{0.10}$ and corresponding Rietveld refinement with bcc structure (Im-3m) and lattice parameter a_{bcc}= 3.263(1) Å. The observed data (experimental) is represented in black dots and the red line corresponds to the calculated data; the difference between the observed and calculated profiles is represented in blue.

The Ta-quinary alloy crystallized in a *bcc* structure (*Im-3m* space group) with a lattice parameter a_{bcc}= 3.263(1) Å, similar to that of the quaternary alloy, a_{bcc}= 3.261(1) Å. This is not surprising since Ta has an atomic radius of 1.43 Å very close to Ti (1.45 Å) and Nb (1.43 Å), two of the other elements with the highest concentration. For comparison, the same alloy produced by ArBM in the preliminary section has a lattice parameter of a_{bcc}= 3.274(1) Å, which is slightly larger probably due to the strain introduced during ball milling.

4.2 Hydrogenation of Ti-V-Zr-Nb-Ta

The as-cast alloy was cut into smaller pieces and activated prior to hydrogenation. The alloy was then hydrogenated by submitting the sample to a single dose of H_2 with a final equilibrium pressure of 33 bar at 100 °C. The kinetics of absorption was recorded and plotted in Figure 4.2 *left*. Subsequently, the alloy was desorbed (at 400 °C for 10 hours under dynamic vacuum) and a pressure-composition isotherm (PCI) was measured for the second hydrogenation cycle at 25 °C (Figure 4.2 *right*).

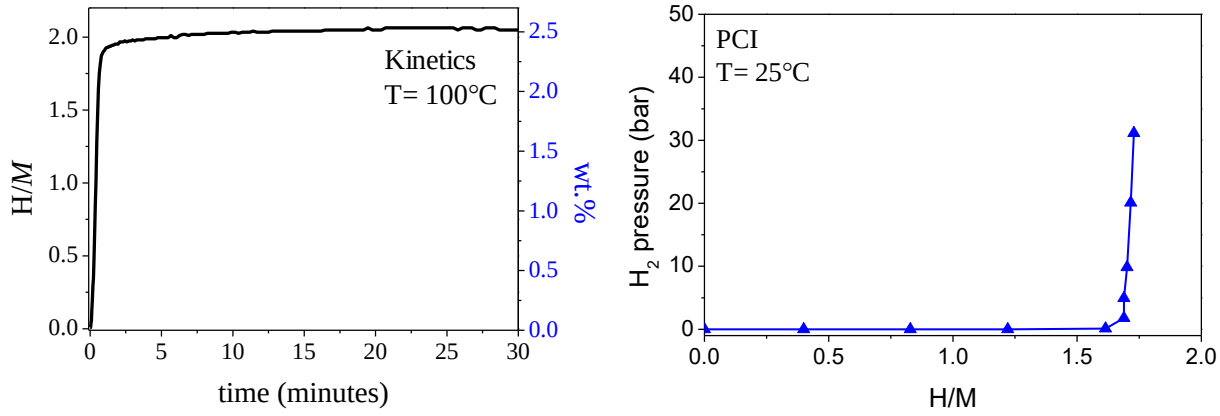

Figure 4.2. Kinetics of absorption at 100 °C (left – first hydrogenation) and PCI measured at 25 °C (right – second hydrogenation) of $Ti_{0.30}V_{0.25}Zr_{0.10}Nb_{0.25}Ta_{0.10}$.

The quinary alloy rapidly absorbed hydrogen up to 90% of its maximum capacity (2.0 H/*M*, or 2.5 wt.%) within the first 60 seconds at 100 °C. The maximum hydrogen capacity for the quinary alloy is higher than the quaternary alloy in terms of H/*M*, which is 1.8 H/*M* (2.7 wt.%). This implies that the addition of Ta (10 %) into the base composition allowed a higher hydrogen uptake. The value of wt.% is slightly lower for the Ta-quinary alloy due to the heavier molecular weight, 77.54 g/mol, when compared to that of the base alloy, 66.52 g/mol.

The PCI curve above reveals a single plateau pressure below 10^{-2} bar at 25 °C, similar to that of the quaternary, this time reaching a capacity of 1.7 H/*M* (2.2 wt.%) in the second hydrogenation cycle.

The structural properties of the hydride phase were determined for the hydride with 2.0 H/*M*. As stated in the previous chapter, SR-XRD offers a better resolution which can provide the evidence necessary to discriminate between closely related structures. For this analysis, the sample was finely hand-grinded and loaded into a capillary of 0.1 mm in diameter for SR-XRD characterization at the *Crystal* beamline in SOLEIL synchrotron facilities, France. The SR-XRD pattern and the corresponding Rietveld refinement in the *fcc* structure are shown in Figure 4.3.

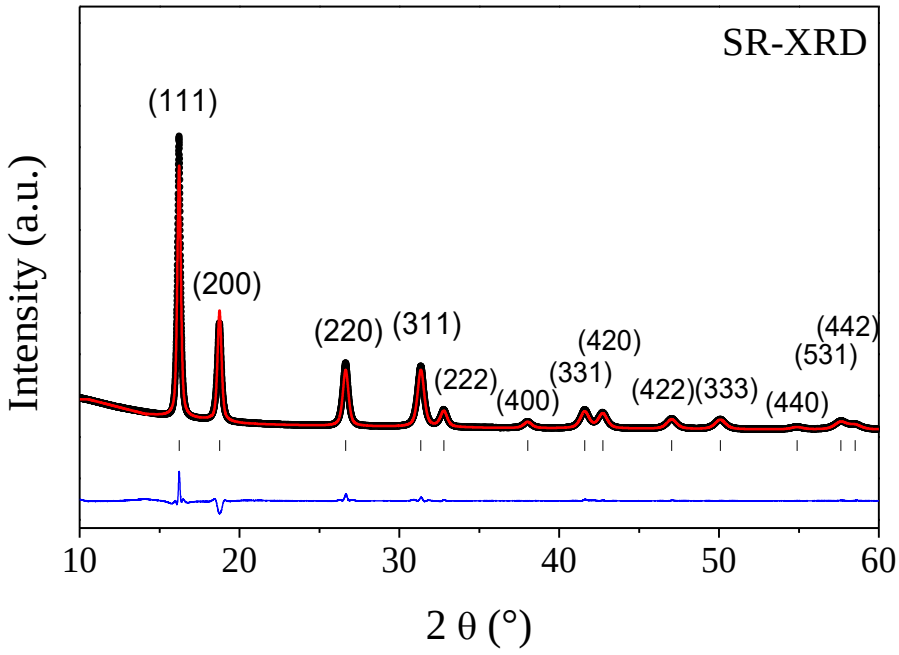

Figure 4.3. SR-XRD of the $Ti_{0.30}V_{0.25}Zr_{0.10}Nb_{0.25}Ta_{0.10}H_{2.0}$ hydride and corresponding Rietveld analysis with a fcc structure (Fm-3m) and lattice parameter a_{fcc}= 4.474(1) Å. The observed data (experimental) is represented in black dots and the red line corresponds to the calculated data; the difference between the observed and calculated profiles is represented in blue.

Following the discussion from the previous chapter regarding the impossibility to reliable discriminate between the *fcc* or *bct* (χ^2= 11.2 and R_B= 3.22 for the *fcc*, and; χ^2= 10.4 and R_B= 3.34 for the *bct*), the simplest structure was privileged to describe the crystalline structure of the hydride. Therefore, the Ta-quinary alloy adopts a *fcc* structure in the hydride phase with a lattice parameter a_{fcc}= 4.474(1) Å.

In summary, the quinary alloy $Ti_{0.30}$ $V_{0.25}$ $Zr_{0.10}$ $Nb_{0.25}Ta_{0.10}$ can rapidly absorb hydrogen up to a maximum capacity of 2.0 H/*M* (2.5 wt.%). This value surpasses that of the quaternary alloy, suggesting that the addition of 10 at% of Ta is beneficial for the hydrogen uptake. The Ta-containing alloy undergoes a phase transformation from a *bcc* to a *fcc* hydride phase upon hydrogenation.

4.3 *In-situ* neutron diffraction

In neutron characterization, hydrogen is replaced by deuterium to obtain a better signal-to-background ratio in the diffraction pattern. Therefore, the Ta-quinary alloy was exposed to a final equilibrium pressure of at least 25 bar of D_2 at room temperature, absorbing a maximum capacity

of 2.0 D/*M*. The *ex-situ* characterization was performed by loading the sample into a vanadium can and the results of diffraction and Rietveld analysis are presented in Figure 4.4.

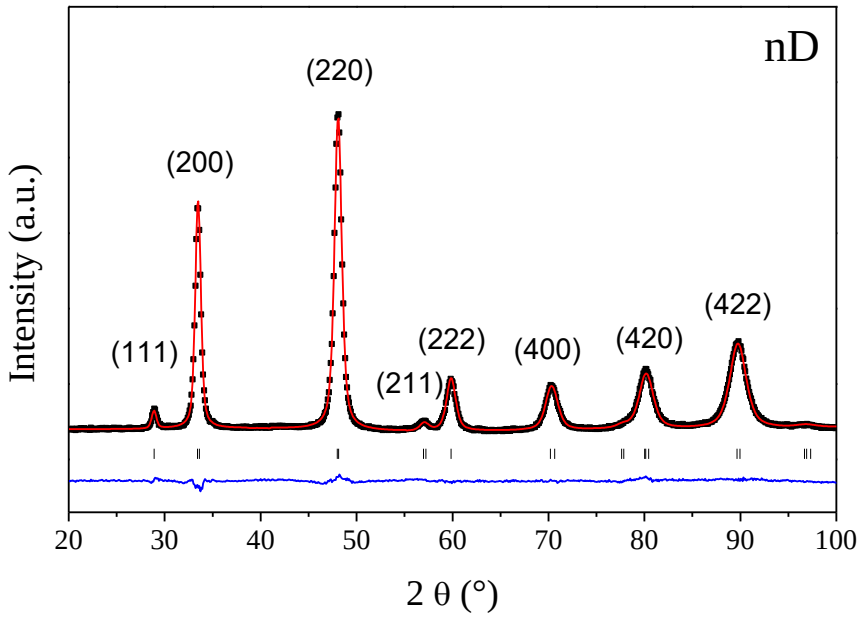

Figure 4.4. nD of the $Ti_{0.30}V_{0.25}Zr_{0.10}Nb_{0.25}Ta_{0.10}D_{2.0}$ and corresponding Rietveld analysis with a fcc structure (Fm-3m) and lattice parameter a_{fcc}= 4.466(1) Å. The observed data (experimental) is represented in black dots and the red line corresponds to the calculated data; the difference between the observed and calculated profiles is represented in blue.

The structural characterization by nD is in good agreement with the results from SR-XRD, with the deuteride phase adopting a *fcc* structure with lattice parameter a_{fcc}= 4.466(1) Å. The hydrogen atoms were determined to have a preferential occupation for the tetrahedral sites of the *fcc* structure, same as the quaternary alloy.

Next, *in-situ* neutron diffraction experiments were carried out during hydrogen desorption at a constant heating rate of 1 °C/min. The deuteride sample was loaded into a silica tube and connected to the vacuum rig with and evacuated under dynamic vacuum (10^{-5} mbar). Diffraction data were collected for a wide range in 2θ angle and the results are plotted in Figure 4.5. The pressure readings from the turbopump are plotted as a function of temperature and shown next to the thermo-diffractogram.

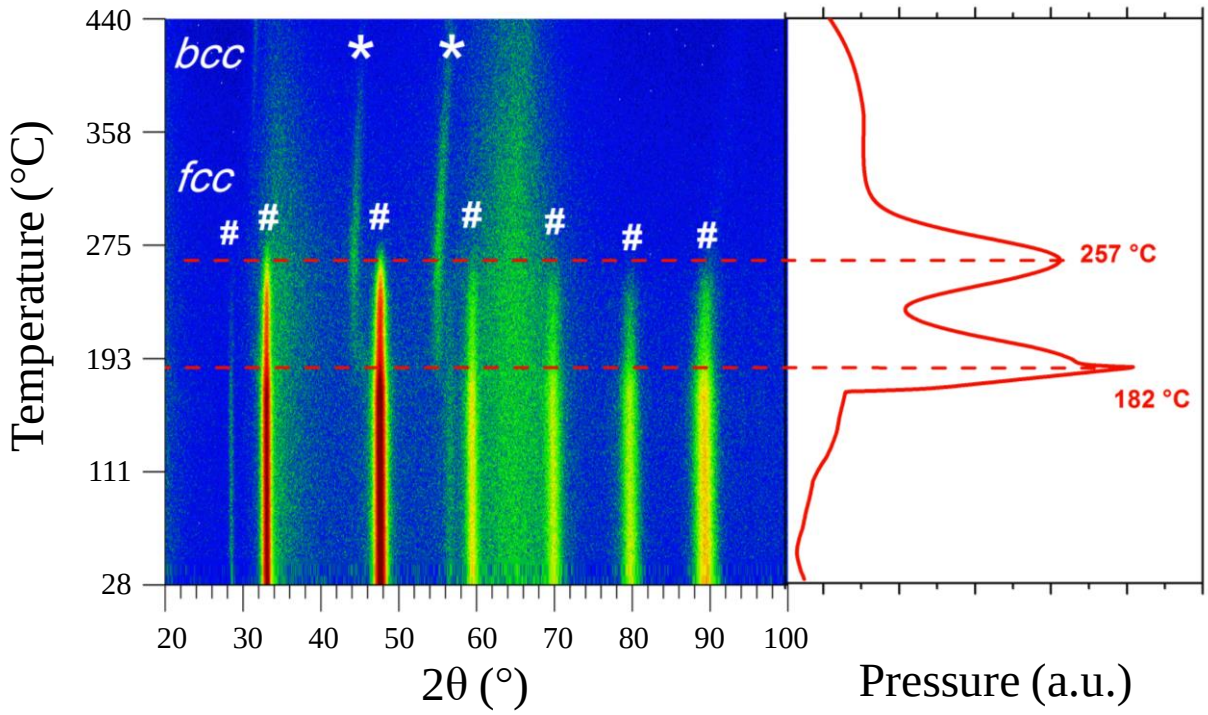

Figure 4.5. In-situ neutron diffraction of $Ti_{0.30}V_{0.25}Zr_{0.10}Nb_{0.25}Ta_{0.10}D_{2.0}$ heated at a constant temperature rate of 1 °C/min and the pressure readings during deuterium desorption.

The pressure profile on the right reveals two desorption events, at ~182 °C and ~257 °C, which are related to the structural transformation observed in the thermo-diffractogram. At room temperature, the diffraction peaks of the *fcc* hydride are marked with the hash symbol (#) while the broad diffraction signals around 32-36° and 60-70° correspond to the silica tube used as the sample holder. From bottom-up, increasing the temperature, the hydride phase remains stable up to ~182 °C, where the *fcc* signals lose intensity and the diffraction peaks of a new phase have appeared. These new diffraction peaks are indexed to a *bcc* structure, corresponding to the solid solution, and these are marked with the star symbol (*). This implies partial desorption of the hydride, where the *fcc* and *bcc* coexist for a temperature range of ~75 °C, in between the two desorption peaks. At around ~257 °C, the diffraction signals of the *fcc* hydride completely disappear, in line with the second desorption peak, leaving only the *bcc* phase at higher temperatures. Thus, the second desorption peak corresponds to the full transformation of the hydride phase into a solid solution. After this point, the *bcc* diffraction peaks slowly shift towards a higher 2θ angle due to deuterium atoms leaving the structure, reducing the lattice parameter in consequence. This is confirmed by the desorption profile on the right, showing a desorption tail after the second peak at ~257 °C. The

phase transitions from nD are in good agreement with the desorption peaks, as indicated by the dashed lines.

It is interesting to compare this result with that observed in the quaternary alloy. The Ta-quinary alloy showed two desorption events with a temperature gap of around ~75 °C, whereas the quaternary alloy only showed a single-desorption peak where the phase transition occurred abruptly at ~270 °C. The quinary alloy has a significantly lower onset temperature than that of the quaternary alloy. This may suggest a destabilization of the hydride phase by the addition of Ta (10 at%).

In summary, the Ta-containing alloy forms a hydride phase with *fcc* structure where hydrogen atoms occupy the tetrahedral interstitial sites. Two desorption events were observed for the quinary alloy, nonetheless, only a single phase transformation was observed during deuterium desorption, from a *fcc* → *bcc* structure. This confirms the single-plateau region observed in the PCI curve of the Ta-quinary alloy.

4.4 *Thermo-desorption characterization*

To study the hydrogen desorption properties, two thermo-desorption techniques were used for the characterization of the Ta-quinary alloy: thermo-desorption spectroscopy (TDS) and differential scanning calorimetry (DSC). For TDS characterization, the hydride was submitted to a constant heating rate of 1 °C/min under dynamic vacuum (10^{-6} mbar) and the results are plotted in Figure 4.6.

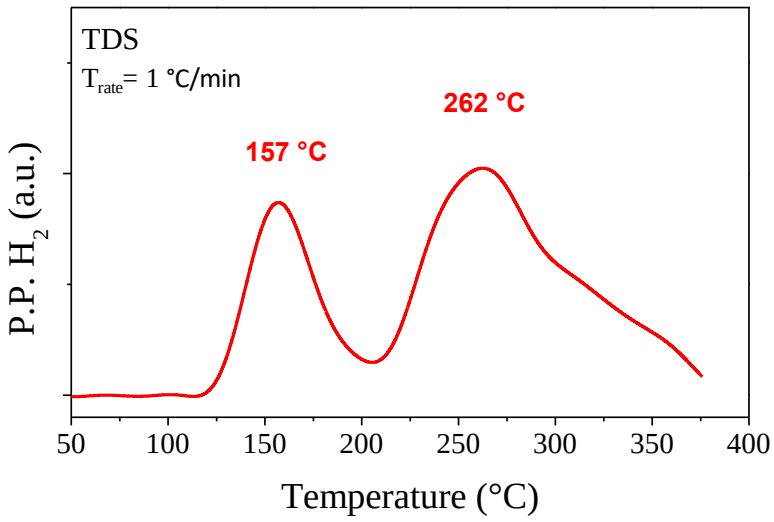

Figure 4.6. TDS curve of $Ti_{0.30}V_{0.25}Zr_{0.10}Nb_{0.25}Ta_{0.10}H_{2.0}$ upon a constant heating rate of 1 °C/min.

Two desorption peaks are observed in TDS, at 157 °C and 262 °C, comparable to those observed in the *in-situ* nD experiment, and with an onset temperature at around ~130 °C. The temperature difference between TDS and nD results is a consequence of the different instruments used for each measurement, as explained in the previous chapter. The first desorption peak corresponds to partial desorption, while the second peak corresponds to the full transformation of the *fcc* hydride into the *bcc* solid solution. This was not observed for the quaternary alloy which only shows a single desorption peak with an onset temperature at around ~275 °C. This suggests that the addition of 10 at% of Ta decreased the onset temperature for hydrogen desorption.

The quinary alloy was also characterized by DSC during a French-Brazilian collaboration in 2019 with the University of São Carlos. The hydride from the first hydrogenation (2.0 H/*M*) was submitted to a twin-test using a DSC calorimeter coupled to a quadrupole mass spectrometer (QMS) and a temperature ramp of 10 °C/min using a continuous flow of Ar as the gas carrier. DSC is a thermal analysis technique that allows the identification of different processes occurring in the material upon heating (endothermic or exothermic), such as the hydrogen desorption in metal hydrides or a physical structural transformation[5]. The released gases upon heating are analyzed by QMS, in this case, only hydrogen is released. By comparing the DSC and the QMS signals, it is possible to discriminate between a chemical desorption process or a physical transformation. The results of DSC-QMS characterization are shown in Figure 4.7.

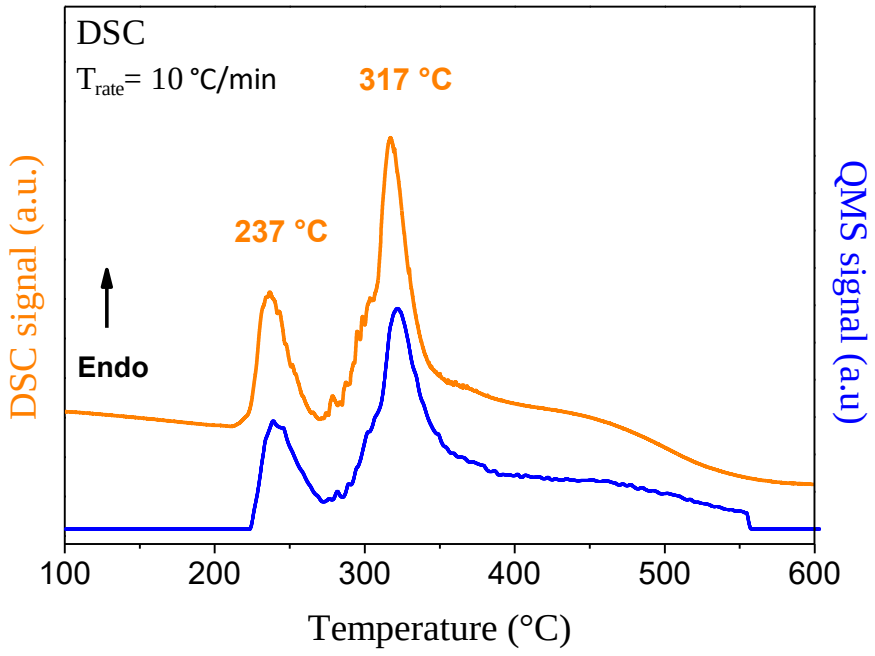

Figure 4.7. DSC-QMS curve of $Ti_{0.30}V_{0.25}Zr_{0.10}Nb_{0.25}Ta_{0.10}H_{2.0}$ upon a constant heating rate of 10 °C/min under Ar flow as the gas carrier. The heat flow measured by the DSC is represented by the orange line, and the ion-counts of hydrogen (H^+) measured by QMS with the blue line.

Two main endothermic processes occur at different temperatures, 237 °C and 317 °C. These are perfectly described by the intensity of the QMS signal for H_2, revealing that both thermal events correspond to the desorption process of hydrogen. The DSC-QMS profiles are very similar to those observed in nD and TDS with two desorption peaks separated by approximately ~80 °C. In DSC, these peaks occur at a higher temperature range and this is mainly due to the higher heating rate used in the measurement. Typically, higher heating rates tend to shift the desorption temperatures towards higher temperatures[5]. However, other factors are influencing the temperature of desorption, such as the pressure conditions (dynamic vacuum or Ar-flow) and the principle of the technique used for the measurement (pressure readings, temperature change, or ion-counts).

After hydrogen desorption, the structural properties of the alloy were characterized by XRD and Rietveld refinement (Figure 4.8). The desorbed alloy recovered the initial a *bcc* structure with a slightly smaller lattice parameter than the as-cast alloy (desorbed: a_{bcc}= 3.246(5) Å and, as-cast: a_{bcc}= 3.263(1) Å).

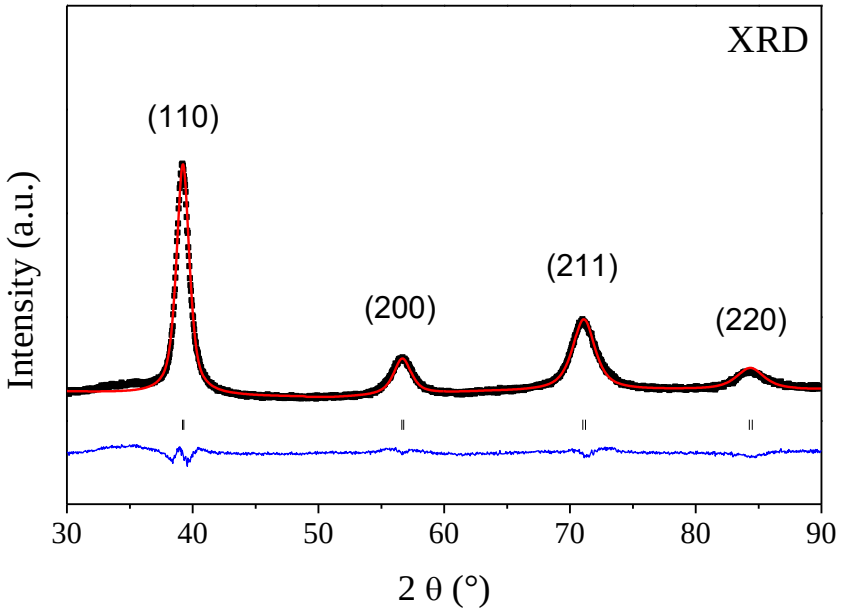

Figure 4.8. XRD of the desorbed $Ti_{0.30}V_{0.25}Zr_{0.10}Nb_{0.25}Ta_{0.10}$ and corresponding Rietveld refinement with bcc structure (Im-3m) and lattice parameter a_{bcc}= 3.246(5) Å. The observed data (experimental) is represented in black dots and the red line corresponds to the calculated data; the difference between the observed and calculated profiles is represented in blue.

With these results, the hydrogen desorption conditions can be established for the hydrogen-cycling evaluation. Similar to the quaternary alloy, to ensure the full desorption of the phase, the Ta-containing alloy should be heated up to 400 °C while under dynamic vacuum.

4.5 *Hydrogen absorption/desorption cycling*

The alloy was then submitted to hydrogen absorption-desorption-cycling, where the reversible storage capacity was evaluated by measuring the hydrogen capacity over 20 hydrogenation cycles. Similar to the quaternary alloy, the absorption conditions consisted of a single dose of H_2 with a final equilibrium pressure of 25 bar at 25 °C (thermostated in a water bath), and hydrogen desorption was carried out at 400 °C for 10 hours under dynamic vacuum (10^{-5} mbar). The results of the hydrogen-cycling are plotted in Figure 4.9.

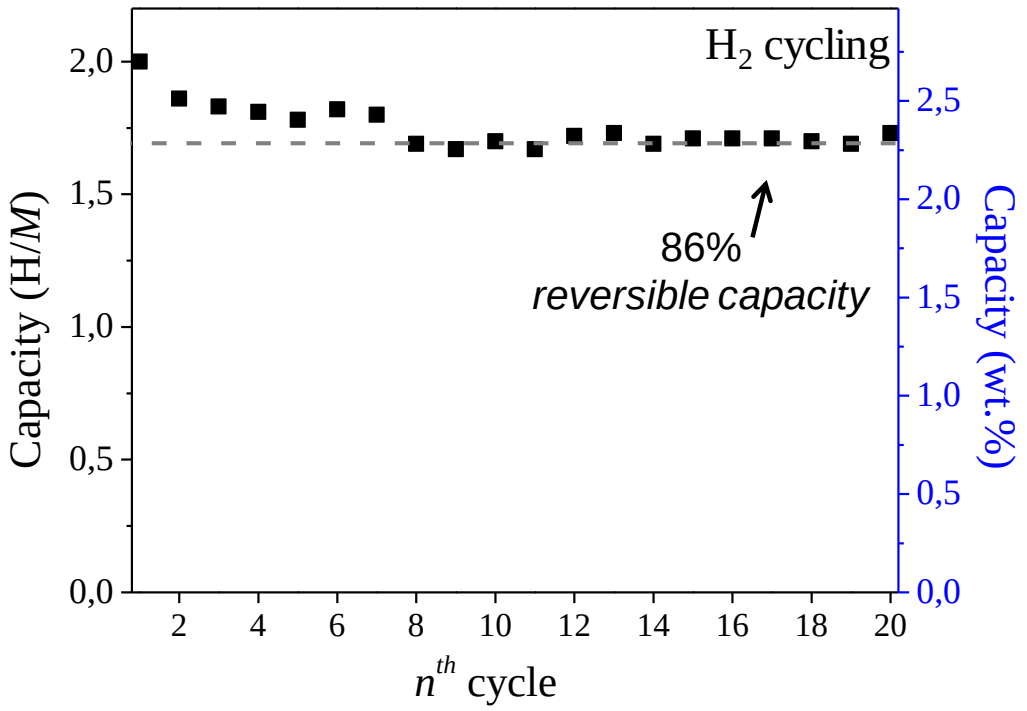

Figure 4.9. Evaluation of the hydrogen capacity of $Ti_{0.30}V_{0.25}Zr_{0.10}Nb_{0.25}Ta_{0.10}$ in terms of H/M and wt.% as a function of the number of hydrogen absorption and desorption cycles.

A fade of the capacity of the quinary alloy is observed during the first 7-8 hydrogenation cycles, followed by a stabilization of the capacity which is represented by the dashed line at around 1.7 H/*M* (2.3 wt.%). The Ta-containing has a reversible storage capacity of 86% (1.7 H/*M*) of the initial capacity, which is slightly larger than that of the quaternary alloy with 82% (1.5 H/*M*).

Structural, chemical, and thermo-desorption characterization after hydrogen-cycling

To study the effect of hydrogen-cycling on the material structure and the hydrogen sorption properties, the quinary alloy (desorbed) and its corresponding hydride phase were characterized by laboratory XRD, SEM-EDS, TDS, and DSC, and compared to their initial properties from the as-cast alloy and the hydride phase at 2.0 H/*M*.

First, the crystalline structure of the hydride and the desorbed phase were characterized by XRD. The diffraction patterns of both phases are plotted in Figure 4.10, along with their initial counterparts.

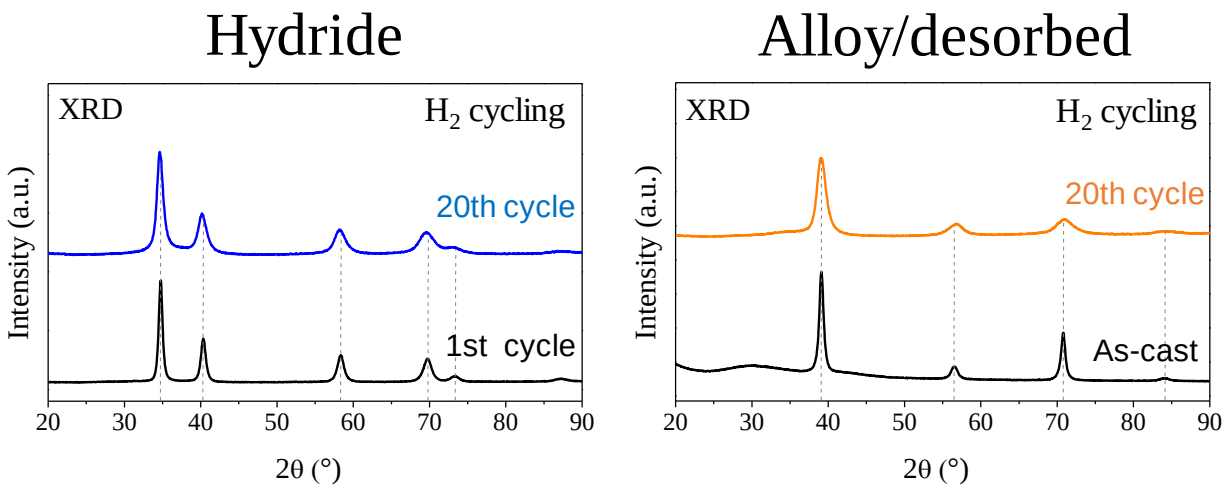

Figure 4.10. XRD patterns of $Ti_{0.30}V_{0.25}Zr_{0.10}Nb_{0.25}Ta_{0.10}$ before and after hydrogen-cycling. Left: hydride phases. Right: as-cast and desorbed phases.

The hydride phase (*left*) and the desorbed alloy (*right*) both maintain a single-phase even after 20 hydrogenation cycles, and the lattice parameters in the 1st (a_{bcc}= 3.263(1) Å, and a_{fcc}= 4.474(1) Å) and 20th (a_{bcc}= 3.246(5) Å, and a_{fcc}= 4.479(1) Å) cycle are nearly the same. As discussed in the previous chapter, there is an enlargement of the diffraction peaks which indicates the loss of crystallinity in the material structure, consequence of hydrogen-cycling. Yet, these results are good indicators of the alloy stability after several cycles.

Next, SEM and EDS characterizations were carried out for the hydride phase in the 1st and 20th hydrogenation cycle, with 2.0 and 1.7 H/*M* respectively. A representative section of the samples is displayed in the BSE images in Figure 4.11.

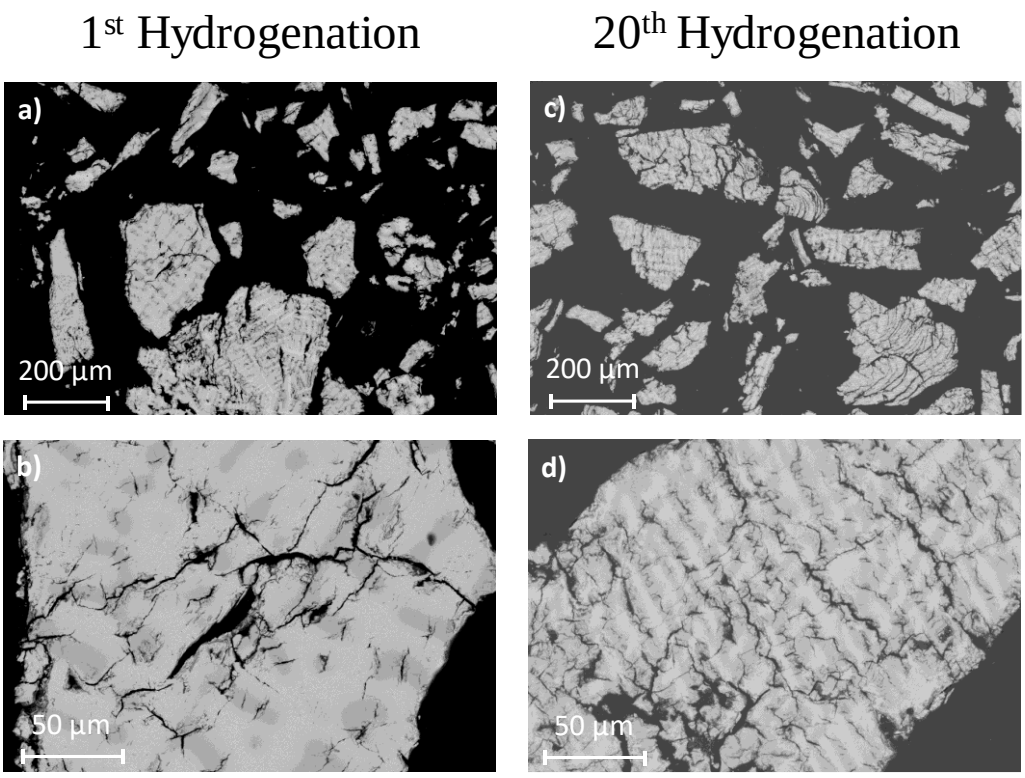

Figure 4.11. BSE images of $Ti_{0.30}V_{0.25}Zr_{0.10}Nb_{0.25}Ta_{0.10}H_x$ in the 1st (a and b) and the 20th (c and d) hydrogenation cycle.

The BSE images of the hydride phases reveal a semi-dendritic microstructure by the contrast in brightness, showing a main *light gray* phase and a minor *dark gray* phase. Significant amounts of cracks are observed in both samples, more severe in the cycled alloy (*c* and *d*), due to hydrogen-embrittlement. This is expected as the lattice expands and contracts repeatedly during the absorption and desorption of hydrogen, respectively. It is noticed that most of the fractures occur in the *dark gray* areas of the microstructure.

These phases, *light gray* and *dark gray*, were analyzed by EDS to study their chemical composition and the results are listed in Table 4.1 and 4.2 for the 1st and 20th hydrogenation cycles, respectively. Additionally, a chemical mapping was performed on both samples revealing the element distribution. These results are shown in Figures 4.12 and 4.13 for the first and last hydrogenation cycles, respectively. The quantification of the atomic concentration was determined using the Ti (K), V (K), Zr (L), Nb (L), and Ta (M) lines from the photon emission of core-electrons.

Table 4 1. Chemical analysis (EDS) of the different phases in the alloy $Ti_{0.30}V_{0.25}Zr_{0.10}Nb_{0.25}Ta_{0.10}$ from the 1st hydrogenation cycle (2.0 H/M).

	Element	Ti	V	Zr	Nb	Ta
light gray	Average, %	25.9	20.3	5.6	32.2	16.0
	Standard deviation	1.0	0.7	0.3	0.8	0.9
dark gray	Average, %	30.8	25.6	21.1	17.9	4.6
	Standard deviation	0.6	1.2	3.0	1.3	0.8
Overall mapping composition, %		28.5	24.3	9.7	26.0	11.5

Table 4.2. Chemical analysis (EDS) of the different phases in the alloy $Ti_{0.30}V_{0.25}Zr_{0.10}Nb_{0.25}Ta_{0.10}$ from the 20th hydrogenation cycle (1.7 H/M).

	Element	Ti	V	Zr	Nb	Ta
light gray	Average, %	28.0	22.8	7.8	29.6	11.8
	Standard deviation	0.7	0.9	0.7	1.2	1.0
dark gray	Average, %	30.3	25.4	12.1	24.5	7.79
	Standard deviation	0.5	0.9	1.5	1.5	1.2
Overall mapping composition, %		29.5	24.8	10.1	26.0	9.6

In the 1st hydride, the *light gray* area has a chemical composition with a slightly richer concentration in Nb(~32 at%) and Ta(~16 at%) than the nominal composition, and a decreased content by around 4-5% in Ti, V, and Zr. Meanwhile, the *dark gray* area is Zr-rich(~21 at%) and poor in Nb- and Ta-concentration (~18 and ~5 at% respectively). The chemical analysis of the 20th hydrogenation shows a smaller chemical modulation between the two phases (*light* and *dark gray*), suggesting the microstructure underwent a chemical homogenization with hydrogen-cycling. However, these are initial results from a small portion of the sample and the number of fissures is significantly larger for the 20th hydrogenation, which may affect the analysis. Thus, further analysis is necessary to support this conclusion.

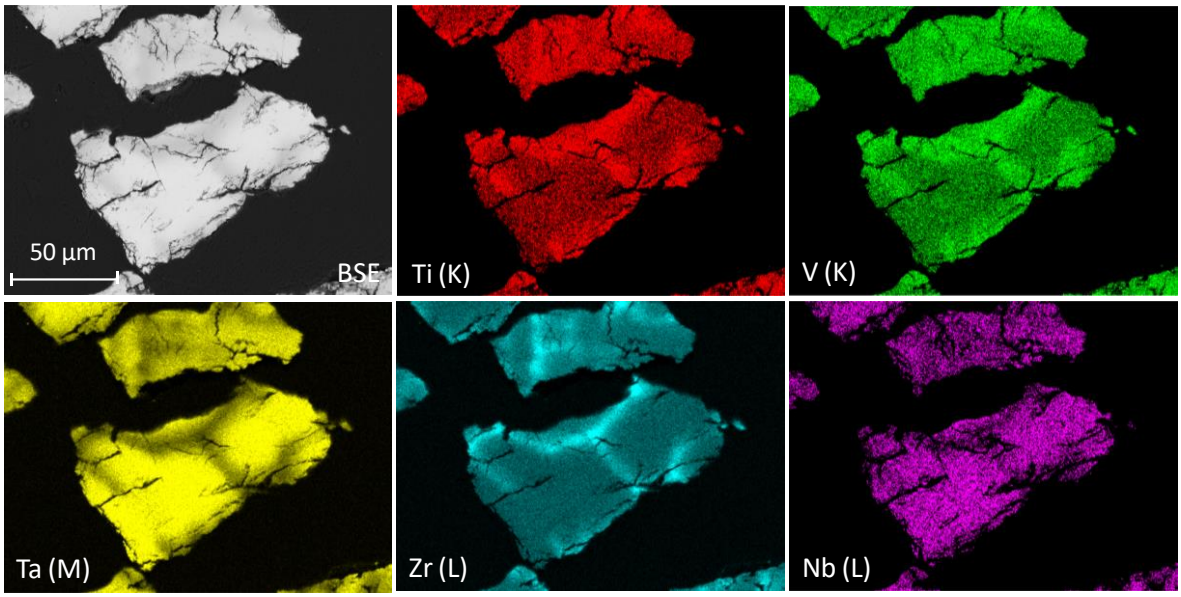

Figure 4.12. EDS chemical mapping of $Ti_{0.30}V_{0.25}Zr_{0.10}Nb_{0.25}Ta_{0.10}$ in the 1st hydrogenation cycle (2.0 H/M).

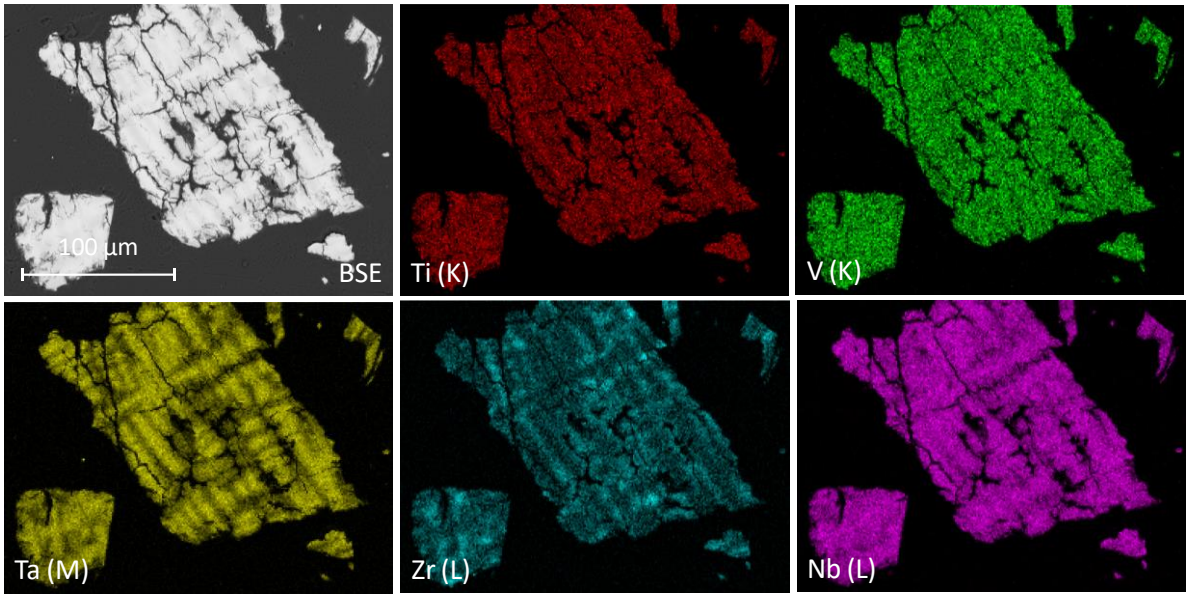

Figure 4.13. EDS chemical mapping of $Ti_{0.30}V_{0.25}Zr_{0.10}Nb_{0.25}Ta_{0.10}$ in the 20th hydrogenation cycle (1.7 H/M).

The EDS chemical mapping shows the element distribution in the microstructure revealing a dendritic array of the two phases, one rich in Zr and the second rich in Ta and Nb, while Ti and V are homogeneously distributed throughout the microstructure.

Next, TDS characterization was performed on the hydride phase after 20 cycles (1.7 H/*M*) under the same experimental conditions as the first hydrogenation (2.0 H/*M*). The results from TDS are shown in Figure 4.14 along with the TDS curve from the first hydride. Similarly, a DSC measurement was carried out for a hydride sample, this time only cycled 10 times, and the results of DSC are plotted in Figure 4.15.

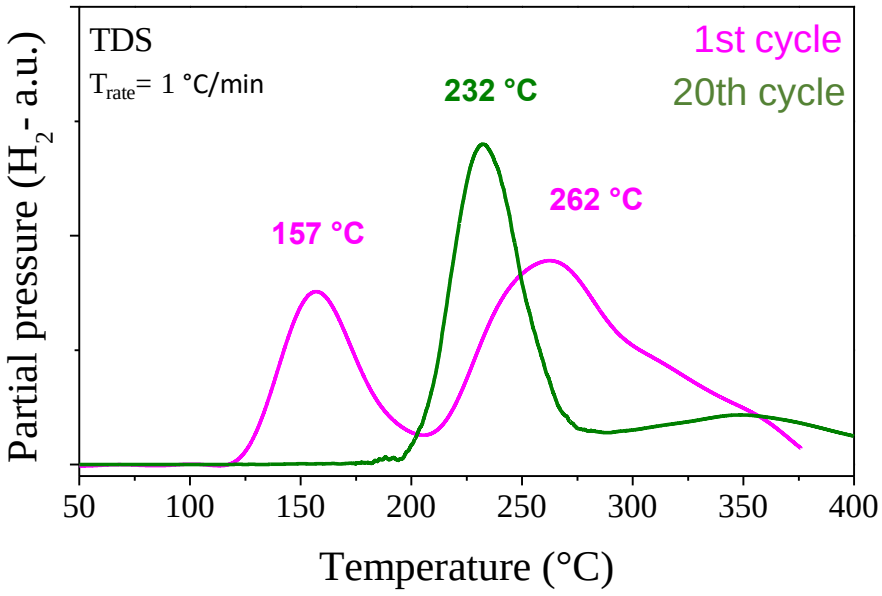

Figure 4.14. Normalized TDS curves of $Ti_{0.30}V_{0.25}Zr_{0.10}Nb_{0.25}Ta_{0.10}H_x$ in the 1st (magenta) and 20th (green) hydrogenation cycle, under a constant heating rate of 1 °C/min.

Interestingly, the thermo-desorption profile of the hydride after 20 cycles does not show two desorption events as the first hydride, in contrast, only a single desorption event is observed, similar to the profile measured for the quaternary alloy. The disappearance of the first desorption event may be related to the material loss in capacity after hydrogen-cycling. The desorption peak of the 20th hydrogenation cycle is slightly shifted towards a lower temperature, compared to the second event in the 1st cycle. This may be explained from a kinetics perspective, where the hydrogen desorbed has shorter diffusion lengths due to a refinement of the grain after cycling.

Similarly, DSC measurement shows a main endothermic event occurring at around ~315 °C, and the curve is perfectly described by the QMS signal of hydrogen (not shown in the figure), relating the thermal event with hydrogen desorption. The temperature of desorption of the main peak matches

that of the second endothermic event in the first cycle, ~317 °C. Similar to TDS, the first desorption event has disappeared in DSC.

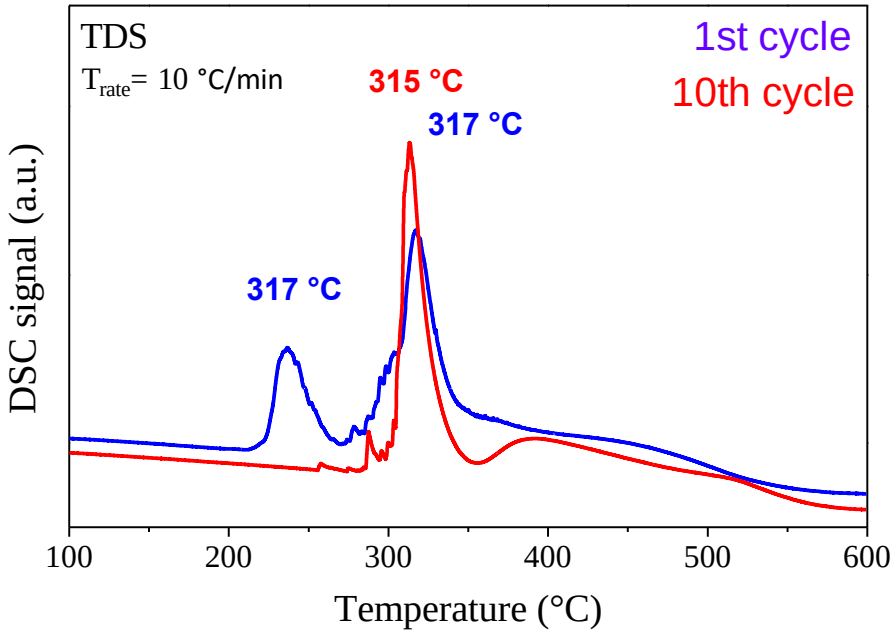

Figure 4.15. DSC curves of $Ti_{0.30}V_{0.25}Zr_{0.10}Nb_{0.25}Ta_{0.10}H_x$ in the 1st (blue) and 10th (red) hydrogenation cycle, under a constant heating rate of 10 °C/min, using Ar flow as the gas carrier.

A simple comparison of the integrated areas under the curve of the QMS signals from both samples inform us about the decrease of the hydrogen capacity[1]. The area under the curve after 10 hydrogenation cycles is 84% that of the first hydride, which is in good agreement with the results from the hydrogen-cycling evaluation in Figure 4.9. Losing hydrogen capacity over cycling is a widespread phenomenon and in many cases, this can be explained by phase segregation, however, this is not the case for Ta-containing alloy, as it was proven by XRD, SEM and EDS analyses. The loss of crystallinity, as proven by XRD, might be one of the reasons for the drop in capacity during cycling.

In summary, the Ta-containing alloy showed interesting hydrogen-cycling performances and can reversibly store up to 86%, or 1.7 H/*M* (2.2 wt.%) for over 20 hydrogenation cycles. The hydride and desorbed phases after cycling retain the same structure as the initial phases, without any indication

[1] The signal of the DSC is not used to calculate the relative amount of hydrogen because other thermal reaction may contribute to the DSC signal leading to a wrong estimation.

of phase decomposition by XRD and EDS. The SEM characterization and chemical analysis revealed a dendritic microstructure for the Ta-containing alloy, with some areas rich in Zr, and others with a high concentration of Ta and Nb.

4.6 *Comparison with the quaternary alloy*

The quaternary and the Ta-containing alloy, both, have similar structural properties before and after hydrogenation. The alloys crystallized in single *bcc* phase after HT-AM synthesis, and after hydrogen absorption, the full-hydride phase adopted a *fcc* structure, with similar lattice parameters (quaternary alloy: a_{bcc}= 3.261(5) Å and a_{fcc}= 4.478(1) Å; and Ta-HEA: a_{bcc}= 3.263(1) Å and a_{fcc}= 4.474(1) Å).

The addition of 10% of Ta caused a few changes in the hydrogen properties as compared to the base composition. In absorption, the hydrogen capacity of the alloy increased by 0.2 H/*M* relative to the base alloy, with a maximum capacity of 2.0 H/*M*. In terms of kinetics, both alloys can rapidly absorb hydrogen at room temperature conditions after a thermo-activation treatment. In hydrogen desorption, a secondary desorption peak appeared with a decreased onset temperature for the Ta-containing alloy, ~130 °C, as compared to the quaternary alloy, ~275 °C. Nonetheless, in-situ nD experiments confirmed a single-phase transformation during hydrogen desorption.

The hydrogen-cycling performances were very similar for the quaternary and Ta-quinary alloys, with a reversible storage capacity of around 82-86% of their respective initial capacity. In terms of wt.%, the alloys have the same reversible storage capacity of 2.3 wt.%. Both MPEAs were able to retain their respective crystalline structure after hydrogen-cycling up to 20 cycles without phase decomposition, as characterized by XRD, SEM, and EDS.

Bibliography

[1] Y. F. Ye, Q. Wang, J. Lu, C. T. Liu, and Y. Yang, "High-entropy alloy: challenges and prospects," *Materials Today*, vol. 19, no. 6, pp. 349–362, Jul. 2016, doi: 10.1016/j.mattod.2015.11.026.

[2] Gordon Aylward and Tristan Findlay, "SI Chemical Data, 3rd edition," *J. Chem. Educ.*, vol. 72, no. 5, p. A109, May 1995, doi: 10.1021/ed072pA109.1.

[3] J. Montero *et al.*, "Hydrogen storage properties of the refractory Ti–V–Zr–Nb–Ta multi-principal element alloy," *Journal of Alloys and Compounds*, vol. 835, p. 155376, Sep. 2020, doi: 10.1016/j.jallcom.2020.155376.

[4] M. Sahlberg, D. Karlsson, C. Zlotea, and U. Jansson, "Superior hydrogen storage in high entropy alloys," *Scientific Reports*, vol. 6, no. 1, Dec. 2016, doi: 10.1038/srep36770.

[5] J. F. Fernández, F. Cuevas, and C. Sánchez, "Simultaneous differential scanning calorimetry and thermal desorption spectroscopy measurements for the study of the decomposition of metal hydrides," *Journal of Alloys and Compounds*, vol. 298, no. 1, pp. 244–253, Feb. 2000, doi: 10.1016/S0925-8388(99)00620-9.

CHAPTER V

~ Ti-V-Zr-Nb-Al ~

CHAPTER 5: Ti-V-Zr-Nb-Al

The next HEA in this project is the alloy containing 10 at% of Al as the fifth element into the base composition Ti-V-Zr-Nb-Al. Aluminum is a lightweight element of the *group 13* of the periodic table, with different electronic properties than the *transition metals* used in this composition and which does not possess electrons in the *d*-orbital. The Al-quinary alloy with composition $Ti_{0.30}$ $V_{0.25}$ $Zr_{0.10}$ $Nb_{0.25}Al_{0.10}$ has a calculated lattice distortion of 5.5%[1], [2].

5.1 Synthesis of Ti-V-Zr-Nb-Al

Even though aluminum has a much lower melting point (~660 °C) than the rest of the elements in the mixture (~1600-2400 °C), HT-AM was still a viable approach to synthesize the Al-quinary alloy with nominal composition, thanks to the high boiling point and relatively low vapor pressure of Al. The Al-quinary alloy was successfully prepared in a single phase only after 20 re-melts under our synthesis conditions. The XRD pattern and the structural fitting of the Rietveld analysis are presented in Figure 5.1.

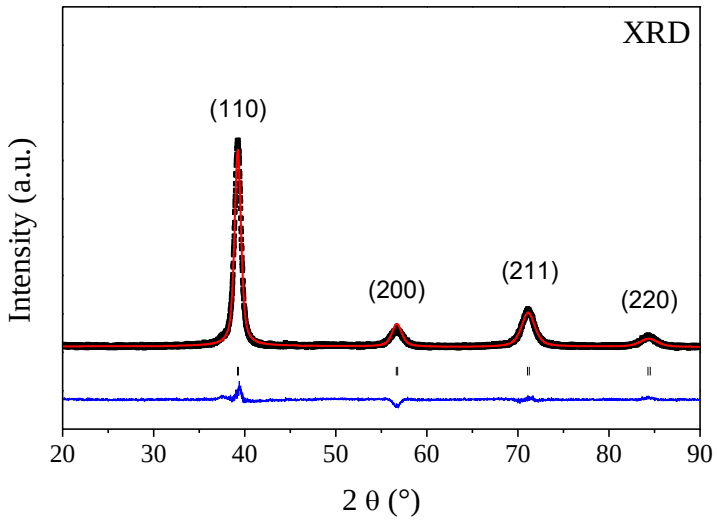

Figure 5.1. XRD of $Ti_{0.30}V_{0.25}Zr_{0.10}Nb_{0.25}Al_{0.10}$ and corresponding Rietveld refinement with bcc structure (Im-3m) and lattice parameter a_{bcc}= 3.247(1) Å. The observed data (experimental) is represented in black dots and the red line corresponds to the calculated data; the difference between the observed and calculated profiles is represented in blue.

The as-cast alloy crystallized in a single *bcc* structure (*Im-3m*) with lattice parameter a_{bcc}= 3.247(1) Å, this value alloy is slightly lower than that of the quaternary alloy a_{bcc}= 3.261(1) Å. This may be explained by the lower lattice distortion in the Al-quinary alloy (5.5 %) than in the quaternary alloy (6.0%).

5.2 Hydrogenation of Ti-V-Zr-Nb-Al

Then, the as-cast alloy was submitted to an activation treatment prior to hydrogenation. The hydrogenation was carried out by exposing the alloy to H_2 with a final equilibrium pressure of ~25 bar at 25 °C, the kinetics of absorption is plotted in Figure 5.2 *left*. Then, the sample was desorbed at 400 °C for 10 hours under dynamic vacuum, and re-hydrogenated, this time, measuring a PCI at 25 °C (Figure 5.2 *right*).

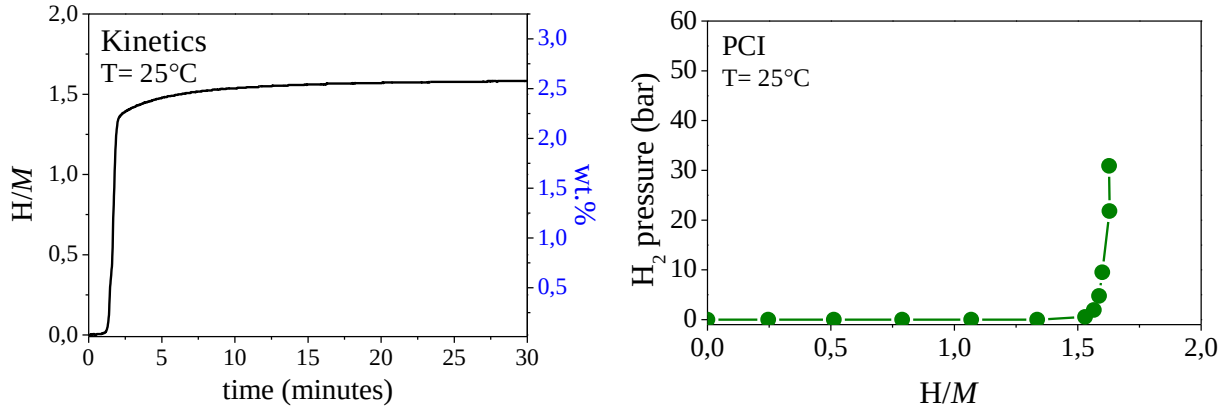

Figure 5.2. Kinetics of absorption at 25 °C (left – first hydrogenation) and PCI measured at 25 °C (right – second hydrogenation) of $Ti_{0.30}V_{0.25}Zr_{0.10}Nb_{0.25}Al_{0.10}$.

The Al-quinary alloy has a maximum hydrogen storage capacity of 1.6 H/*M*, or 2.6 wt.%, in the first (kinetics – *left*) and second hydrogenation (PCI – *right*). The kinetics plot shows a small incubation time of 1-2 minutes and then, rapidly absorbs hydrogen reaching almost full capacity within the first 5 minutes at 25 °C. The PCI curve on the *right* suggests the alloy undergoes a single phase transformation at low equilibrium pressure, similar to the profile observed in the quaternary alloy. A second PCI, this time measured at 100 °C, is presented in Figure 5.3.

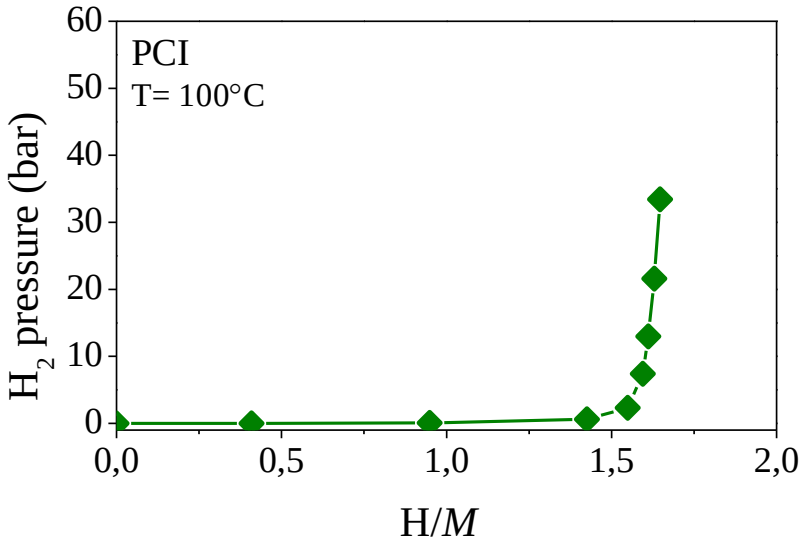

Figure 5.3. Pressure-composition isotherm of $Ti_{0.30}V_{0.25}Zr_{0.10}Nb_{0.25}Al_{0.10}$ measured at 100 °C.

The PCI curve at 100 °C shows a single plateau and a maximum hydrogen capacity of 1.6 H/*M*. The equilibrium pressure for hydride formation is still in the error bars of detection of the instrument (10^{-2} bar). Typically, higher temperatures increase the equilibrium pressure of hydride formation in the PCI plot, however, this is not observed for the Al-quinary. This further confirms that the Al-quinary alloy has only one phase transformation and forms a very stable hydride phase.

The structural properties of the hydride phase were then characterized by SR-XRD at the synchrotron facilities of SOLEIL. The structural refinement was carried out in the *fcc* and *bct* structures, however, only the *bct* fitting is presented in Figure 5.4.

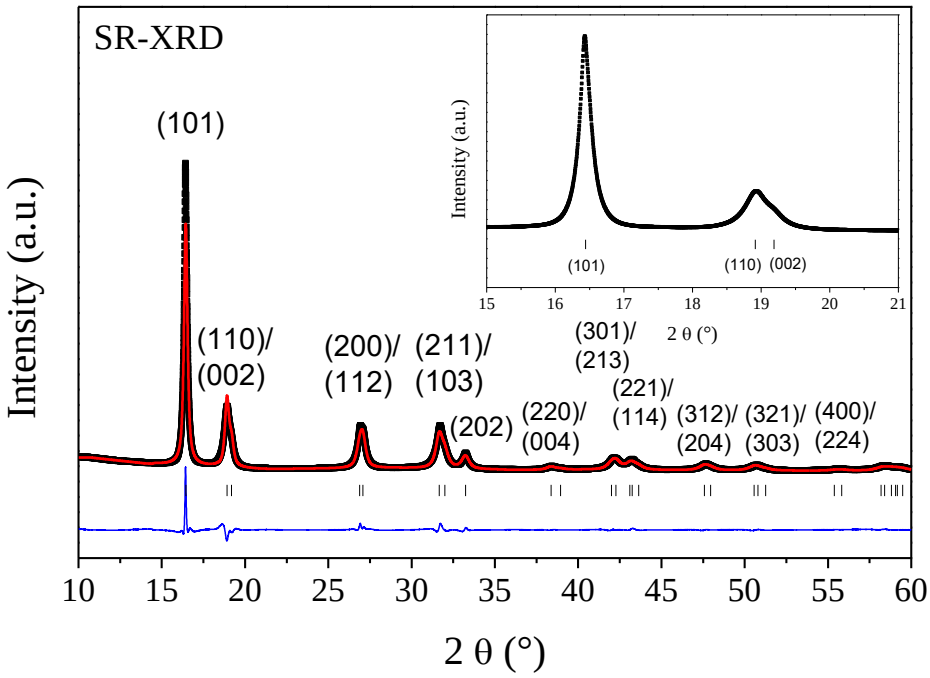

Figure 5.4. SR-XRD of the $Ti_{0.30}V_{0.25}Zr_{0.10}Nb_{0.25}Al_{0.10}H_{1.6}$ hydride and corresponding Rietveld analysis with bct structure (I4/mmm) and lattice parameter a_{bct}= 3.137(1) Å and c_{bct}= 4.374(1) Å. The observed data (experimental) is represented in black dots and the red line corresponds to the calculated data; the difference between the observed and calculated profiles is represented in blue. (Inset: zoom of the 2θ region 15-21°).

The evidence to discriminate between the *fcc* and *bct* is provided by the large difference between the agreement factors of the Rietveld analyses on both structures (χ^2_{bct}= 34.2 and χ^2_{fcc}= 68.2). The Al-quinary hydride, at the maximum hydrogen capacity (1.6 H/*M*), crystallizes in a *bct* structure (*I4/mmm*) with lattice parameters a_{bct}= 3.137(1) Å and c_{bct}= 4.374(1) Å. More evidence is found in the SR-XRD pattern, where a closer inspection of the diffraction peaks between 15-21° in 2θ (see *inset*), reveals the presence of two diffraction peaks overlapping at around 19°. These overlapping signals arise from the diffraction of the (110) and (002) planes of the *bct* lattice. This confirms the formation of the *bct* structure after hydrogenation.

In summary, the Al-quinary alloy has a maximum hydrogen uptake of 1.6 H/*M* with low equilibrium pressure for hydride formation. The as-cast alloy underwent a phase transformation from a *bcc* alloy to a *bct* hydride at full capacity. The hydride phase has a preferential crystallization into the *bct* structure, whereas the quaternary and the Ta-quinary alloys adopt a *fcc* structure. The addition of Al (10 at%) into the base composition has decreased the hydrogen capacity of the base alloy by 0.2 H/*M*, while the opposite effect is observed by the addition of Ta (10 at%).

5.3 *In-situ* neutron diffraction

The structural properties were further characterized by nD experiments. *ex-situ* measurement to locate the position of deuterium in the lattice, and *in-situ* thermo-desorption to study the structural transformation upon hydrogen desorption. A deuterated sample of the Al-containing alloy was prepared absorbing 1.6 D/*M*. The results of the *ex-situ* nD and structural refinement are presented in Figure 5.5.

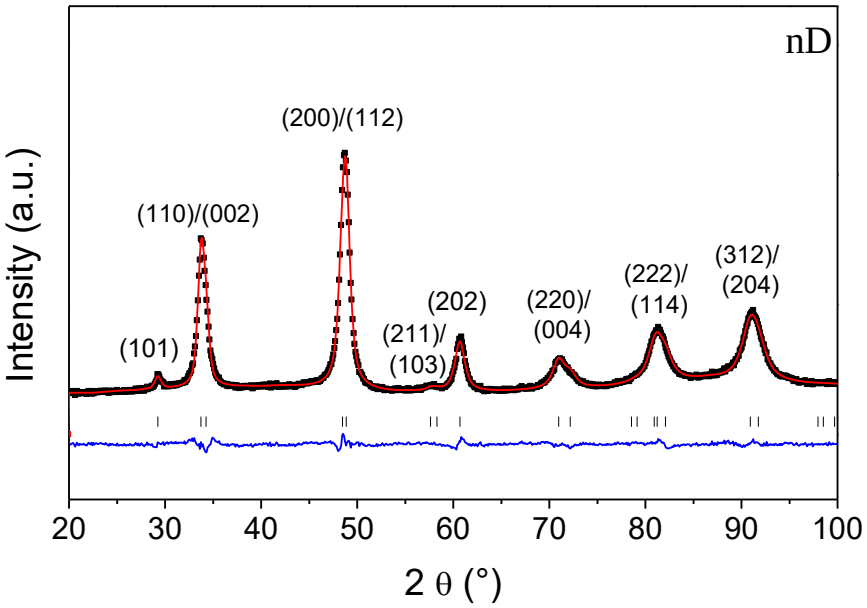

Figure 5.5. Ex-situ nD of the $Ti_{0.30}V_{0.25}Zr_{0.10}Nb_{0.25}Al_{0.10}D_{1.6}$ and corresponding Rietveld analysis with a bct structure (I4/mmm) and lattice parameter a_{bct}= 3.135(1) Å and c_{bct}= 4.370(1) Å. The observed data (experimental) is represented in black dots and the red line corresponds to the calculated data; the difference between the observed and calculated profiles is represented in blue.

The fitting of the nD pattern is in good agreement with the results from SR-XRD, confirming the preferential crystallization into the *bct* structure with lattice parameters a_{bct}= 3.135(1) Å and c_{bct}= 4.370(1) Å, and hydrogen atoms occupying at the tetrahedral interstitial sites.

Next, the *in-situ* thermo-desorption characterization was carried out. The sample was submitted to a constant heating rate of 1 °C/min up to ~450 °C while evacuating under dynamic vacuum (10^{-5} mbar). The results of the *in-situ* experiments are plotted in Figure 5.6, along with the pressure readings in the turbopump.

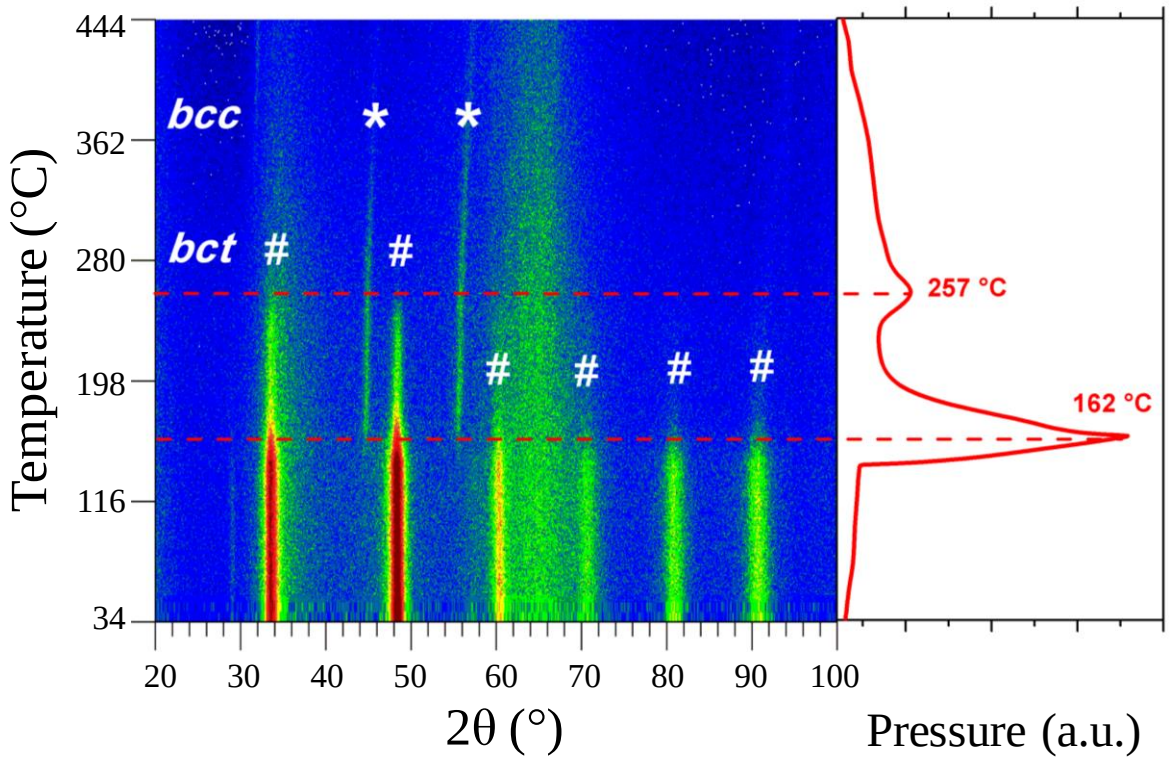

Figure 5.6. In-situ neutron diffraction of $Ti_{0.30}V_{0.25}Zr_{0.10}Nb_{0.25}Al_{0.10}D_{1.6}$ heated at a constant temperature rate of 1 °C/min and the pressure readings during deuterium desorption.

The pressure profile reveals two desorption events, a main peak at ~162 °C and a minor one at ~257 °C. These peaks have a direct correlation with the structural changes observed in the thermo-diffractogram. At room temperature, the diffraction signals of the *bct* hydride are marked with the hash symbol (#) and the broad signals between 32-36° and 60-70° in 2θ belong to the silica sample holder. With increasing temperature, the hydride structure remains stable up to ~150 °C, where the intensity of the *bct* signals rapidly fades. Only the major diffraction peaks at ~34° and 48° in 2θ remain visible. At ~150 °C, new diffraction peaks appear and these correspond to the *bcc* solid solution, marked with the star symbol (*). Both, *bct* and *bcc* phases, coexist for a temperature range of approximately ~90 °C, in between the two desorption events. This suggests the partial desorption of the material after the first desorption peak (~162 °C), whereas the second peak (~257 °C) corresponds to the complete transformation of the hydride into a *bcc* solid solution. At higher temperatures the *bcc* peaks shift towards a higher 2θ angle and, as explained before, this is due to hydrogen being released from the solid solution. This is confirmed by the desorption tail observed after the second desorption peak.

In summary, the desorption behavior of the Al-quinary hydride is very similar to that observed for the Ta-containing alloy, with two desorption events separated by a temperature gap of ~90 °C, and only one phase transformation. The hydrogen atoms were located in the tetrahedral sites of the *bct* structure.

5.4 *Thermo-desorption characterization*

The hydrogen desorption properties of the HEA were characterized by two thermo-desorption techniques: TDS and DSC. The TDS profile was recorded under a constant heating rate of 1 °C/min while under dynamic vacuum, and the results are shown in Figure 5.7.

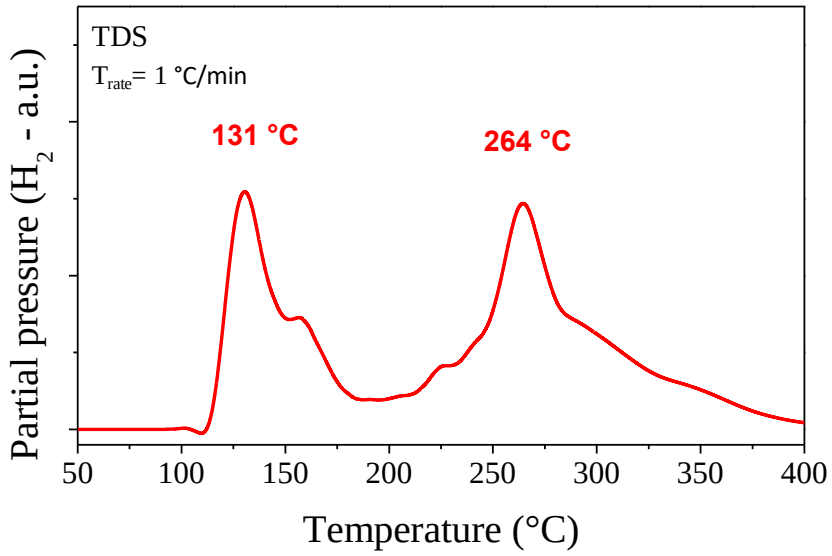

Figure 5.7. TDS curve of $Ti_{0.30}V_{0.25}Zr_{0.10}Nb_{0.25}Al_{0.10}H_{1.6}$ upon a constant heating rate of 1 °C/min.

The TDS curve above shows two main desorption peaks, at ~131 °C and ~264 °C, with temperatures comparable to those peaks observed in the nD, except for their relative intensities which are more balanced in TDS. The onset temperature of the Al-quinary alloy is at around ~110 °C, which is a significantly lower value than that of the quaternary alloy at around ~270 °C.

These results are very interesting when compared to the base composition, which has only one desorption event at ~287 °C. This suggests that the addition of a fifth element (Al and Ta) have

destabilized the hydride phase and significantly decreased the onset temperature in the quinary alloys, ~110 °C (Al) and ~130 °C (Ta).

The desorbed alloy was then characterized by XRD in Figure 5.8, revealing that the Al-containing alloy has recovered the *bcc* structure of the as-cast alloy with the same lattice parameter (desorbed: a_{bcc}= 3.246(1) Å and, as-cast: a_{bcc}= 3.247(1) Å).

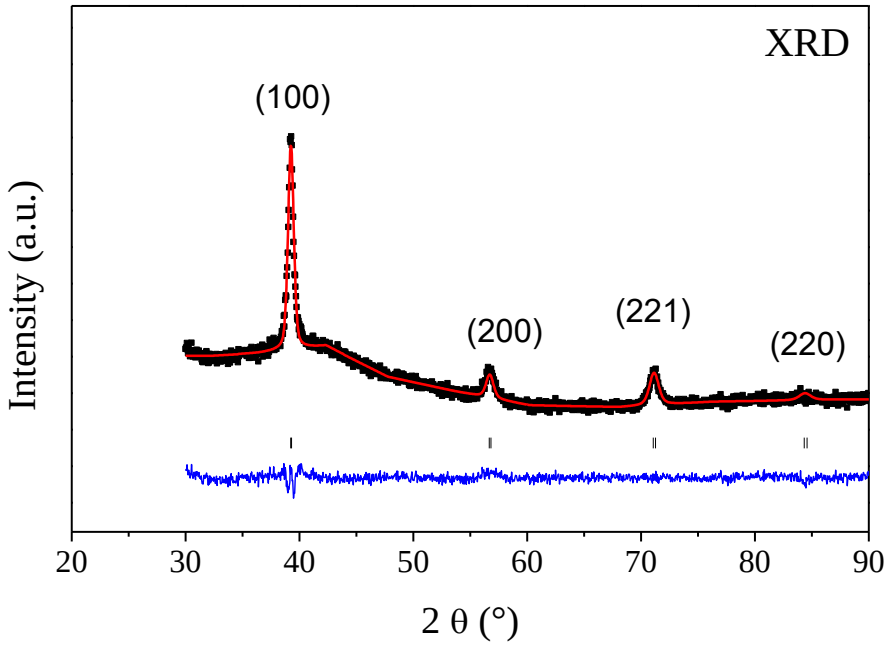

Figure 5.8. XRD of the desorbed $Ti_{0.30}V_{0.25}Zr_{0.10}Nb_{0.25}Al_{0.10}$ and corresponding Rietveld refinement with bcc structure (Im-3m) and lattice parameter a_{bcc}= 3.246(1) Å. The observed data (experimental) is represented in black dots and the red line corresponds to the calculated data; the difference between the observed and calculated profiles is represented in blue.

This result confirms the reversibility of the structure upon hydrogen absorption and desorption. The conditions for hydrogen desorption were established following the same conditions as the previous alloys, a minimum temperature of 400 °C under dynamic vacuum (10^{-5} mbar).

4.5 *Hydrogen absorption/desorption cycling*

Next, the hydrogen-cycling properties were measured with the help of a Sievert's device to evaluate the amount of hydrogen absorbed in each cycle in terms of H/*M* and wt.%. The absorption conditions consisted of a single dose of H_2 with a final equilibrium pressure of 25 bar at 25 °C, and the hydrogen desorption was carried out by heating the sample to 400 °C for 10 hours under dynamic vacuum (10^{-5} mbar). The results of the hydrogen-cycling are plotted in Figure 5.9.

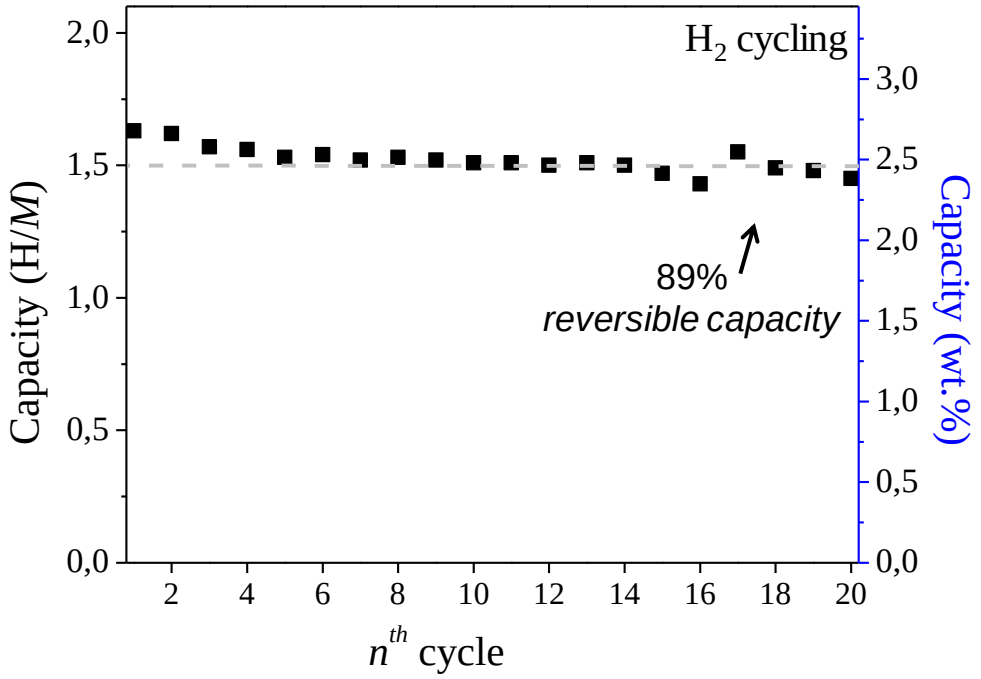

Figure 5.9. Evaluation of the hydrogen capacity of $Ti_{0.30}V_{0.25}Zr_{0.10}Nb_{0.25}Al_{0.10}$ in terms of H/M and wt.% as a function of the number of hydrogen absorption and desorption cycles.

The storage capacity of the alloy slightly fades during the first 10 cycles and subsequently reaches stabilization at around 1.5 H/*M* (2.5 wt.%). The Al-containing alloy showed a more stable storage capacity upon cycling, as compared to the quaternary alloy, and has a reversible storage capacity of 89% up to 20 hydrogenation cycles.

Structural, chemical, and thermo-desorption characterization after hydrogen-cycling

The cycled alloy was submitted to diverse characterization techniques to study the effect of hydrogen-cycling on the material microstructure and hydrogen sorption properties by comparing the results from the initial as-cast alloy and first hydride with 1.6 H/*M*.

First, the crystalline structures of the desorbed and hydride phases of the 20th cycle were characterized by XRD and the results are plotted in Figure 5.10 along with their initial counterparts.

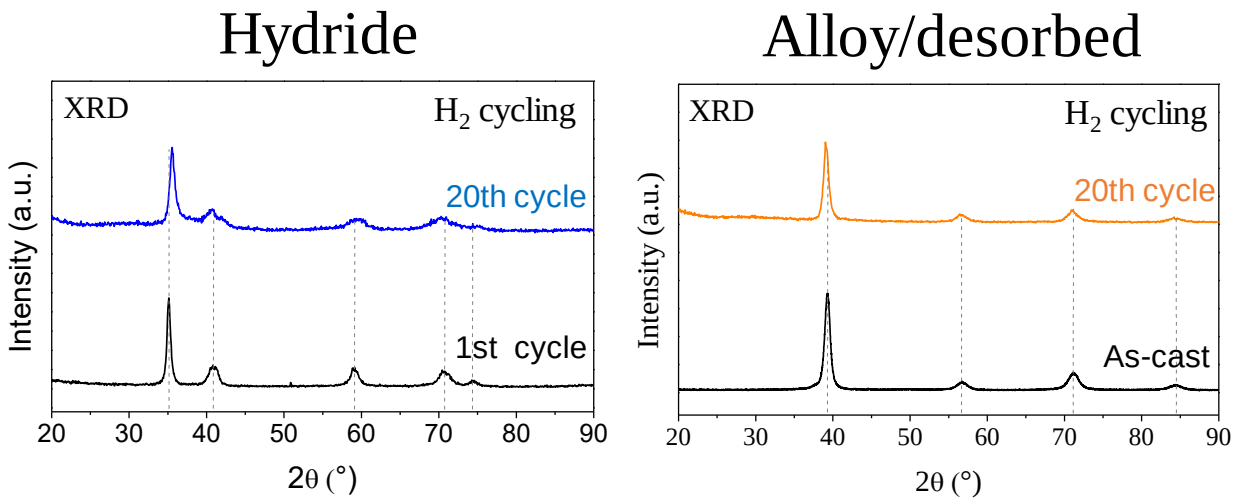

Figure 5.10. XRD patterns $Ti_{0.30}V_{0.25}Zr_{0.10}Nb_{0.25}Al_{0.10}$ before and after hydrogen-cycling. Left: hydride phases. Right: as-cast and desorbed phases.

Both, the hydride (*left*) and the desorbed phase (*right*), maintained the *bct* and *bcc* structures with lattice parameters a_{bct}= 3.197(1) and c_{bct}= 4.368(1) Å, and a_{bcc}= 3.244(1) Å, respectively. In comparison, the initial hydride (first cycle) and the as-cast alloy have similar lattice parameters a_{bct}= 3.137(1) and c_{bct}= 4.374(1) Å, and a_{bcc}= 3.247(1) Å. Thus, these results prove the structural stability of the alloy upon hydrogen-cycling. Moreover, both phases have retained a good degree of crystallinity after cycling, better than the quaternary alloy. This, further support the hypothesis that the loss of hydrogen capacity is related to the material's crystallinity. The quaternary alloy had a reversible storage capacity of 82% whereas the Al-quinary performs better (89%). Further evidence of the *bct* structure for the Al-quinary hydride, can be observed in the XRD pattern of the cycled hydride (*blue* line), where the two independent diffraction peaks at around 40° in 2θ become more apparent.

Next, SEM and EDS characterizations were carried out for the hydride phase in the 1st and 20th hydrogenation cycle, with 1.6 and 1.5 H/*M* respectively. A representative section of the samples is displayed in the BSE images in Figure 5.11.

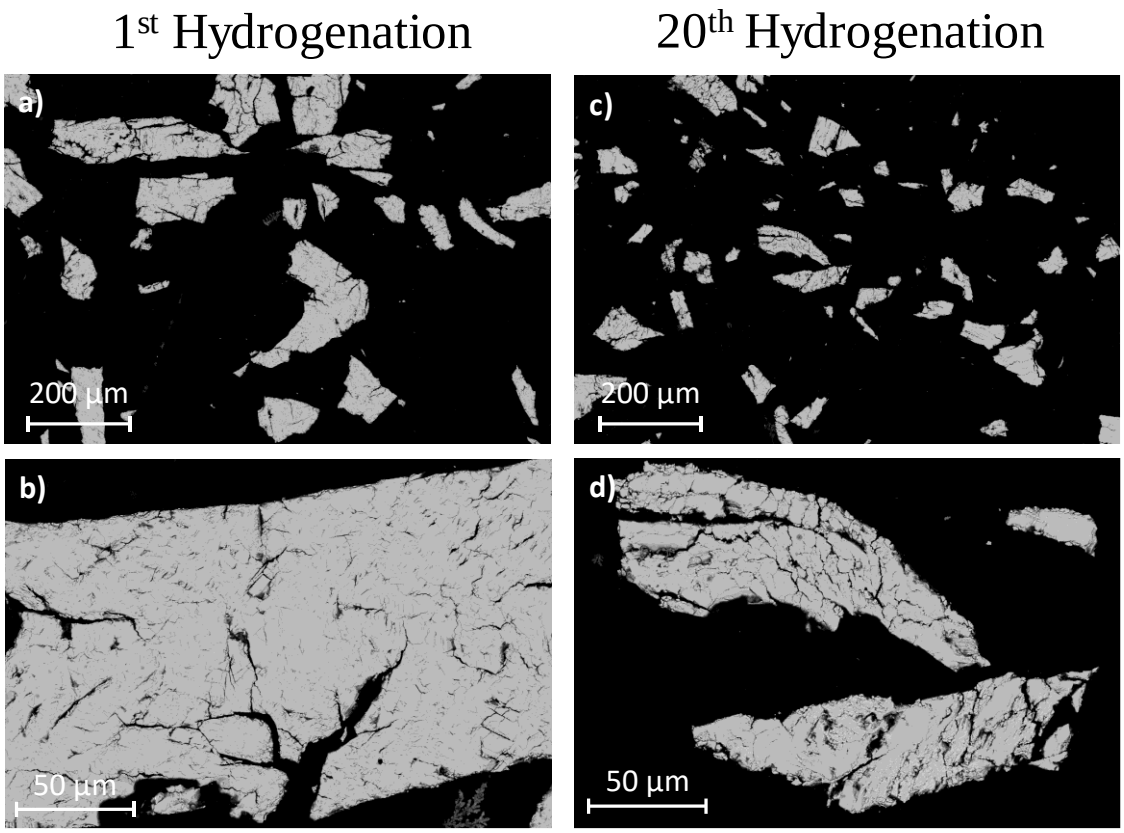

Figure 5.11. BSE images of $Ti_{0.30}V_{0.25}Zr_{0.10}Nb_{0.25}Al_{0.10}H_x$ in the 1st (a and b) and the 20th (c and d) hydrogenation cycle.

The BSE electron images show a homogeneous phase throughout the material in the first and after 20 hydrogenation cycles. The number of cracks and fissures has increased for the cycled hydride (*c* and *d*) and this is consisting due to hydrogen-embrittlement over cycling.

Next, a chemical analysis was performed on both samples to check the element distribution and chemical composition of the microstructure before and after cycling. The images from the chemical mapping are presented in Figure 5.12 and 5.13 for the 1st and 20th cycle, respectively, and the results from the chemical analysis, listing the atomic concentration of each element, are compiled in Table 5.1 and Table 5.2, respectively.

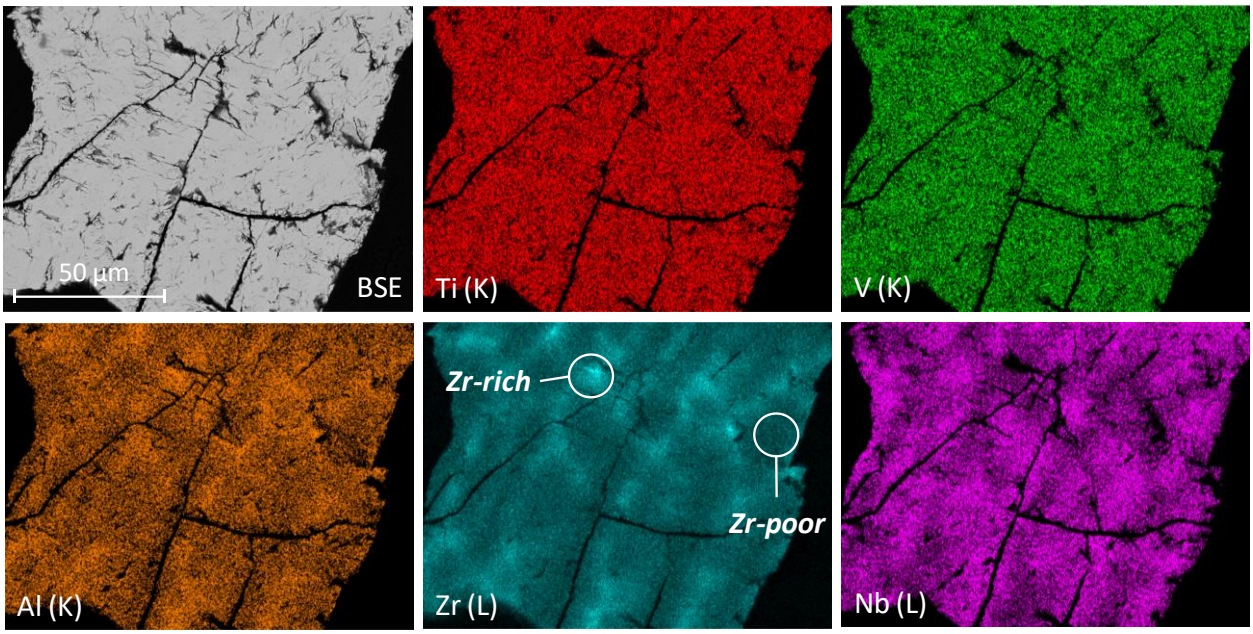

Figure 5.12. EDS chemical mapping of $Ti_{0.30}V_{0.25}Zr_{0.10}Nb_{0.25}Al_{0.10}$ in the 1st hydrogenation cycle (1.6 H/M).

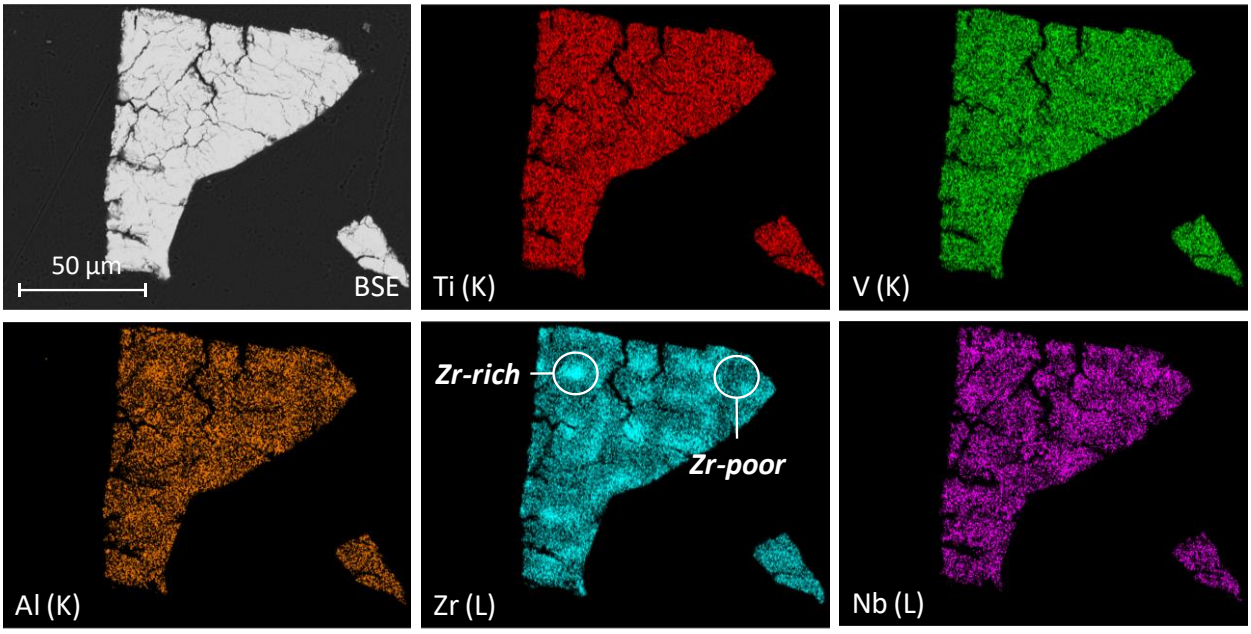

Figure 5.13. EDS chemical mapping of $Ti_{0.30}V_{0.25}Zr_{0.10}Nb_{0.25}Al_{0.10}$ in the 20th hydrogenation cycle (1.5 H/M).

The EDS analyses show the presence of two phases revealed by the contrast in color and concentration of each element, particularly from the element distribution of Zr (*cyan*). These phases are distinguished by Zr-rich and Zr-poor areas, indicated in the figures above. Similar to what was

observed for the quaternary and Ta-quinary alloys, the Nb distribution shows a richer concentration in the areas where Zr has lower content and vice versa. On the other hand, Al, Ti, and V, are homogeneously distributed throughout the phase.

Table 5.1. Atomic composition (EDS) of the different phases in the alloy $Ti_{0.30}V_{0.25}Zr_{0.10}Nb_{0.25}Al_{0.10}$ from the 1st hydrogenation cycle (1.6 H/M).

	Element	Al	Ti	V	Zr	Nb
Zr-poor	Average, at%	9.2	29.8	24.7	8.3	28.0
	Standard deviation	0.4	0.6	0.7	0.6	0.5
Zr-rich	Average, at%	12.1	28.7	22.6	17.5	19.1
	Standard deviation	0.6	0.9	1.2	2.5	1.6
Overall mapping composition, at%		10.0	29.5	24.6	10.8	25.1

Table 5.2. Atomic composition (EDS) of the different phases in the alloy $Ti_{0.30}V_{0.25}Zr_{0.10}Nb_{0.25}Al_{0.10}$ from the 20th hydrogenation cycle (1.5 H/M).

	Element	Al	Ti	V	Zr	Nb
Zr-poor	Average, at%	8.9	29.3	24.6	8.5	28.7
	Standard deviation	0.3	0.3	0.8	0.2	0.6
Zr-rich	Average, at%	10.9	28.0	24.0	15.6	21.5
	Standard deviation	0.2	1.5	1.4	2.9	1.5
Overall mapping composition, at%		9.5	28.9	24.6	11.2	25.9

From the chemical analyses, it is noticed that the element concentrations of both phases are close to the nominal composition $Al_{0.10}Ti_{0.30}V_{0.25}Zr_{0.10}Nb_{0.25}$, with a small deviation for Al, Ti and V (~1-2 at% difference), whereas Zr and Nb have a larger deviation of 6 and 4 at%, respectively. Nevertheless, the sample shows good chemical homogeneity in both samples and there is no evidence of phase decomposition or segregation after 20 hydrogenation cycles.

Finally, the cycled hydride was submitted to TDS characterization and the normalized curve is plotted in Figure 5.14 along with the TDS measurement from the first hydride, under the same experimental conditions.

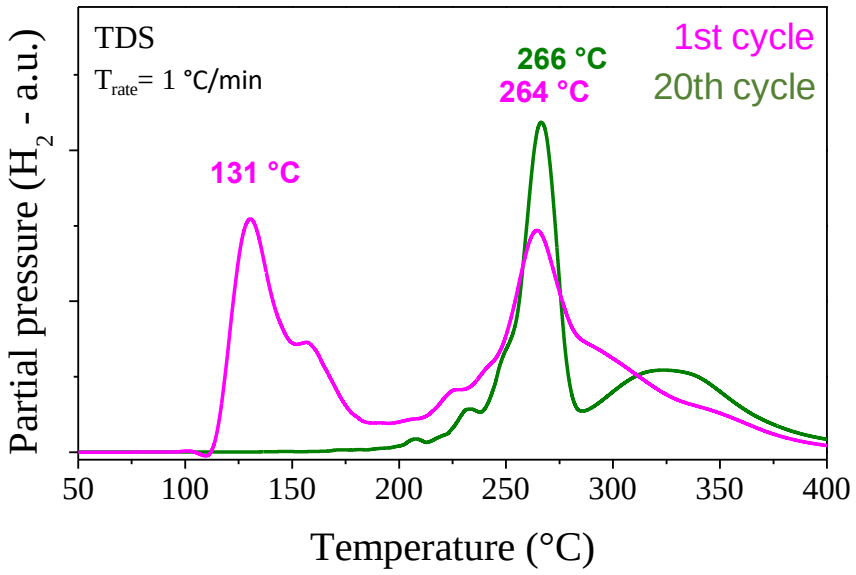

Figure 5.14. Normalized TDS curves of $Ti_{0.30}V_{0.25}Zr_{0.10}Nb_{0.25}Al_{0.10}H_x$ in the 1st and 20th hydrogenation cycle, under a constant heating rate of 1 °C/min.

The TDS curve of the cycled alloy (*green*) reveals a main desorption event at around 266 °C and a minor desorption tail at around 325 °C. Interestingly, the desorption peak at 131 °C from the 1st hydride (*magenta*) is not observed for the cycled alloy. This was also observed for the Ta-quinary alloy, and it was suggested that the disappearance of the first desorption peak may be related to the capacity loss during hydrogen-cycling.

In summary, the Al-quinary alloy was able to withstand hydrogen-cycling maintaining nearly the same structural and hydrogen sorption properties. The alloy has a reversible storage capacity of 89% (1.5 H/M or 2.5 w%) up to 20 hydrogenation cycles. The alloy maintained a good degree of crystallinity in the *bcc* and *bct* structures after cycling with nearly the same lattice parameters. No phase segregation was observed from the EDS analysis and the element distribution in the microstructure was kept constant. The thermo-desorption properties of the alloy changed after cycling, showing a single desorption event in the TDS characterization, which may be related to the capacity loss of the material after cycling.

5.6 *Comparison with the quaternary alloy*

The quaternary and the Al-containing alloy, both, have crystallized in a *bcc* lattice after synthesis with similar parameters (quaternary alloy: a_{bcc}= 3.261(5); and Al-HEA: a_{bcc}= 3.247(1) Å). Interestingly, the hydride phase of the Al-quinary alloy has adopted a *bct* structure (a_{bct}= 3.137(1) Å and c_{bct}= 4.374(1) Å) instead of the *fcc* for the quaternary hydride (a_{fcc}= 4.478(1) Å).

The addition of 10% of Al, also decreased the hydrogen absorption capacity of the base composition by 0.2 H/*M*, the opposite effect to Ta-addition. The hydrogen atoms in the *bct* structure have a preferential occupation to the tetrahedral sites. The thermo-desorption profile of the Al-containing hydride showed two desorption events separated by a temperature of ~90 °C, whereas the quaternary alloy only had a single desorption peak. The onset temperature of the Al-containing alloy, ~110 °C, is significantly lower than that of the base compositions, ~275 °C

The Al-containing alloy showed a reversible storage capacity of 89% (2.4 wt.%) after 20 hydrogenation cycles, a better result when compared to the 82% (2.3 wt.%) of the quaternary alloy. Moreover, the Al-containing alloy showed superior capabilities to withstand hydrogen-cycling, maintaining a higher degree of crystallinity than that of the base alloy, which could explain the superior reversible capacity of the alloy.

Bibliography

[1] Y. F. Ye, Q. Wang, J. Lu, C. T. Liu, and Y. Yang, "High-entropy alloy: challenges and prospects," *Materials Today*, vol. 19, no. 6, pp. 349–362, Jul. 2016, doi: 10.1016/j.mattod.2015.11.026.

[2] Gordon Aylward and Tristan Findlay, "SI Chemical Data, 3rd edition," *J. Chem. Educ.*, vol. 72, no. 5, p. A109, May 1995, doi: 10.1021/ed072pA109.1.

[3] Ch. Lexcellent and G. Gondor, "Analysis of hydride formation for hydrogen storage: Pressure–composition isotherm curves modeling," *Intermetallics*, vol. 15, no. 7, pp. 934–944, Jul. 2007, doi: 10.1016/j.intermet.2006.11.002.

CHAPTER VI

~ Ti-V-Zr-Nb-Mg ~

CHAPTER 6: Ti-V-Zr-Nb-Mg

The last of the HEAs evaluated in this manuscript is the Mg-containing composition $Ti_{0.30}$ $V_{0.25}$ $Zr_{0.10}$ $Nb_{0.25}Mg_{0.10}$. Magnesium is an alkaline-earth metal, lightweight, and widely studied for its hydrogen sorption properties, in its pure form Mg has a maximum storage capacity of 7.6 wt.%[1]. This composition has a calculated lattice distortion of 6.6%[2], [3], the highest among all the previous compositions.

6.1 Synthesis of Ti-V-Zr-Nb-Mg

Due to the low melting temperatures (~650 °C) and high vapor pressure of Mg, the synthesis of the HEA containing Mg cannot be carried out by a high-temperature fusion technique like HT-AM. Thus, ArBM was implemented for the synthesis of the Mg-quinary alloy, as discussed in the *Preliminary Results* section. The Mg-quinary alloy was successfully synthesized in a single phase after 2 hours of ball milling time, yielding an alloy in powder form with small particle size (µm range). The results of the structural characterization by XRD are shown in Figure 6.1.

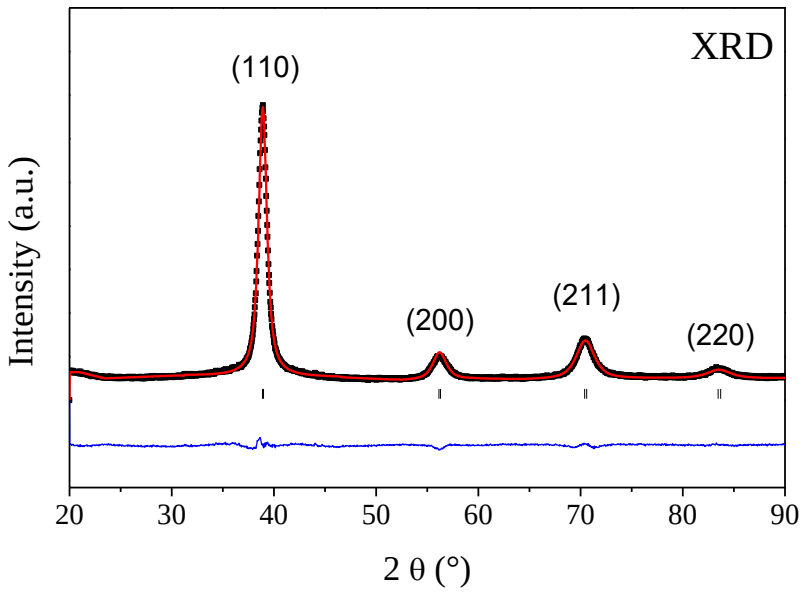

Figure 6.1. XRD of $Ti_{0.30}V_{0.25}Zr_{0.10}Nb_{0.25}Mg_{0.10}$ and corresponding Rietveld refinement with bcc structure (Im-3m) and lattice parameter a_{bcc}= 3.273(1) Å. The observed data (experimental) is represented in black dots and the red line corresponds to the calculated data; the difference between the observed and calculated profiles is represented in blue.

The pristine Mg-quinary alloy crystallizes in a single *bcc* structure (*Im-3m* space group) with a lattice parameter a_{bcc}= 3.273(1) Å, slightly larger than the quaternary alloy a_{bcc}= 3.261(1) Å. This can be understood as the atomic size of Mg (1.60 Å)[3] is significantly larger than most of the elements in the composition. Also, because of the same reason, the Mg-quinary alloy has a larger lattice distortion than the quaternary alloy, 6.6% and 6.0%. After the synthesis, the ball-milled alloy was stored inside an Ar glovebox to prevent surface oxidation.

6.2 Hydrogenation of Ti-V-Zr-Nb-Mg

For the hydrogenation of the Mg-containing alloy, the sample was loaded into a stainless steel cell and sealed under Ar atmosphere, and subsequently connected to the Sievert's device to minimize air exposure. The sample was then activated by heat treatment at 340 °C for 2 hours under dynamic vacuum. First, the alloy was exposed to a single dose of H_2 with a final equilibrium pressure of ~25 bar at 25 °C. Figure 6.2 *left* shows the absorption kinetics for the first hydrogenation. Afterward, the alloy was desorbed at 400 °C for 10 hours under dynamic vacuum and re-hydrogenated, this time, measuring a PCI at 25 °C (Figure 6.2 *right*)

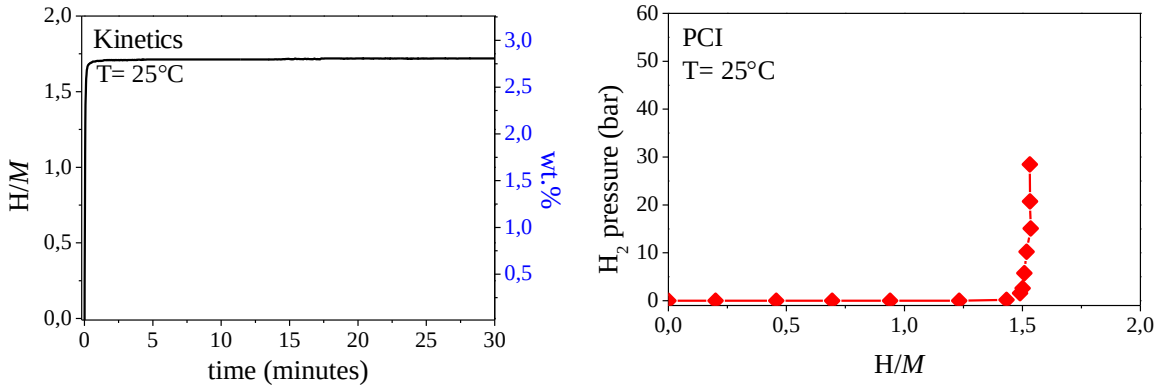

Figure 6.2. Kinetics of absorption at 25 °C (left – first hydrogenation) and PCI measured at 25 °C (right – second hydrogenation) of $Ti_{0.30}V_{0.25}Zr_{0.10}Nb_{0.25}Mg_{0.10}$.

The ball-milled sample rapidly absorbed hydrogen at room temperature, reaching a maximum capacity of 1.7 H/*M*, or 2.8 wt.%, within a few seconds. The Mg-quinary alloy showed a superior hydrogen capacity in terms of wt.% than the quaternary alloy, 2.7 wt.% (1.8 H/*M*), meaning that the addition of 10 at% Mg improved the storage capacity by reducing the weight of the HEA. The PCI

curve measured at room temperature shows a single plateau at low equilibrium pressure, below 10^{-2} bar, this time reaching a maximum capacity of 1.5 H/*M* for the second hydrogenation.

In the *preliminary results* section, the ball-milled quaternary alloy showed poor kinetics of absorption at room temperature that was explained as a consequence of surface oxidation. This time, the ball-milled sample was not exposed to air and rapidly absorbed hydrogen at room temperature, reaching equilibrium within just a few minutes.

The crystalline structure of the hydride phase, at the maximum hydrogen capacity (1.7 H/*M*), was characterized by SR-XRD at the synchrotron facility in SOLEIL, France. Figure 6.3 shows the Rietveld refinement of the diffraction pattern with a *fcc* structure. Broad diffraction signals are observed for the Mg-containing alloy due to the extensive grinding in ball-milled samples, which refines the crystallite size and introduced more strain into the structure[4].

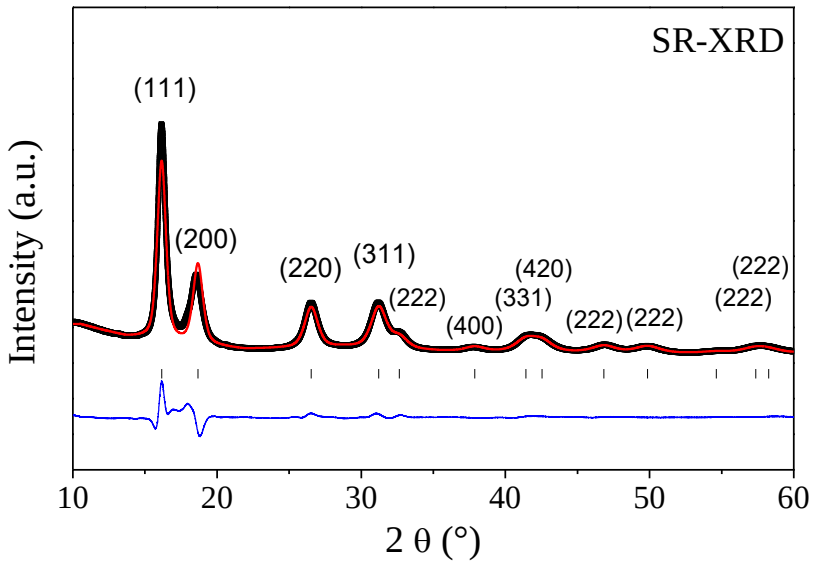

Figure 6.3. SR-XRD of the $Ti_{0.30}V_{0.25}Zr_{0.10}Nb_{0.25}Mg_{0.10}H_{1.7}$ hydride and corresponding Rietveld analysis with a fcc structure (Fm-3m) and lattice parameter a_{fcc}= 4.492(1) Å. The observed data (experimental) is represented in black dots and the red line corresponds to the calculated data; the difference between the observed and calculated profiles is represented in blue.

As it was the case for the quaternary and Ta-quinary alloy, the refinement of the diffraction pattern can be similarly fitted by using either a *fcc* or a *bct* structure, with close confidence factors (χ^2_{fcc}= 62.1 and χ^2_{bct}= 68.8). Due to the impossibility to reliable discriminate between these, the simplest structure will be privileged for the hydride phase. Thus, it is assumed that the Mg-quinary hydride adopts the *fcc* structure with lattice parameter a_{fcc}= 4.492(1) Å.

In summary, the ball-milled quinary alloy $Ti_{0.30}V_{0.25}Zr_{0.10}Nb_{0.25}Mg_{0.10}$ can rapidly absorb hydrogen at room temperature, with a maximum storage capacity of 1.7 H/*M* (2.8 wt.%), and undergoes a phase transformation from a *bcc* alloy to a *fcc* hydride.

6.3 *In-situ* neutron diffraction

Next, nD experiments were performed on a deuteride sample (1.7 D/*M*) at the ILL neutron facility in Grenoble, France. First, the diffraction pattern was measured *ex-situ* by loading the sample into a vanadium can to collect the diffraction data at 25 °C. The results of nD are plotted in Figure 6.4 along with the structural refinement with a *fcc* structure.

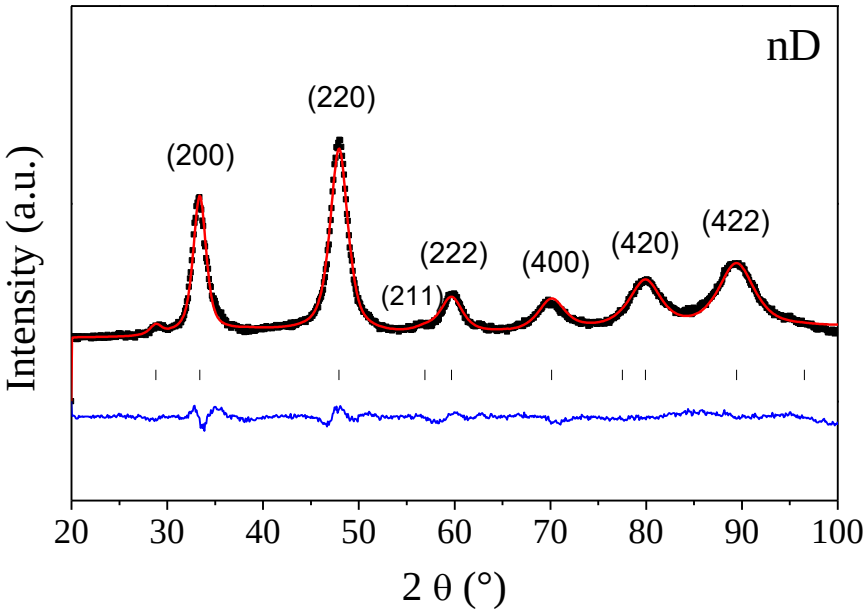

Figure 6.4. nD of the $Ti_{0.30}V_{0.25}Zr_{0.10}Nb_{0.25}Mg_{0.10}D_{1.7}$ and corresponding Rietveld analysis with a fcc structure (Fm-3m) and lattice parameter a_{fcc}= 4.479(1) Å. The observed data (experimental) is represented in black dots and the red line corresponds to the calculated data; the difference between the observed and calculated profiles is represented in blue.

The nD of the deuteride phase also reveals the broadening of the diffraction peaks characteristic of ball-milled samples. The Rietveld refinement with a *fcc* structure shows a good fitting of the nD profile with a lattice parameter a_{fcc}= 4.479(1) Å, and the deuterium atoms were located in the tetrahedral interstitial sites of the *fcc* structure.

Next, *in-situ* neutron diffraction was performed during thermo-desorption by heating the sample at a constant heating rate of 1 °C/min while evacuating under dynamic vacuum (10^{-5} mbar). The thermo-diffractogram is plotted in Figure 6.5 along with the pressure readings on the right.

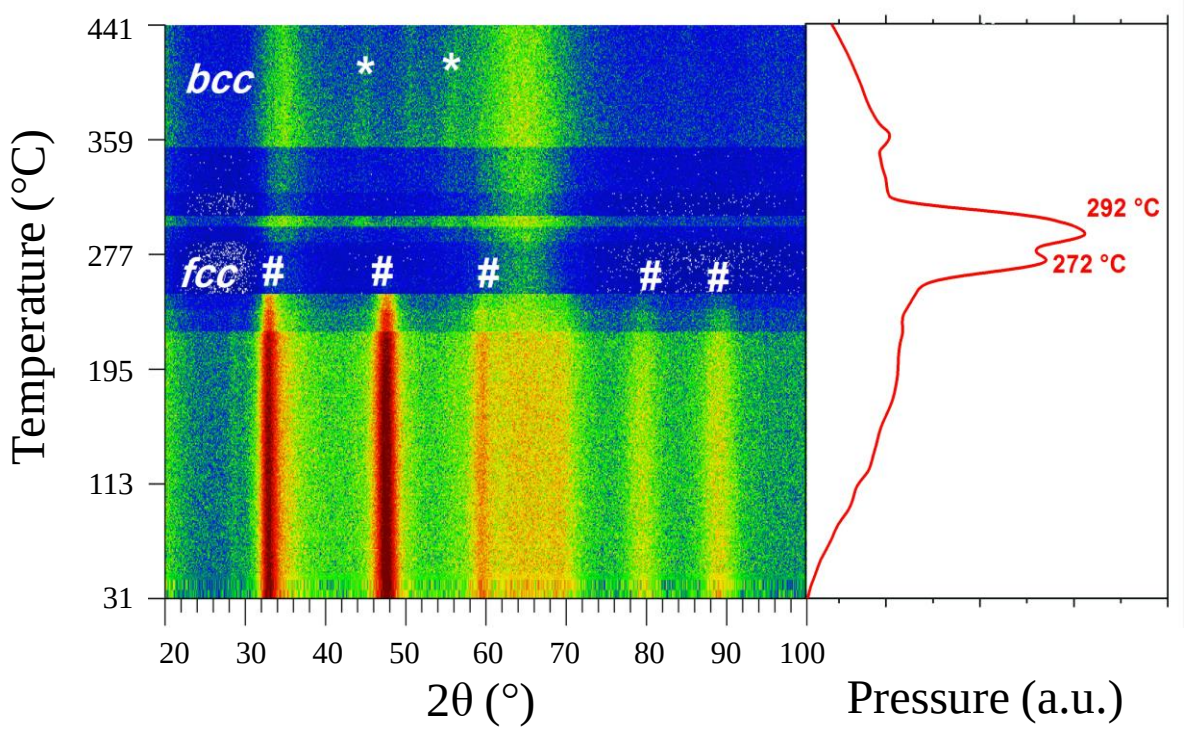

Figure 6.5. In-situ neutron diffraction of $Ti_{0.30}V_{0.25}Zr_{0.10}Nb_{0.25}Mg_{0.10}D_{1.7}$ heated at a constant temperature rate of 1 °C/min and the vacuum pressure readings during deuterium desorption.

The diffraction signals of the *fcc* hydride are marked with the hash symbol (#) and the broad signals at around 32-36° and 60-70°, in 2θ, correspond to the silica tube used as the sample holder. Starting from the bottom, the *fcc* phase seems stable up to ~240 °C, where a sudden disruption of the neutron signal occurs. The intensity of the *fcc* phase decreases smoothly with increasing temperature. This is linked to the desorption profile on the right, where hydrogen desorbs at a slow rate from ~50-240 °C. The disruption of the neutron signal, from ~240 to 350 °C, is associated with the desorption event observed in the pressure profile (~272-292 °C). After 350 °C, the diffraction signal returns and shows the diffraction peaks of the silica tube and few other low-intensity signals in between 40 and 60°. The *fcc* structure is no longer observed at high temperatures, and thus, it can be assumed that the alloy has fully desorbed deuterium after the desorption peaks. Based on the previously characterized MPEAs, the diffraction signals of the *bcc* alloy should correspond to those marked with stars (*) in the thermo-diffractogram.

This oddly-timed disruption can be explained by hydrogen desorption and the fact that the ball-milled sample is a fine powder with small and light-weight particles. When desorption begins, at the onset temperature, significant amounts of hydrogen are suddenly released from the metal, creating a gas flow that moves the particles away. To put it into context, the geometry setup of the experiment consists of a silica tube in a vertical position, connected to the vacuum rig through the upper side while the sample sits at the bottom of the tube, in the pathway of the neutron beamline. The desorbed gas flows upwards, towards the vacuum rig, levitating the fine particles and moving them out of the neutron beam, disrupting the diffraction signal. After the desorption peak, at around 350 °C, the fine powder settles down and the diffraction signals of the sample are collected once again.

In summary, the Mg-quinary hydride adopts a *fcc* structure with hydrogen occupying the tetrahedral interstitial sites, the same as the quaternary alloy. Even though the phase transitions were not properly recorded during the *in-situ* measurement, it can be assumed that the Mg-quinary alloy follows the same trend as the former MPEAs, and underwent a single-phase transformation upon hydrogen desorption from a *fcc* hydride to a *bcc* structure. This is also supported by the single desorption event with two maxima in the pressure profile.

6.4 *Thermo-desorption characterization*

The hydrogen desorption properties were characterized by TDS under a constant heating rate, 1 °C/min, and dynamic vacuum (10^{-6} mbar). The results from TDS are plotted in Figure 6.6.

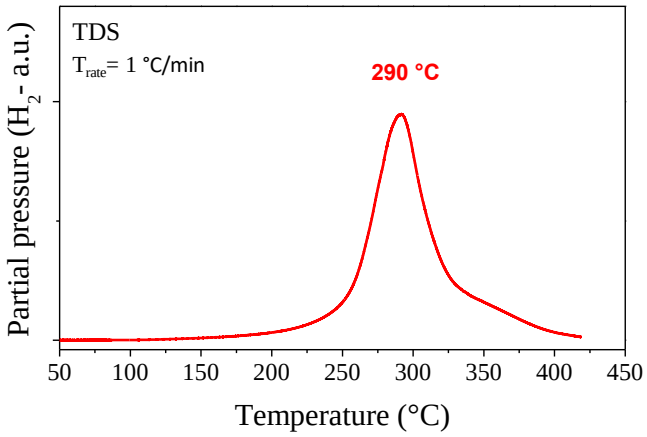

Figure 6.6. TDS curve of $Ti_{0.30}V_{0.25}Zr_{0.10}Nb_{0.25}Mg_{0.10}H_{1.7}$ upon a constant heating rate of 1 °C/min.

The TDS curve reveals a single desorption peak at ~290 °C, close to that of the quaternary alloy at ~287 °C, and is in good agreement with the *in-situ* neutron diffraction experiment. Interestingly, the addition of Mg into the base composition maintained similar desorption properties as the quaternary alloy, whereas the addition of Al and Ta destabilized the thermo-desorption properties of the hydride phase, decreasing the onset temperature and spreading the desorption process into two desorption events separated by a temperature gap of around ~90 °C.

After hydrogen desorption, the alloy was characterized by XRD and Rietveld analysis, presented in Figure 6.7. The desorbed alloy recovers the single *bcc* structure with a smaller lattice parameter than the pristine alloy (desorbed: a_{bcc}= 3.239(1) Å and, pristine: a_{bcc}= 3.273(1) Å).

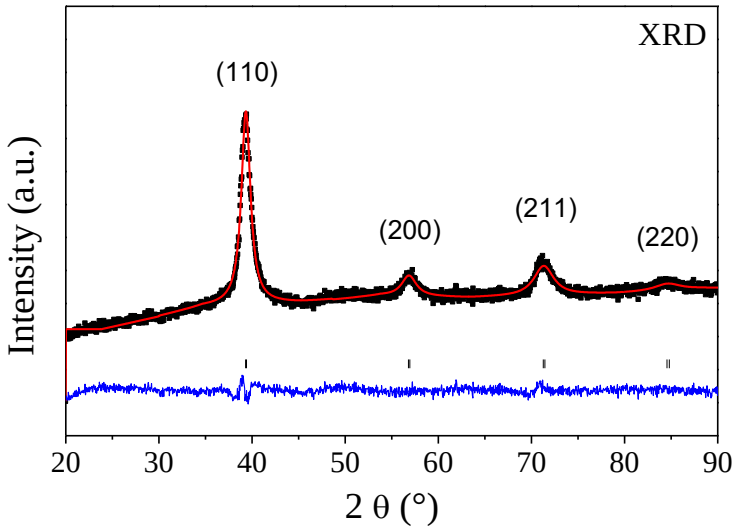

Figure 6.7. XRD of the desorbed $Ti_{0.30}V_{0.25}Zr_{0.10}Nb_{0.25}Mg_{0.10}$ and corresponding Rietveld refinement with bcc structure (Im-3m) and lattice parameter a_{bcc}= 3.239(1) Å. The observed data (experimental) is represented in black dots and the red line corresponds to the calculated data; the difference between the observed and calculated profiles is represented in blue.

6.5 *Hydrogen absorption/desorption cycling*

Then, the hydrogen-cycling properties of the Mg-quinary alloy were evaluated in terms of capacity expressed as H/*M* and wt.%. For hydrogen absorption, the alloy was submitted to a final equilibrium pressure of 25 bar at 25 °C (thermostated in a water bath), and for hydrogen desorption, the sample was heated up to 400 °C and kept constant for 10 hours under dynamic vacuum (10^{-5} mbar). The Mg-quinary alloy was cycled up to 12 times and the results are plotted in Figure 6.8.

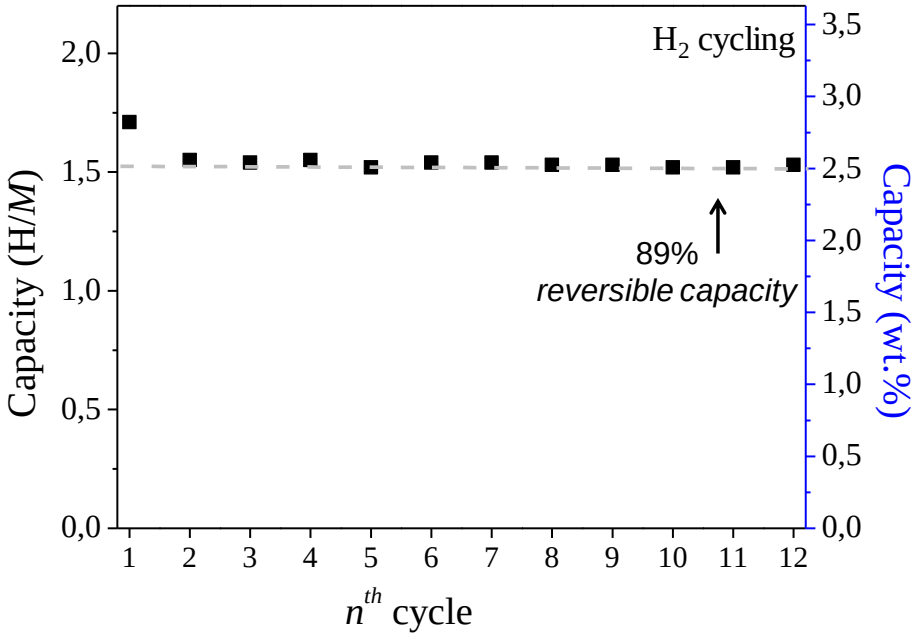

Figure 6.8. Evaluation of the hydrogen capacity of $Ti_{0.30}V_{0.25}Zr_{0.10}Nb_{0.25}Mg_{0.10}$ in terms of H/M and wt.% as a function of the number of hydrogen absorption and desorption cycles.

The Mg-quinary alloy reaches a stable reversible capacity only after the second hydrogenation cycle, whereas the quaternary, and the other quinary alloys, had a fading capacity of maximum 10 hydrogenation cycles. The reversible storage capacity of the Mg-containing alloy is 1.5 H/*M*, or 2.5 wt.%, which is 89% of its initial capacity. In comparison, the quaternary alloy had a reversible capacity of 1.5 H/*M*, or 2.3 wt.%, equivalent to 82% of its maximum capacity.

Structural, chemical, and thermo-desorption characterization after hydrogen-cycling

The cycled alloy was submitted to diverse characterization techniques to study the effect of hydrogen-cycling on the material microstructure and hydrogen sorption properties by comparing the results from the initial pristine alloy and first hydride.

First, the desorbed and hydride phases at the 12th hydrogenation cycles were characterized by XRD and the results are plotted in Figure 6.9 along with their initial counterparts.

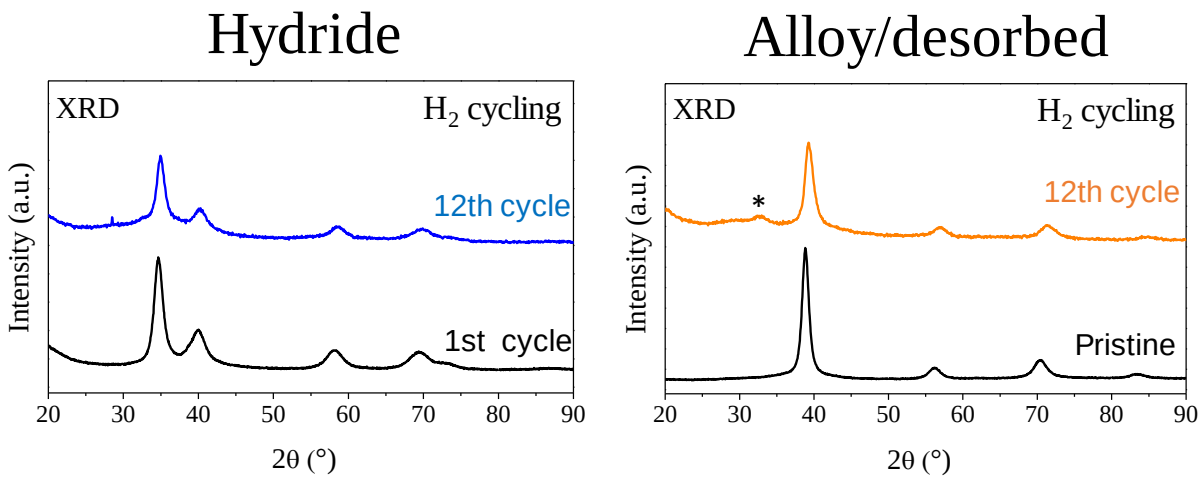

Figure 6.9. XRD patterns $Ti_{0.30}V_{0.25}Zr_{0.10}Nb_{0.25}Mg_{0.10}$ before and after hydrogen-cycling. Left: hydride phases. Right: pristine and desorbed phases.

Both, the hydride (*left*) and desorbed phases (*right*) maintained the same crystal structure after 12 hydrogenation cycles. From the XRD, a displacement of the diffraction peaks to a higher 2θ is noticed for the desorbed phase, which is an indication of a smaller lattice constant. The calculated lattice parameters for the cycled alloy are: a_{bcc}= 3.231(1) Å and a_{fcc}= 4.498(1) Å; and for the initial alloy and hydride phases: a_{bcc}= 3.273(1) Å and a_{fcc}= 4.492(1) Å, respectively. A small diffraction contribution (marked with a star) can be observed at ~33°, in 2θ, for the desorbed phase (*orange – right*). The source of this diffraction peak is unknown and may arise from a segregated phase or contamination introduced during sample manipulation. The chemical analysis in the next section may help to identify the nature of this impurity.

Next, EDS characterization was performed on the hydride phase in the 1st and 12th hydrogenation cycle, 1.7 and 1.5 H/*M* respectively. A chemical mapping was performed on both samples to check the element distribution and chemical composition of the microstructure. The images from the chemical analysis are presented in Figure 6.10 and 6.11 for the 1st and 12th cycle, respectively, and the atomic concentrations of each element are listed in Table 6.1 and Table 6.2. The atomic concentrations were quantified using the Ti (K), V (K), Zr (L), Nb (L), and Mg (K) lines from the photon emission of core-electrons.

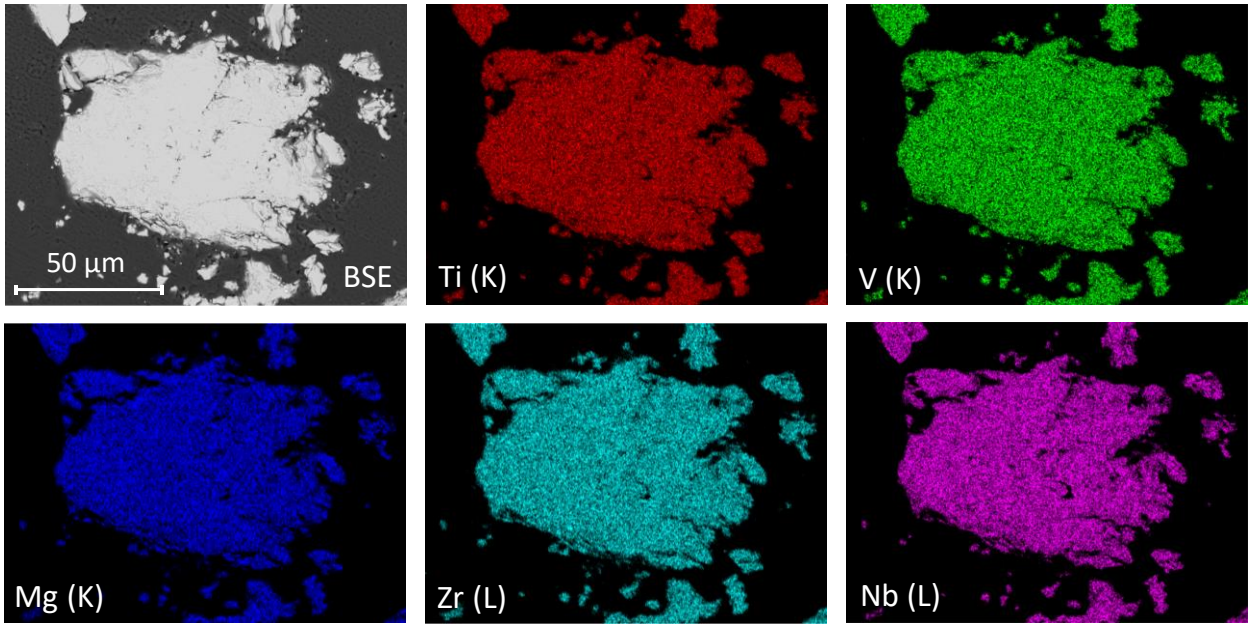

Figure 6.10. EDS chemical mapping of $Ti_{0.30}V_{0.25}Zr_{0.10}Nb_{0.25}Mg_{0.10}$ in the 1st hydrogenation cycle (1.7 H/M).

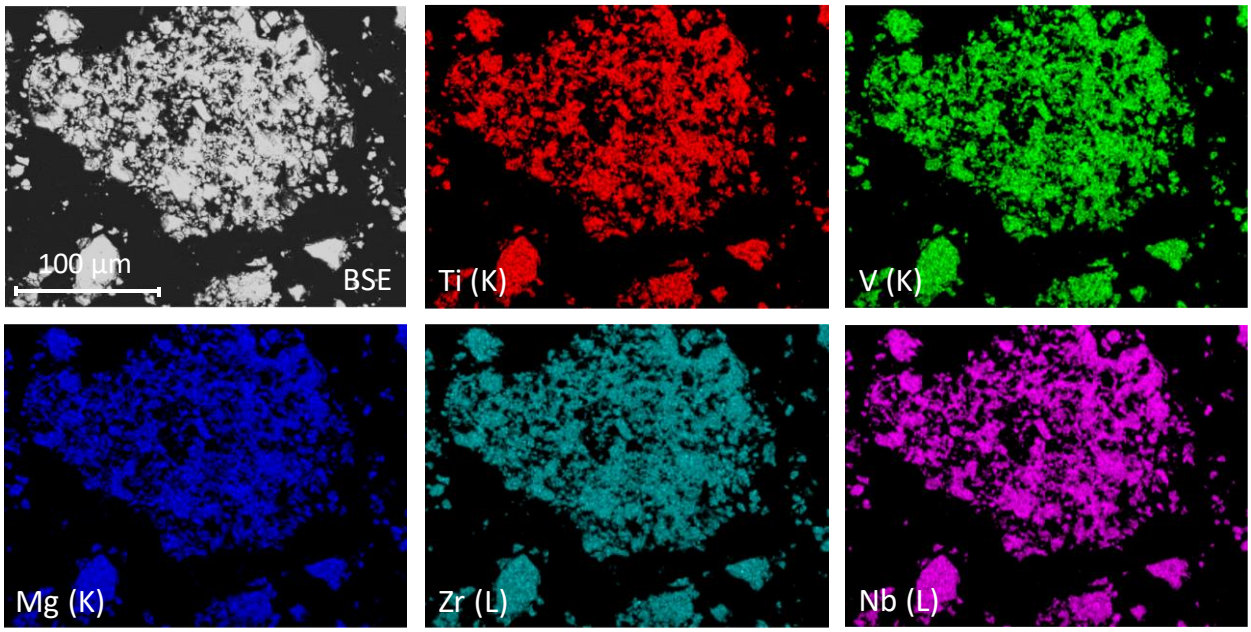

Figure 6.11. EDS chemical mapping of $Ti_{0.30}V_{0.25}Zr_{0.10}Nb_{0.25}Mg_{0.10}$ in the 12th hydrogenation cycle (1.5 H/M).

The chemical mapping reveals a homogenous distribution of the elements throughout the microstructure, and no secondary phases can be observed as it was the case of the HT-AM samples. The cycled alloy shows a refined microstructure consequence of hydrogen embrittlement, but it

maintains a good chemical homogeneity as the first hydride. There is no evidence of a segregated phase that can explain the diffraction peak (*) observed in XRD, thus it is more likely that this is contamination introduced before the hydrogen-cycling experiments.

Table 6.1. Chemical analysis (EDS) of the different phases in the alloy $Ti_{0.30}V_{0.25}Zr_{0.10}Nb_{0.25}Mg_{0.10}$ from the 1st hydrogenation cycle (1.7 H/M).

Element	Ti	V	Zr	Nb	Mg
Average, %	29.3	24.7	10.2	26.1	9.7
Standard deviation	0.4	0.4	0.1	0.3	0.2

Table 6.1. Chemical analysis (EDS) of the different phases in the alloy $Ti_{0.30}V_{0.25}Zr_{0.10}Nb_{0.25}Mg_{0.10}$ from the 12th hydrogenation cycle (1.5 H/M).

Element	Ti	V	Zr	Nb	Mg
Average, %	29.3	24.6	10.3	26.4	9.4
Standard deviation	0.5	0.5	0.3	0.2	0.5

The atomic concentrations of the microstructure are near the nominal values with minimal variation of ~1.0 at% for both samples, confirming that the chemical structure of Mg-quinary alloy can withstand hydrogen-cycling for at least 12 hydrogenation cycles without phase segregation or decomposition.

Lastly, a TDS measurement was performed on the hydride phase after 12 hydrogenation cycles (1.5 H/*M*) under the same experimental conditions as before. The TDS results are plotted in Figure 6.12 along with the TDS cure from the first hydride (1.7 H/*M*).

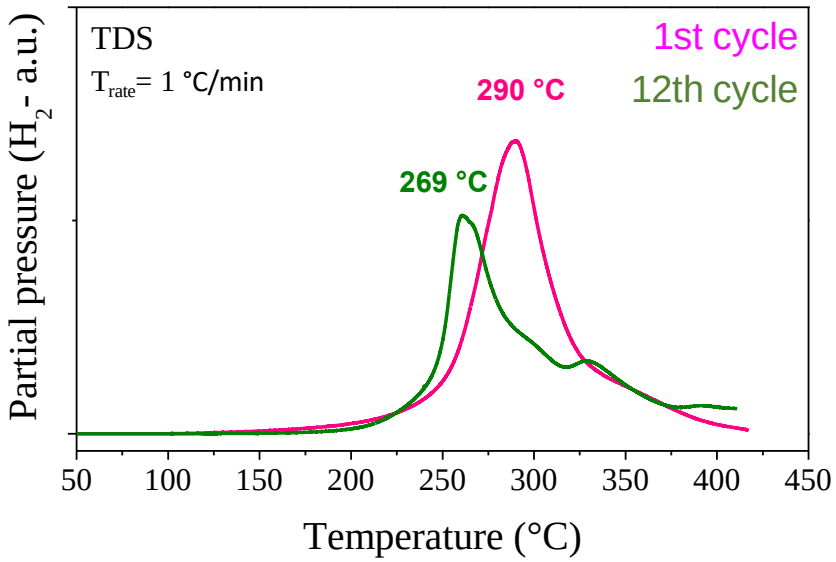

Figure 6.1. Normalized TDS curves of $Ti_{0.30}V_{0.25}Zr_{0.10}Nb_{0.25}Mg_{0.10}H_x$ in the 1st and 12th hydrogenation cycle, under a constant heating rate of 1 °C/min.

The thermo-desorption profile of the cycled hydride is very similar to that of the initial phase, with a temperature of maximum desorption rate at 269 °C and nearly the same onset temperature ~250 °C. This behavior was similarly observed for the quaternary alloy.

In summary, the Mg-containing alloy showed interesting hydrogen-cycling properties, which can reversibly store up to 1.5 H/*M* (2.5 wt.%) for more than 12 hydrogenation cycles. The crystalline structure and chemical composition of the alloy were retained after hydrogen-cycling, as characterized by XRD and EDS analyses. The thermo-desorption properties of the alloy were also maintained constant after cycling.

6.6 *Comparison with the quaternary alloy*

The Mg-containing alloy was successfully synthesized by ArBM crystallizing in a *bcc* structure (a_{bcc}= 3.273(1) Å), similar to the quaternary alloy prepared by HT-AM (a_{bcc}= 3.261(1) Å). Both alloys undergo the same phase transition from a *bcc* alloy to a *fcc* structure upon hydrogen absorption, with lattice parameters a_{fcc}= 4.478(1) Å and a_{fcc}= 4.492(1) Å, for the quaternary and Mg-quinary alloy respectively.

The hydrogen sorption properties of the Mg-containing alloy are similar to those of the base composition, taking into consideration that the alloys were prepared using different techniques (ArBM and HT-AM). The maximum capacity of the Mg-quinary alloy is 1.7 H/*M* (2.8 wt.%), whereas the quaternary alloy has a maximum uptake of 1.8 H/*M* (2.7 wt.%). This difference cannot be entirely accounted to the addition of Mg (10 at%), but also it might be a consequence of the synthetic method employed. As demonstrated in the *preliminary results* section, the ball-milled quaternary alloy had a slightly lower hydrogen capacity than the arc-melted sample of the same alloy. The temperatures for hydrogen desorption in both alloys are also very similar, with an onset temperature at around ~250 °C.

The hydrogen-cycling properties of the Mg-quinary alloy are superior to those of the quaternary, even for a ball-milled alloy, showing a reversible storage capacity of 89% and 82% of their initial capacity, respectively. The structural and chemical properties of both alloys were maintained after several hydrogenation cycles and neither of both suffered from hydrogen-induced decomposition.

Bibliography

[1] L. Ouyang *et al.*, "Magnesium-based hydrogen storage compounds: A review," *Journal of Alloys and Compounds*, vol. 832, p. 154865, Aug. 2020, doi: 10.1016/j.jallcom.2020.154865.

[2] Y. F. Ye, Q. Wang, J. Lu, C. T. Liu, and Y. Yang, "High-entropy alloy: challenges and prospects," *Materials Today*, vol. 19, no. 6, pp. 349–362, Jul. 2016, doi: 10.1016/j.mattod.2015.11.026.

[3] Gordon Aylward and Tristan Findlay, "SI Chemical Data, 3rd edition," *J. Chem. Educ.*, vol. 72, no. 5, p. A109, May 1995, doi: 10.1021/ed072pA109.1.

[4] J. Huot, D. B. Ravnsbæk, J. Zhang, F. Cuevas, M. Latroche, and T. R. Jensen, "Mechanochemical synthesis of hydrogen storage materials," *Progress in Materials Science*, vol. 58, no. 1, pp. 30–75, Jan. 2013, doi: 10.1016/j.pmatsci.2012.07.001.

Conclusions and Perspectives

The main objective of this project was to study the hydrogen sorption properties of different MPEAs based on refractory elements. In the literature, the hydrogenation properties of single-phased MPEAs are scarcely investigated and, due to the chemical diversity of multi-component alloys, it is almost impossible to find a rational trend to relate and explain the hydrogen sorption properties with the chemical composition or structural properties of the material. The main idea behind this project was to propose a new strategy for the evaluation of different MPEAs by systematically studying these alloys, minimizing the degree of freedom in these systems, and standardizing the experimental conditions for their evaluation.

This strategy entails establishing a base MPEA, composed by four refractory elements, study the structural and hydrogen sorption properties, and evaluate the effect of adding a fifth element into the mixture. Thus, four compositions have been thoroughly studied in this manuscript: Ti-V-Zr-Nb and Ti-V-Zr-Nb-*M*, where *M*= Ta, Al, and Mg.

A first study, denominated as *preliminary results*, addressed the optimization of the chemical composition of the MPEAs in order to produce single-phased systems. The optimized composition consists on the reduction of Zr-content to 10 at.%. Also, the concentration of the fifth element was maintained at 10 at% to avoid substantial changes in the structural properties. Thus the optimized composition for this study is $Ti_{0.30}$ $V_{0.25}$ $Zr_{0.10}$ $Nb_{0.25}M_{0.10}$. Additionally, the quaternary alloy was synthesized by three different synthetic methods and the hydrogenation properties were evaluated to determine the best synthetic approach. This study revealed that arc melting alloys can work under air-conditions with minor effects on the hydrogenation properties. In ball-milled alloys, the hydrogenation properties are significantly affected by surface oxidation, and must be stored and manipulated in high-purity Ar glovebox. Thus, all MPEAs in this project were synthesized by arc melting, when applicable.

The quaternary alloy Ti-V-Zr-Nb, with optimized composition, is denominated as the alloy with base properties to compare against. The quaternary alloy was successfully prepared by arc melting in a single phase with a *bcc* structure. The microstructural analysis by EDS confirms good chemical homogeneity throughout the microstructure with few regions slightly rich in Zr. The alloy has a maximum hydrogen capacity of 1.8 H/*M* (2.7 wt.%) and the resulting hydride crystallized in a single

fcc structure, as determined by SR-XRD. The quaternary alloy undergoes a single phase transformation upon hydrogen absorption (or desorption) confirmed by the PCI and *in-situ* nD experiments. The hydrogen desorption of the quaternary alloy occurs in a single step. The quaternary alloy is able to reversibly store 1.5 H/M, or 2.3 wt.% up to 20 hydrogenation cycles, and the loss of the capacity occurs within the first three cycles. The quaternary alloy showed good chemical and structural stability, maintaining a single structure without phase separation or hydrogen induced decomposition, as determined by XRD and EDS analyses.

The main results of the characterization of the quaternary and quinary alloys are listed in the table below.

	Structural properties			Storage capacity			Desorption
MPEA composition	pristine		hydride	initial	reversible capacity		TDS
	δ%[1]	a_{bcc} /Å	a_{fcc}(a, c_{bct})/Å	H/*M* (wt.%)	H/*M* (wt.%)	%	T_{onset} / °C
$Ti_{0.325}V_{0.275}Zr_{0.125}Nb_{0.275}$	6.0	3.261(1)	***fcc*** *4*.478(1)	1.8 (2.7)	1.5 (2.3)	82%	270
$Ti_{0.30}V_{0.25}Zr_{0.10}Nb_{0.25}$**Ta**$_{0.10}$	5.5	3.263(1)	***fcc*** 4.474(1)	2.0 (2.5)	1.8 (2.3)	86%	125
$Ti_{0.30}V_{0.25}Zr_{0.10}Nb_{0.25}$**Al**$_{0.10}$	5.5	3.247(1)	***bct*** 3.137(1) 4.374(1)	1.6 (2.6)	1.5 (2.5)	89%	110
$Ti_{0.30}V_{0.25}Zr_{0.10}Nb_{0.25}$**Mg**$_{0.10}$	6.6	3.273(1)	***fcc*** 4.492(1)	1.7 (2.8)	1.6 (2.5)	89%	260

1 Lattice distortion as described by Ye. et al. 2016
2 Reversible storage capacity in % is calculated from the H/*M* capacities
3 Onset temperature in the first hydride according to TDS measurements

The addition of Ta, Al, or Mg as the fifth element caused diverse and interesting effects on the structural and hydrogen sorption properties of the base composition. Firstly, all three quinary alloy crystallized in a single phase with the same crystalline structure as the quaternary alloy (*bcc*). The Mg-quinary alloy (ball-milled) has a homogenous microstructure with minimal chemical modulation, while the Al- and Ta-quinary alloys had few region rich in Zr, the same as the quaternary alloy. The BSE image of Ta-quinary alloy revealed a semi-dendritic microstructure with two phases: one rich in Zr, and other rich in Nb and Ta.

The addition of Ta had a positive effect on the hydrogen storage capacity, increasing the maximum capacity to 2.0 H/*M*, meanwhile, Al and Mg had the opposite effect with a maximum capacity of 1.6 and 1.7 H/*M*, respectively. There is no direct relationship of this behavior with the structural properties of the MPEAs (e.g. lattice distortion, or lattice parameters). All the resulting hydrides

are single structures and there is no evidence of phase separation after hydrogenation, as determined by XRD and EDS. Two of the quinary alloys adopted a *fcc* structure in their hydride phase, while the Al-composition adopted the *bct* structure, as determined by SR-XRD. These two structures are relatable to each other, as the *bct* structure can be described by an expansion or the *c*-axis in the *fcc* lattice. The hydrogenation of all HEAs occurred in a single-phase transformation from a pristine *bcc* alloy to a *fcc* hydride phase, the same as the quaternary alloy.

The thermo-desorption characterization of the quinary alloys revealed interesting differences with the quaternary composition. The onset temperature for hydrogen desorption was significantly decreased with the addition of Ta and Al (~130 and ~110 °C), while Mg showed almost the same desorption behavior of the quaternary alloy, ~270-275 °C.

The hydrogen-cycling properties were improved with the addition of Ta, Al, and Mg, respectively. All HEAs showed superior reversible storage capacities of 86-89%, particularly the Al- and Mg-quinary alloys, compared to the reversible capacity of the quaternary alloy, 82%. The chemical composition and the structural properties of all HEAs were maintained after hydrogen-cycling, showing the same, or similar, chemical composition and crystalline structures of the initial alloys, while cycling in single phase.

These systems, Ti-V-Zr-Nb-*M*, showed interesting results when compared to those in the literature, particularly in the cycle-life properties, as they demonstrated to withstand hydrogen-cycling without phase separation or decomposition, an issue often reported for multi-component materials. The main disadvantage of these system is the stability of the hydride phase, which requires high temperatures for hydrogen desorption. The stability of the hydride is also manifested in the PCI curves of the MPEAs in this project, with equilibrium pressures below 10^{-2} mbar. Therefore one of the main objectives for future works is to study new HEAs compositions that have less stable hydride phases.

Due to the chemical versatility of MPEAs and HEAs, this opens a wide field of opportunity to investigate and to rationalize the hydrogen sorption properties of these materials with their structural properties or chemical composition. This project can be used as a cornerstone for a systematic approach of the evaluation of the hydrogenation properties. Therefore, we propose the following perspectives:

- The properties of the MPEAs reported in this manuscript may be complemented by PCIs measurements at different temperatures to determine the thermodynamic properties of the hydrogenation reaction, and; TDS measurements at different heating rates to determine the activation energy for hydrogen desorption by the Kissinger method.
- Investigate a large number of HEAs in the form of $Ti_{0.30}V_{0.25}Zr_{0.10}Nb_{0.25}M_{0.10}$, where M can be substituted by other transitions metals, alkali, or alkaline earth metals (or almost any other elements from the periodic table) and study their hydrogenation properties by kinetics of absorption, PCI, and TDS, with intention to find a less stable hydride phase.
- Similar to the previous point, investigate more HEAs compositions, this rationalizing the fundamental properties (e.g. lattice parameters, volume expansion with hydrogen, valence electron concentration, etc.) and relate them to their hydrogen absorption and desorption properties.
- The most appealing compositions, based on the results from this project, are the Al- and Mg-quinary alloys due to the lightweight properties and their hydrogen-cycling properties, can be further investigated by varying their atomic concentration $Ti_vV_wZr_xNb_yM_z$ and study the effect of the hydrogen sorption properties in a rational approach (e.g. modulating the lattice distortion, or the influence of an element in higher concentration).

The new paradigm of multi-component materials, HEAs, offers a huge, almost infinite, number of possibilities for the developments of new materials with exciting properties.